Photonic micromachined devices : design, fabrication and experiment

Weiming Zhu

UNIVERSITÉ PARIS-EST

Ecole Doctorale

Mathématiques, Sciences de l'Information et de la Communication (MSTIC)

THÈSE

pour obtenir le grade de

Docteur de l'Université Paris-Est

Spécialité : Electronique, Optronique et Systèmes

présentée et soutenue publiquement par

Weiming ZHU

le 13 octobre 2010

Composants Photoniques Micro-usinés – Conception, fabrication et expérimentation

Photonic Micromachined Devices – Design, fabrication and experiment

Directeur de thèse
Tarik BOUROUINA
Ai-Qun LIU

Jury

Yong CHEN, Directeur de Recherches, ENS Paris	Rapporteur
Christophe GORECKI , Directeur de Recherches, FEMTO-ST Besançon	Rapporteur
Yamin LEPRINCE, Professeur, UPEMLV, Marne-la-Vallée	Examinateur
Bassam SAADANY, Chef du département MEMS, Si-Ware-Systems	Examinateur
Tarik BOUROUINA, Professeur, ESIEE Paris	Examinateur
Ai-Qun LIU, Professeur, Nanyang Technological University, Singapour	Examinateur

ACKNOWLEDGMENTS

I gratefully appreciate the help of my supervisors, Professor Tarik Bourouina and Professor Liu Ai Qun, who have not only offered me valuable guidance and advices in the academic studies but also encouraged me for excellent development.

I would like to express my thanks to Dr. Zhang Xuming who was the senior fellow in our team. He is the elder brother to all the group members and always set good examples to us.

Thanks to Dr. Cai Hong for giving me a good training on MEMS design, layout and fabrication processes. Thanks to Dr. Fu Yuan-Hsing for the helpful discussions. Thanks to Dr. Tang Min, Dr. Yu Aibin, Dr. Selin Teo, Dr. Wu Jiuhui, Dr. Muhammad Faeyz Karim and Dr. Khoo Eng Huat for their help and guidance. Thanks to Mr. Zhang Wu, Mr. Dong Bin, Mr. Ren Ming, Mr. Tao Jifang, Mr. Li Zhenguo, Mr. Chin Lip Ket, Ms. Xiong Sha and Ms. Yu Jiaqing for their helpful discussions and collaborations. I would like to express my thanks to Mr. Yu Yefeng who has been my roommate for almost five years. Thanks to all the group members for their help and accompany in those days.

I would like to express my thanks to ESIEE-Paris, Université Paris-Est and Nanyang Technological University for the supporting of this PhD project.

Finally, I would like to give my thanks to my family for their support and understanding.

SUMMARY

In this PhD project, three different approaches have been studied for tunable photonic devices based on MEMS technology. First, the optical double barrier structure has been numerically studied and experimentally demonstrated as the thermo-optical switch, switchable polarizer and optical tunneling junctions integrated as reconfigurable WDM system. Second, the slow light structure using metamaterial with coupled split ring unit cells is numerically analyzed. Finally, a tunable magnetic metamaterial is demonstrated using MEMS technology.

The first major work is to use the optical tunneling effects to design MEMS based photonic devices. Three different tunable photonic devices has been demonstrated using thermo-optical tuning. A thermo-optic switch is realized using MEMS technology. The device is fabricated on silicon-on-isolator wafer using deep etching process. The transmission of the optical switch is controlled by the optical length of the central rib which is thermally controlled by the external pumping current. In experiment, it measures a switching speed of 1 μs and an extinction ratio of 30 dB. *A* switchable polarizer is demonstrated using the double optical barrier structure which transmit the light with one polarization state and filter out the others. In experiment it measures a PER of lager than 23 dB when the pumping current is above 60 mA. The switching time is shorter than 125 μs which is limited by the polarization analyzer used in the experiment. A MEMS reconfigurable add-drop multiplexer is realized by applied the optical tunneling structure to the ribbed waveguide. The tunable add-drop multiplexer is based on Y-shape optical double barriers tunneling junction which are realized by MEMS technology. In the

experiment, a five-channel prototype of the tunable add-drop multiplexer is demonstrated. The measured output is ranged from 1549.24 nm to 1559.21 nm.

A tunable slow light metamaterial via tuning the substrate refractive index is numerically studied. The couple SRR unit cell is proposed for enhanced tunability and slow light function. The simulation results show that the coupled SRR design improves the tunability of the effective permittivity and the effective permeability by 70 and 200 times, respectively. The required permittivity change is only 0.025, which can be achieved by either thermal-optic effect or photon induced free carrier effect of the semiconductor materials. It may find potential applications in data storage, photonic circuits, optical communications and bio-sensors.

To show the real time modulation of the magnetic metamaterials, a THz tunable metamaterial using the MEMS technology is numerically analyzed and experimentally demonstrated. The tunable magnetic metamaterials is constructed by split ring unit cells the geometry of which can be changed by MEMS actuators. The size of the unit cells is around 40 μm × 40 μm corresponding to the resonance frequency in THz region. The effective permeability of the tunable magnetic metamaterial can be tuned from negative (-0.1) to positive (0.5) at the resonant frequency. It demonstrates a unique approach to control the optical properties of metamaterials via changing the geometric dimensions and shapes of the unit cells.

CONTENTS

LIST OF FIGURES

CHAPTER 1

INTRODUCTION

1.1 Motivation

More than 3000 years ago, ancient Chinese built beacon tower to deliver messages using the signal flame. Today, a single mode fiber with the core size around 9 micrometers can carry more than one trillion bits per second. To date, light is not only used as the medium of signals for telecommunications [1-10], but also used for laser manufacturing, biological and chemical sensing, medical diagnostics and therapy, display technology, and optical computing etc. Therefore, controlling light with a faster, stable and low power consuming way becomes the goal pursued by researchers studying photonic devices. Many switchable (or tunable) photonic devices such as tunable lasers [11-14], optical switches [15-20] and variable optical attenuators [21, 22] have been developed to meet the needs of vast applications. The bottleneck of further increasing the performance of photonic devices always lies in the following two questions: How to reduce the device scale so that it can be integrated in to a photonic circuit? How to control the micro-scaled or even nano-scaled photonic devices?

Microelectromechanical Systems (MEMS) offers a technical platform to solve the above two problems [23-25]. MEMS is the technology using very small (micro-scaled)

devices. It is also called Nanoelectromechanical Systems (NEMS) when the devices become nano size. Different from the hypothetical vision of molecular nanotechnology or molecular electronics, MEMS are made up of components between 1 to 100 micrometers in size (i.e. 0.001 to 0.1 mm) and MEMS devices generally range in size from 20 micrometers to a millimeter. Borrowing the ideas from large scaled devices, traditional MEMS technology succeed in building micro-scaled devices based on micromachining processes. MEMS technology offers the integration of mechanical elements, sensors, actuators, and electronics on a common silicon substrate through microfabrication on silicon wafer or adds new structural layers to form the mechanical and electromechanical devices. In this way, large size optical devices can be scaled down to micro-scale using the MEMS technology.

Generally speaking, there are two methods to control the propagation of the light within the tunable photonic devices. One method is to change the geometry of the photonic devices to control the path way of the signal light. For example, a movable mirror is often used to change the direction of the reflected light in MEMS optical switches. The other method is to change the optical properties of the device compositing materials such as the photonic switches. The first method is used in many MEMS optical devices. However, the switching time of the MEMS mechanical structures is typical at milliseconds. The second method attracts more and more research interests because of its faster switching time.

The optical properties of the compositing materials of the photonic devices are often realized by stimulating the material using thermo, electrical or optical method.

However the changes of the optical properties are quite limited. Take silicon for example, the refractive index change of the silicon is typically less than 0.5%. Therefore, the micro-optical resonators are often applied to enhance the effect of the compositing material change. In most cases, it is not feasible to simply scale down the optical cavities used in large scaled optical devices to build MEMS devices, because the size effects might cause some problems in the performance of the micro-scaled devices. Therefore, the optical resonators have to be carefully designed to meet the needs of the micro-scaled photonic devices.

Metamaterials refers to the artificial materials the optical properties of which relay on both the geometry of the unit cells and their compositing materials. The unit cells of metamaterials are sub-wavelength resonators of the incident light whose wavelength is typically ten times of the size of the unit cells. The size of the unit cells for THz metamaterials is around tens of micros which are the typical size for MEMS devices. Therefore, the geometry of the THz metamaterial unit cells can be tuned by MEMS technology. It offers another method to make micro-scaled tunable photonic devices.

1.2 Objective

The ultimate objective of this PhD project is to design micro-scaled tunable photonic devices which have merits of low power consumption, fast tuning speed, large tuning range and small device scales etc. To achieve this objective, two different approaches have been studied in this thesis: The first one is to apply MEMS technology

to double optical barrier structure the signal light of which is transmitted via resonance tunneling effect. The other approach is to use MEMS structure to tune the geometry of the THz metamaterial unit cells. In this way the material properties of the THz metamaterial can be changed for potential applications on tunable photonic devices.

The double optical barriers structures are often used to study the super luminance effects. In this PhD project, the frustrated total internal reflection (FTIR) structures are realized using MEMS technology to control the propagation of the signal light. A numerical analysis method is developed to study and optimize the parameters of the FTIR structure and five different tunable photonic devices are demonstrated.

In order to demonstrate the possibility of combine the MEMS technology with metamaterial structures, a numerical study on a tunable slow light waveguide is first given and then followed by the demonstration of a tunable magnetic metamaterial.

1.3 Major contributions

The major contributions of this thesis are summarized as the following:

A thermo-optic switch is realized based on optical double optical barrier structure, which has a high-low-high-low-high refractive index construct formed by micromachined silicon prisms and air gaps. Analysis shows such structure features full transmission (i.e., ON state) and requires low refractive index change for switching function. The device is fabricated on silicon-on-isolator wafer using deep etching process. In experiment, it measures a switching speed of 1 μs and an extinction ratio of 30 dB.

A switchable polarizer is demonstrated using the double optical barrier structure. In experiment it measures a PER of lager than 23 dB when the pumping current is above 60 mA. The switching time is shorter than 125 μs which is limited by the polarization analyzer used in the experiment.

A MEMS tunable add-drop multiplexer is realized by applied the optical tunneling structure to the ribbed waveguide. The tunable add-drop multiplexer is based on Y-shape optical double barriers tunneling junction which are realized by MEMS technology. In the experiment, a five-channel prototype of the tunable add-drop multiplexer is demonstrated. The measured output is ranged from 1549.24 nm to 1559.21 nm.

A tunable slow light metamaterial via tuning the substrate refractive index is numerically studied. The couple SRR unit cell is finally proposed and numerically characterized. The simulation results show that the coupled SRR design improves the tunability of the effective permittivity and the effective permeability by 70 and 200 times, respectively The required permittivity change is only 0.025, which can be achieved by either thermal-optic effect or photon induced free carrier effect of the semiconductor materials. It may find potential applications in data storage, photonic circuits, optical communications and bio-sensors.

A tunable metamaterial using the MEMS technology is numerically analyzed and experimentally demonstrated. The effective permeability of the tunable magnetic metamaterial can be tuned from negative (-0.1) to positive (0.5) at the resonant

frequency. It demonstrates a unique approach to control the optical properties of metamaterials via changing the geometric dimensions and shapes of the unit cells.

1.4 Organization of the thesis

This thesis is focused on the design and experiment of the tunable photonic devices based on MEMS technology which is divided into six chapters:

Chapter one gives a brief introduction of the motivation, objective, major contribution and organization of the thesis.

Chapter two gives the literature survey on optical resonators, tunable photonic devices and tunable metamaterials.

Chapter three demonstrate MEMS devices based on optical tunneling effects. Firstly, the frustrated total internal reflection (FTIR) optical barrier structure is presented and its transmission states are numerically studied via transfer matrix method (§3.1). The design of MEMS optical double barriers switch will be first elaborated, followed by the theoretical and experimental analyses is shown in §3.2. Then, the application of the MEMS optical double barrier structure as the switchable polarization beam splitter is shown in §3.3. The optical tunneling effect is combined with the rib waveguide and form a reconfigurable optical tunneling junction is shown in §3.4 and followed by its applications on the wavelength de-multiplex system. Finally the conclusion is shown in §3.5.

Chapter four is focused on the tuning of the slow light metamaterials via the refractive index change of the substrate. The tunablility of the tunable metamaterial is

limited by the material properties of the substrate, the tuning range of which is normally not very large. The objective of this chapter is to find a new metamaterial structure which can enhance tunability of the tunable metamaterials. Furthermore, the tuning of the group velocity index of such tunable metamaterials is also numerically studied. This chapter is organized as follow: The design of the slow light waveguide constructed by metamaterials is shown in §4.1. The fishnet unit cell is analyzed in §4.2 as a possible candidate for the building blocks of slow light waveguide. A coupled SRR unit cell is given in §4.3 for better tunability. The tuning of the material properties and slow light group index on a fishnet metamaterial is shown in §4.4. The discussion on absorption is given in §4.5.

Chapter five shows a new way to tune the optical properties of the metamaterials. This tuning method combines micromachined technology with the design of the metamaterial unit cells. It can make the metamaterials tunable without exciting their compositing materials. Therefore, the tunablility of the metamaterial is no longer limited by the refractive index change of the nature materials. In this chapter, a split ring structure is selected to demonstrate the tuning method. The electrical and magnetic response of the tunable metamaterial is demonstrated both numerically and experimentally. This chapter is organized as follows: The design of the tunable metamaterial is given in §5.1. The numerical analysis of the tunable metamaterial is shown in §5.2 and followed by the fabrication (§5.3) and experimental demonstration in §5.4. Finally the summary is given in §5.5.

CHAPTER 2

LITERATURE SURVEY

In this chapter, the literature survey of optical tunneling, micro-cavities, optical switches, slow light waveguide and metamaterials are presented. The optical micro-cavities are the key components for the micro-scaled photonic devices tuned by changing the material properties of the compositing materials which is faster and more stable than those devices tuned by the mechanical method. Here the optical micro-cavities are categorized by their geometry and summarized by their quality factors. The micro-scaled optical switches are presented to be compared with our approaches in Chapter 3. Finally, the survey of metamaterials is presented.

2.1 Survey of optical tunneling

2.1.1 Definition of the optical tunneling effect

Optical tunneling effect refers to the phenomenon of photons penetrating through the classically impenetrable barriers (e.g., the interface where the total internal reflection occurs, photonic bandgap, metal layer, etc.), similar to the electron tunneling through the quantum barriers. Such effect has attracted broad interest of physical studies for both fundamental and technological reasons and has actually become the cornerstone between

the classical theory of electromagnetic waves and quantum physics. In particular, the optical tunneling effect is indispensable to the experimental study of tunneling process. Since the wavelength of light is around 1 μm, optical tunneling structures are on order of micrometers compared to the nanometer-scale electron tunneling structures. Additionally, the optical tunneling is not complicated by other side effects such as electron-electron couplings.

According to the quantum physics, all particles, including photons, can tunnel trough barriers which classically impossible for them to go through. Photons can tunnel through the optical barriers such as the photonic band gap, mental, above-critical-angle air gap (FTIR effect) and show great similarity to the electron tunneling effect. For decades, the analogy between the photon tunneling and electron tunneling has been widely studied because the longer wavelengths of the photons bear great advantage in experiments [26, 27].

According to resent research on the analogue of optical and electron tunneling effects, identical transmission probabilities can be obtained from the two dimensional Maxwell equations for photons and the one dimensional Schrödinger equations for electrons by making the equivalence as below [28],

$$\frac{2mE}{\hbar^2} \Leftrightarrow \frac{\omega^2}{c^2} cos^2\theta$$
$$\frac{2m(V_0 - E)}{\hbar^2} \Leftrightarrow \frac{\omega^2}{c^2}(n^2 sin^2\theta - 1) \tag{2.1}$$

where m, V_0 and E are the mass, barrier potential, and energy of the electron, respectively; while ω, n and θ, n denote the frequency, medium refractive index and the incidence angle of the photon, respectively.

Consider the photon tunneling process within non-absorption single and double optical barriers structures. When an optical wave incident on a single barrier structure, some of the photons tunnel through the barrier and others are reflected back. The amplitudes of the electric field reflected backward by different interfaces are geometric proportional such that the elimination of the reflection will be impossible. However, the situation is a bit more complex when two optical barriers are taken into consideration. Similar to the electron tunneling cases which have been theoretically studied [29] and experimentally observed [30] quite a long time ago, the tunneling probability can be greatly enhanced by the resonance of the photons between the two barriers. Furthermore, the total transmission condition can be achieved by adjusting the potential of the optical barriers and the distance between them. In another word, the optical barrier can be bridged by placing another barrier beside it with proper distance and potential which is named as the resonance tunneling effect in both electron and photon multi-barriers.

2.1.2 Applications of the optical tunneling effect

In quantum physics, optical tunneling effects are often used for experimental demonstration of the superluminal effect. The superluminal effect, also named as the faster than light (FTL) effect, refers the propagation of information or matter with the speed faster than the light. The superluminal effect has been proposed and studied for years shortly after the discovery of quantum mechanical tunneling. In 1930, the

discussion on the speed of the tunneling process is brought up. A approximate analysis on time dependent Schrodinger equations and the conclusion that the tunneling takes no appreciable time was made. This conclusion had been discussed for 30 years until the quantum tunneling devices has been made based on thin film technology. Then the question is revised in an effort to understand the frequency limitations for tunneling structures consisted of metal-insulator-metal thin film sandwiches and an analytical expression for the time delay in barrier tunneling which suggests a finite and short traversal tunneling time that saturates with distance was given. To date, although no direct experiment shows the tunneling speed of matter can be faster than the speed of light, the experimental study on superluminal effect using optical tunneling structures remains an interesting research which has potential applications on communication and space travelling.

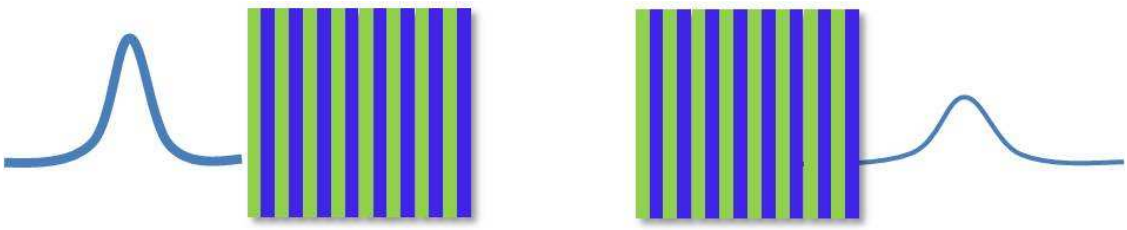

Fig. 2.1: Schematic of optical tunneling on 1D photonic structure

The experimental measurement of superluminal optical tunneling times in double barrier photonic band gaps was demonstrated by [30]. The tunneling pulses is chosen to be 1500 nm in wavelength and the experiment is carried out on double barrier fiber Bragg gratings. The transit time is measured to be paradoxically short which implying the

superluminal propagation and the saturation effect on the barrier distance are also observed.

The other and maybe the most widely used application for optical tunneling effect is the coupling of the photonic devices between sub-wavelength gaps. For example, optical tunneling effects has been used as the coupling between the waveguide and photonic micro-cavities, the coupling between the prism and metal surface for the generation of the surface plasmon waves and the coupling between the laser head and cavities. In Chapter 3, the optical tunneling effect using frustrated total internal reflection will be used to design the thermo-optical switches.

2.2 Survey of optical micro-cavities

Dielectric optical micro-cavities are the key components for densely-integrated optical circuits. Most of the micro-cavities now used are large compared with the resonance wavelengths which are the limits of the size of the micro-cavities. However, the structure size of the micro-cavities can be reduced to the order of the wavelength by using the compositing materials with large refractive index contrast. The optical micro-cavities can be categorized into three different types by their geometry, such as the Fabry-Pérot (FP) cavity, photonic crystal micro-cavities and the whispering gallery micro-cavities etc.

2.2.1 Fabry-Pérot micro-cavities

The Fabry-Pérot (FP) micro-cavity is named after Charles Fabry and Alfred Perot who construct this optical micro-cavity as interferometer [26, 27]. The typical FP cavity is constructed with a transparent plate with two reflecting surfaces, or two parallel highly reflecting mirrors (Fig. 2.1). Divided by their mirrors, the FP micro-cavities can be categorized by three different types: the plane mirror FP micro-cavities (Fig. 2.1(a)), the curved mirror FP micro-cavities (Fig. 2.1(b)) and the Bragg mirror FP micro-cavities (Fig. 2.1(c)). The plane mirror FP micro-cavities are the most basic type of the FP cavity and have been widely used in the applications such as laser cavities, etalon and filters [28, 29]. The curved mirror FP cavities can further focus the light due to the shape of its mirror which reduces the scattering loss due to the mirrors. The Bragg mirror FP micro-cavities has larger Q factors than the cured mirror and plane mirror FP cavities because the Bragg mirror usually has a larger reflection coefficient.

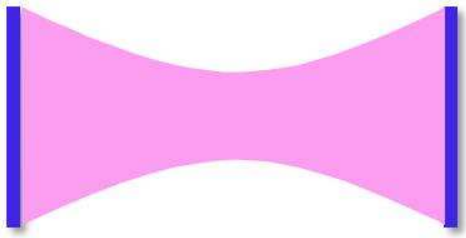

(a)

(b)

(c)

Fig. 2.2: Different types of Fabry-Pérot micro-cavities. (a) the plane mirror FP cavity, (b) the curved mirror FP cavity and (c) the Bragg mirror FP cavity.

The transmission spectrum of FP micro-cavities as a function of wavelength exhibits peaks of large transmission corresponding to resonances of the micro-cavity. The transmission coefficient can be written as [30]

$$T = \frac{(1-R)^2}{(1-R)^2 + 4 \cdot R \cdot sin^2(\frac{2\pi d}{\lambda})} \tag{2.2}$$

where T is the transmission coefficient, R is the reflection coefficient of the mirrors, d is the optical length between the two mirrors and λ is the wavelength.

The FP cavity is widely used in telecommunications and laser optics. The most important common applications are as filters, in which a series of thin film layers are deposited on an optical surface by vapor deposition. Those multi thin film layers structures have similar geometries with 1D photonic crystal [30]. The FP cavity can also be used as the optical wavemeter, laser cavities and etalons etc. The FP optical cavities

can be scaled down to micro size for densely-integrated photonic circuit. However the edge effects caused by the scattering of the light become obvious when the cavity size become small enough to be compared with the wavelength.

2.2.2 Photonic crystal micro-cavities

Periodical structures with high refractive index contrast have recently become very interesting structures for light localization. The periodical structures, also called photonic crystals, can be designed to have the photonic bandgap which stop the light from propagating at all directions. Theoretically speaking, light can be trapped within a very small region by constructing the confinement periodical structures at three dimensions (3D). However, 3D photonic crystals are not easy to be fabricated with the existing fabrication techniques [31, 32]. 1D photonic crystals derived directly from Bragg reflectors has already been widely used in commercial applications such as data communications, laser cavities and sensors etc. 2D photonic crystals are fabricated using dielectric membrane with periodically patterned holes or arrays of small pillars which have been demonstrated in many works [33-37].

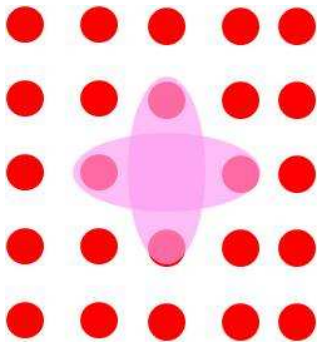

Fig. 2.3: Schematic of 2D photonic crystal micro-cavity.

The photonic crystal micro-cavities can be designed to have not only very high quality factors (Q factor) but also very small mode volumes. The light can be localized within a very small region according to the design. The typical lattices of the photonic crystals are one quarter of the resonance wavelength and the photonic crystal micro-cavities can be realized by simply remove or change the positions of the building blocks (holes or pillars). Therefore, the size of the photonic micro-cavities can be scaled down the order of the wavelength. Furthermore, the lattice structures are very easy to be integrated with each other. However, the coupling of the light from outside to the photonic micro-cavities remains a problem. The large Q factor increased the light-matter interactions which ensure the nonlinear tuning of the photonic crystal micro-cavities. However, the large Q factors also lower the threshold of the signal light induced nonlinear effect which limits the power of the signal thus decrease the signal noise ratio (SNR).

2.2.3 Micro-cavities with whispering gallery mode

The whispering gallery modes are confined by continuous total internal reflection of the cavity interface. One of the largest whispering gallery mode cavities is the temple of the heaven the size of which is around 5000 square meters. The resonant waves are the sound waves other than the optical waves. However, the whispering gallery mode cavities can be scaled down to small enough to compare the resonant wavelength. In recent years, many different micro-cavities with whispering gallery mode have been studied, such as the micro-sphere cavities, the toroid micro-cavities and the micro-ring cavities [38-40].

The whispering gallery mode micro-cavities have many applications such as micro-lasers, narrow filters, optical switching, ultrafine sensing, displacement measurements, high resolution spectroscopy, Raman sources and studies of nonlinear optical effects.

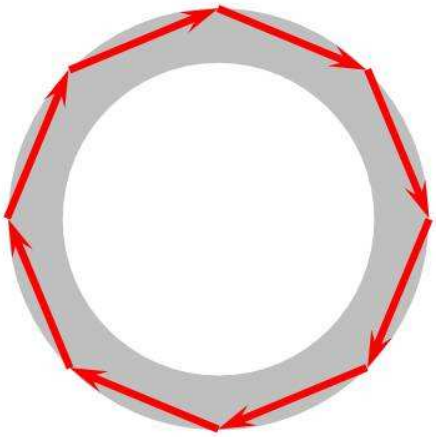

Fig. 2.4: Schematic of whispering gallery mode (WGM) micro-cavity.

Similar to the photonic crystal micro-cavities, the whispering gallery mode micro-cavities has merits such as, high Q factor, small mode volume and small size etc. The fabrication techniques remain challenging regarding the commercial applications. As the scattering loss dominate the total loss of most whispering gallery modes, the cavity surfaces have to the carefully polished.

Micro-cavities fabricated using dielectric materials, such as semiconductors, glass and polymers etc., are the key components for most of the tunable photonic devices which is modulated using the nonlinear effects. Dielectric micro-cavities can localize the light field within a very small volume thus have a high Q factor and enhanced light-matter interaction. In this way, the nonlinear effects of the nature material can be

amplified and the resonant frequency of the micro-cavities can be shifted. This is the basic concept used in most micro-scaled tunable photonic devices which has been intensively studied recently. However, the dielectric micro-cavities have the limitations as follows: Firstly, the power of the signal light is limited by the Q factor and compositing material of the micro-cavities. Signal light of large power may introduce the nonlinear effect of the micro-cavities and cause the self-modulation. This problem can be solved by choosing the signal light wavelength at non-sensitive regions of the compositing materials. Another limitation of the micro-cavities is the narrow band width of the resonant spectrum. The working frequencies are typically chosen to be the resonance frequency of the micro-cavities thus the spectrum can be very narrow band due to high Q of the micro-cavities. Finally, the dielectric micro-cavities control the light by modulate the electric field of the incident light waves. Dielectric micro-cavities cannot directly affect the magnetic field without ferromagnetic components which limits their applications on magnetic resonance based devices such as superlens. In chapter three, a new approach is developed to design the tunable photonic devices based on MEMS technology.

2.3 Survey of optical switches

Optical switches often refers to the device that enables signals in optical fibers or integrated optical circuits (IOCs) to be selectively switched from one circuit to another. In commercial term, optical switch often refers to the equipment that switches the signal light from one photonic circuit to another by electronically switching between fiber

transponders. Traditional MEMS borrow the ideal form the commercial optical switches and using movable mirrors or shutters to switch the light in micro-scaled photonic circuits using electronically controlled actuators. In recent years, photonic switches which switch the pathway of the light using nonlinear effects attract more and more research interest due to their fast switching speed and low power consumption. In this section, the optical switches are categorized by their switching mechanism.

2.3.1 Mechanical optical switch

The mechanical optical switches refer to those devices which change the path way of the light using the mechanically actuated moveable paths such as the movable optical fibers or mirrors [41-43]. Fig. 2.4 shows the schematic of a mechanical optical switch based on MEMS movable mirrors. The optical switch consists of four components: one input fiber, two output fibers and a movable mirrors. The input and output fiber 1 is directly coupled to each other and the output fiber 2 is placed perpendicularly to the other two fibers. The signal light from the input fiber is reflected 90° to the output fiber 2 when a 45° tilted movable mirror is placed between the input fiber and output fiber one (Fig. 2.4 (a)). The signal light can be switched to output fiber 1 when the moveable mirror on longer block the signal light between the input fiber and output fiber 1. In this way, the signal light from the input fiber can be switched between the output fiber 1 and 2 by mechanically change the position of the moveable mirrors [44, 45].

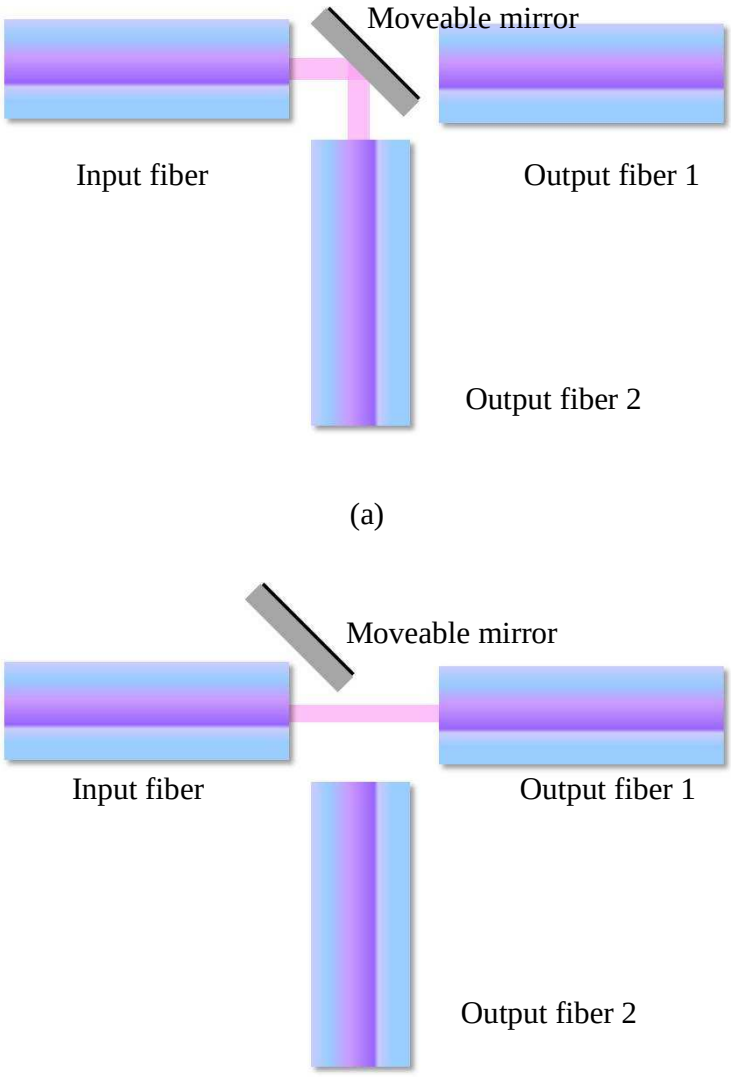

Fig. 2.5: The schematic of a mechanical optical switch. (a) signal light is switched to output fiber 2 (b) signal light is switched to output fiber 1.

This kind of the optical switches advanced in broadband switching and simple geometry. However, the switching speed is limited by the mass of the movable parts. That is because the acceleration of the movable parts (fibers, mirrors) obeys the Newton's

law while the force given by the actuator cannot be increased infinitely. The typical switching time of the mechanical optical switch in micro-scaled size is around several milliseconds. Furthermore, the typical sized of the actuator is around several square millimeters which prevent the mechanical optical switches from being densely integrated.

2.3.2 Thermo-optical switch

The thermo-optical switch refers to those devices which switch the pathway of the signal light by the thermo-optical effect [46-47]. The thermo-optical switch can be divided into two groups. One is switching the light using thermo-expansion effect. For example, the transmission the Bragg mirrors is highly depended on the lattice constant of each mirrors. When the lattice constant is change by the thermo effect, the transmission of the Bragg mirror of certain wavelength can be switched from 100% to 0%. In this way the Bragg mirror can be functioned as an optical switch. The switching speed of the thermo-expansion is similar to that of the mechanical optical switch. As this kind of switching requires heating the whole mirror, the switching speed of the thermo-expansion optical switch might be even delayed by the heat diffusion process without cooling system.

The other kind of thermo-optical switch is changing the refractive index of the optical micro-cavities via thermo-effect. For example, the thermo-induced refractive index of the silicon material can be expressed as follow [48]

$$\frac{dn}{dT} = 1.86 \times 10^{-4}/K \tag{2.3}$$

The switching time of the thermo-optical switch is around microseconds since the localized heating is required only on the micro-scaled optical cavities. The expansion of the crystal lattice for nature crystals is typically around microseconds. However, most thermo-optical switches have much longer switching time due to the lack of fast heating system and cooling systems which is not easy to be integrated to the micro-scaled devices.

2.3.3 All optical switch

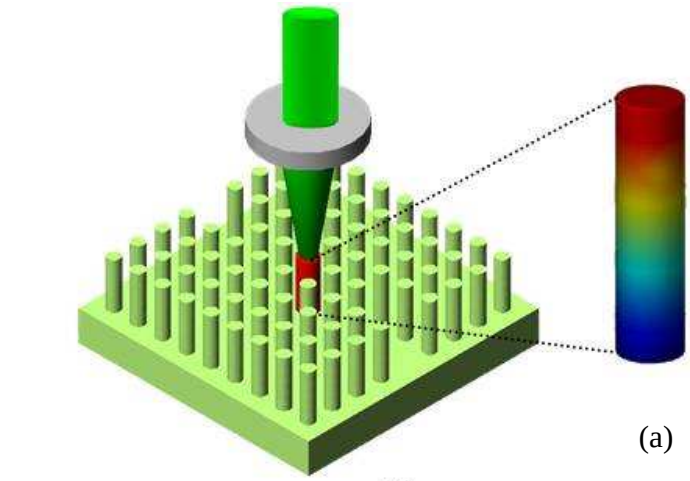

(a)

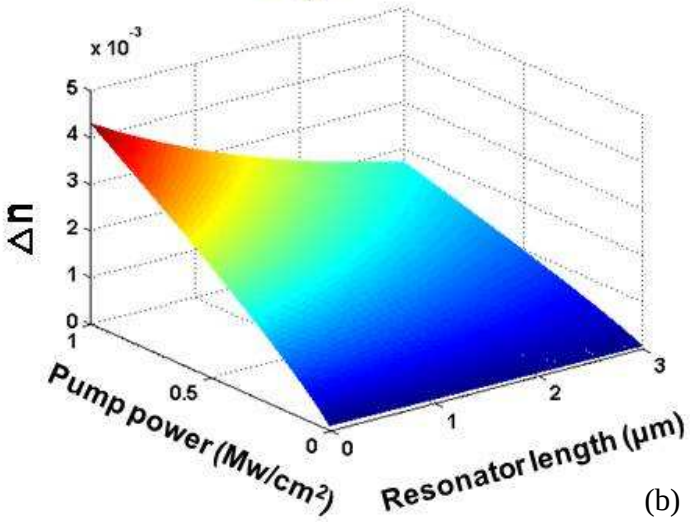

(b)

Fig. 2.6: (a) The schematic of all optical switch based on 2D photonic crystal cavities. (b) The change of the refractive index as the function of pumping light power and the length of the central resonator.

The concept of all optical switches derives directly from the ideal of all optical networks (AON) or all photonic circuit which, analogy to the electronic circuit, uses light wave communication exclusively within the network. In this way the limitation of the optical-electrical-optical (OEO) conversion can be circumvented. All optical switches are the building blocks for the optical transistors and optical logic gate. Practically speaking, the power of the signal light within the optical switch has to be comparable to the triggering light so that it can be used in AON. Most of the reported all optical switches are, more precisely speaking, optical switches triggered by photon induced free carrier effect. For example, the all optical switch based on 2D photonic crystal cavities is shown in Fig. 2.5 (a) [49]. The refractive index of the central resonator is changed by the vertically incident pumping light while the pathway of the signal light within the photonic crystal waveguide can be modulated. The free carrier effect on refractive index change Δn is plotted in Fig. 2.5 (b) using the following equations [48]

$$\Delta n = -[8.8 \times 10^{-22} \Delta N_e + 8.5 \times 10^{-18} (\Delta N_h)^{0.8} \tag{2.2}$$

where ΔN_e and ΔN_h is the free carrier density induced by free electrons and holes respectively.

The triggered light changes the refractive index of the optical switch compositing material thus changes the pathway of the signal light. Therefore, the power of the triggered light are much stronger than that of the signal light which creates a bottleneck for the all optical switch applications. The typical switching time of the all optical switch is in the order of picoseconds which are limited by the carrier relaxation time. Researchers in quantum optics are building all optical switches using photon-photon interactions which use one photon to control the transmission of the other. It might be a solution to the above mentioned problem. However, there are still many basic works unfinished.

Optical switches have been widely used in telecommunications, optical computations and biomedical chips. Of all the applications, the switching speed is always the most frequently concerned parameter of the optical switches which are limited by the following conditions: Firstly, the ultimate bottleneck of the switching time is the response time of the compositing materials to each switching mechanisms. For example, the switching speed of the mechanical optical switches is limited by the moving speed and displacement required by the moving components such as the movable mirrors and shutters. However the thermo-optical switch is limited by the material response of the thermo expansion and relaxation time of the crystal lattice. Therefore, changing the compositing material may be one solution to further increase the switching time. For example, the optical properties of many nonlinear crystals, such as the liquid crystal, can be dramatically changed by the thermo or electrical excitations. Such nonlinear crystals can be used as the compositing material for the optical switches. For example, liquid

crystals are used in optical micro-cavities or Mach–Zehnder interferometer [50] for optical switching. However, the nonlinear crystals increase the fabrication difficulties and are not suitable for densely-integrations.

2.4 Survey of slow light waveguides

Generally speaking, there are two procedures that can be used to control the group velocity of light. One of these is to exploit material resonances, such as the sharp absorption resonances of an atomic vapor. Control can be achieved, for example, by applying a strong optical field and using nonlinear effects to modify the optical response experienced in a signal pulse, as in the work of Hau et al. Examples of this approach are electromagnetically induced transparency (EIT). In addition to EIT, there are several other sorts of material resonances that can be used to produce slow-light effects. There has been particular success with the use of stimulated Brillouin scattering and the use of stimulated Raman scattering. In each of these processes, the strong gain feature induced by the presence of a strong pump field will also produce, as a consequence of the Kramers–Kronig relations, a rapid spectral variation in the refractive index, which in turn leads to strong slow-light effects. The other procedure is to use material engineering to fabricate microstructured materials, such as arrays of microrings and photonic crystals that have artificially created resonances and optical responses. For instance, the group velocity of light in a photonic crystal can be slowed down dramatically near the band edge of the photonic Brillouin zone. One particular example of this approach is the work

of Vlasov et al. at IBM, in which by appropriate patterning of a silicon waveguide a group index of 300 was produced, corresponding to a 300-fold reduction in the group velocity.

In recent years, slow light has been intensively studied by two different groups of researchers divided by the frequency region they are interested in. One group of people works on the optical region. They use dialectic only waveguide with large dispersion to slow the light down by resonance. For example, the coupled resonance optical waveguide (CROW) is used for slow light purposed since the photon life time in the high Q optical cavities are very long. Generally speaking the electric response of the wave-guiding structure is tailored by introducing the artificial structures. The other groups of researchers work on slow backward waves established in engineering practice giving rise to both microwave tubes [51] and to antennas [52]. Waves propagating on coupled LC circuits were investigated by Atabekov [53] and Silin and Sazonov [54] as simple examples of periodic filters and slow wave structures which is similar as the CROW in the optical frequency region. An antenna array shown in [55] excited by a single element was shown to be able to support a leaky wave which is partially guided and partially radiating. Slow waves can also be achieved by propagating the light along a set of spherical nano-particles [56-58], electrically coupled metallic rods [59], or a set of magnetically coupled loops as shown in [60, 61]. Those slow light waves generated by tailoring the magnetic response of the wave-guiding structures are called magneto-inductive (or MI) waves. Metamaterials offers a platform to tailor both the electric and the magnetic response of the artificially engineered wave-guiding structures. Therefore,

both the electro-inductive and magneto-inductive slow light waves can be found in metamaterials.

2.5 Survey of metamaterials

This Metamaterials are artificially engineered materials, formed by integrating various sub-wavelength unit cells, which can exhibit unconventional optical responses not observed in their individual compositing materials or in natural media. For example, negative, low, or near-zero permittivity or permeability can be observed in metamaterials with carefully designed unit cells. The negative refractive index can be observed in certain frequencies when both the permittivity and the permeability are negative. Metamaterials, especially the negative refractive index metamaterials, have attracted a great deal of research interest in recent years [62-77]. The first experimental verification of a metamaterial with negative refraction is demonstrated at microwave frequencies [78] using split-ring resonators predicted by Sir Pendry [79]. Experimental and theoretical studies of metamaterials which started in the microwave frequency region are steadily moving into the higher frequency region. Recent experimental breakthroughs show the optical response of metamaterials in the THz, infrared, and visible frequencies [80-83] with the aid of the nano-fabrication techniques.

It is important to point out that the concept of metamaterials is not limited to the negative-index material. Other artificially engineered materials with unusual parameter values, such as epsilon-near-zero (ENZ) materials [84, 85], epsilon-very-large (EVL) materials [86, 87], highly dispersive materials, and single-negative (SNG) media, may

offer exciting potential applications as well. For instance, using ENZ materials, it has been shown theoretically that the possibility of squeezing light through very narrow channels and tight bends [88]. The ENZ materials which are used in transparency and cloaking are also shown in [89, 90]. Generally speaking, metamaterials provide a platform for dispersion engineering and management which means the dispersion of the materials can be designed by changing the geometry of their unit cells. It is a direct method to modulate and tailor electromagnetic waves. For example, it is well known that by stacking pairs of thin layers of plasmonic material (e.g., Ag) and conventional dielectric, one can form an anisotropic metamaterial whose permittivity tensor elements can achieve near zero or very high values [91] which cannot be achieved by bulk materials with single composition.

2.5.1 Magnetic metamaterials

Magnetic metamaterials consisting of artificially designed unit cells with a strong magnetic response have been developed into an important branch of the metamaterials research. For example, the split ring resonator unit cell is designed for strong magnetic response which was investigated in [92-99]. Many works have been down in different forms of split ring structures. One of the split ring structures with broadside coupling is proposed in [100], another structure, namely the twin split ring, was proposed in [101], and a three-dimensional set of rings, isotropic split ring, was introduced in [102]. The singly split ring was known before as a broken loop [103, 104]. The split pipe [105, 106] is a novel bulk variant of the single ring resonator without need of a substrate; it was also introduced under the name of the finger ring [107]. The loop with loaded capacity was

described by Schelkunoff and Friis [108] and later used by Wiltshire et al. and by Mossalaei et al. [109]. Other metamaterial unit cells with strong magnetic resonance are also proposed, such as double circular elements [110], chiral, double-helix particles, the Swiss Roll [111] and the Spiral Resonator [112] etc. Other metamaterials using particles are also demonstrated such as “castle” rings [113], “labyrinth” rings [114], or “metasolenoids” [115]. The development of the field of magnetic metamaterials has taken a new turn when miniaturization of split rings using microfabrication was employed to increase the magnetic resonance frequency of meta-materials to 1 THz (300 μm wavelength) [116]. Nanofabrication led to further increase of the magnetic resonance frequency first to 100 THz (3 μm wavelength) [117] and most recently to the visible range [118-120]. Novel nanoparticles such as a pair of closely spaced nanostripes or nanorods [121, 122], the nanostructured U-particle [123, 124] and the nanostructured “ crescent” [125] were introduced. The magnetic metamaterials open a gateway to tailor the magnetic response of the artificial structures without introducing the ferromagnetic materials.

2.5.2 Tunable metamaterials

Metamaterials are the artificial materials with many properties which may result in the applications which cannot be realized by nature materials, such as invisibility cloaks, negative refraction and perfect lenses [126-130]. However, metamaterials has drawback as follows: Firstly, the significant frequency dispersion caused by the resonance nature of the metamaterials leads to the narrow bandwidth and large metal absorption. Although narrow bandwidth is required for some applications, the

applications of the metamaterials are limited by its narrow bandwidth in many cases. Practically speaking, the working frequency range of any given design on metamaterials is about 5% to 10% compared to its central frequency. Like many nature materials, the limitation on the bandwidth and absorption severely restricts metamaterials from many potential applications. Therefore, a compositing of the nature materials with metamaterial structures, namely hybrid metamaterials, become the subject which is under more and more intensively researches [131, 132].

Hybrid metamaterials refer to those metamaterials the compositing materials of which are strongly involved in the resonant of their unit cells. In other words, the optical properties of the hybrid metamaterial, such as the effective permittivity and permeability, are strongly dependent on the material properties of their compositing materials. The hybrid metamaterials have passive properties (e.g. native electric response, negative magnetic response or slow light) which are prior designed by the geometry of the unit cell and compositing materials which is similar to all the artificial materials. In addition, the hybrid metamaterials have dynamic properties, such as photoconductivity, nonlinearity, gain etc., which result from the strong interaction between the compositing material and the unit cell resonance [133-140]. In another point of view, the hybrid metamaterial is designed to enhance or tailor the nonlinear properties, such as the photoconductivity, thermo-optical effect and free carrier injection via voltage, which belong to the compositing materials of the hybrid metamaterials.

The dielectric compositing materials of the metamaterials are often used as the substrate to provide the mechanical support for the metal parts [141, 142]. The effect of the metamaterial substrate has long been considered as the red shift in the working

frequency and the origin of the dielectric loss which need to be minimized by the design. However, the tunable electric response of the substrate offers a method to dynamic control the metamaterial unit cell resonance both on the resonant frequency and the resonant magnitude. The tunable hybrid metamaterials by optical and voltage switching method have been demonstrated by Willie J. Padilla and Richard D. Averitt from Boston university [143-147]. The metamaterial with gain medium to compensate the loss due to the metal structures have been intensively studied recently [148-150]. The absorbed light energy caused by the collision of the electrons in the metal parts of the unit cells can be compensated by the electrically pumped gain medium inside the unit cells. It offers a possible solution to the loss problem of the metamaterials.

2.6 Summary

The literature survey is conducted to fulfill the two major objectives of this PhD project. One is to design MEMS based photonic devices from the device level which is focused on how to build photonic devices by designing a structure which is much larger than the working wavelength. The other one is to design a MEMS based photonic devices by reshaping sub-wavelength unit cells which is regarded as the atom of the materials. Those kinds of devices has potential applications which mainly comes from the material properties of the massive unit cells and working at longer wavelength region such as THz. Therefore, the literature survey is focused on two different parts. One is the optical tunneling structures [156-165] which are used for building the MEMS photonic devices

at device level and their counterpart optical micro-cavities which has already been widely used in optical MEMS. The other is metamaterial and the slow light waveguide.

The optical cavities, such as the F-P cavities, photonic crystal cavities and WGM cavities etc., have already widely been used in optical MEMS for the design of micro-scaled photonic devices for years because of the merits such as small size, enhanced light matter interaction, high sensitivity of the environmental change etc. The resonance tunneling structures are similar with the optical cavities due to the resonance nature of the light which leads to properties such as wavelength selective, high Q factor, and tunable etc. However, in this PhD project, an optical double barrier structure is chosen to build MEMS based photonic devices due to the reasons listed as follows. Firstly, the coupling of the FTIR double barrier structure to the output can be controlled by the MEMS structure. The coupling efficiency of the tunneling structures determines the photon life time within the FTIR structure which is one of the key features dominating the Q factor of the whole device. Secondly, the tuning of the FTIR tunneling structure is more flexible using MEMS structure than that of the micro-cavities. As will be discussed in chapter 3, the FTIR structure can be tuned by changing the refractive index of the compositing material, the incident angle or the polarization states etc. which can be possible realized with the MEMS technology. Finally the FTIR tunneling structure can be tuning by the refractive index variation of the central rib which can be used as the waveguide of the pump light for all-optical modulation. It might be one solution to reduce the pump light power of the tunable devices realized by photon induced free carrier effect which requires very high power pump light in most devices based on optical micro-cavities.

Metamaterials are engineered materials the unit cells of which are designed to mimic the molecular or atoms of nature materials. Like other artificial materials, such as photonic crystals, metamaterials offers a platform to tailor the light by the design of the unit cell geometry. In this chapter, three interesting metamaterial properties related to the PhD project presented in Chapter 4 and Chapter 5 have been introduced. Firstly, the slow light properties of the metamaterial are surveyed. The slow light effect has been widely studied in the dielectric waveguides using high Q factor cavities. However, most of the dielectric high Q factor cavities confine the light by tailor its electric field. Metamaterial offers a new platform to directly response the incident magnetic field and slow light by the coupled magnetic resonators. The magnetic response of the metamaterial unit cells not only results in the magneto-introductive slow light waves but also results in many applications which cannot be realized in nature materials. However, those applications, such as the super lens, cloaking, and negative refractive index slow light effect, are quite limited by the narrow band and high absorption due to the resonance nature of the metamaterial unit cells. Tunable metamaterial offer a possible solution to such problem by changing the electric response of the substrate of the metamaterials. The narrow band width can be partially solved by the metamaterials with tunable working frequencies while the absorption problem can be compensated by adding gain medium to the metamaterial unit cells. In chapter 4, a slow light metamaterial with tunable slow light factor controlled by the substrate refractive index is proposed. A mechanical tunable metamaterial using MEMS structure is demonstrated in Chapter 5.

CHAPTER 3

OPTICAL TUNNELING AND DEVICES

Most of the previous studies focus on only the single optical barrier structure. The main purpose is to study the frustrated total internal reflection (FTIR) phenomenon and the associated superluminal tunneling process. Optical structures with more than one barrier are not well addressed. On the other hand, the electron tunneling through the double quantum barriers presents an interesting feature that the tunneling probability can be greatly enhanced by the resonance between the two barriers, which have been theoretically studied and experimentally observed quite a long time ago. Based on the analogy of optical tunneling and electron tunneling, the double or even multiple optical barriers should work for the optical transmission characteristics. Microelectromechanical systems (MEMS) is the technology of the very small (micro-scale) systems which are often used as platform of integrated mechanical elements, sensors, actuators. It is possible to realize the switchable optical tunneling devices via the micro-machined structure which are consist of the components ranging from several to hundreds of microns.

The objective of this chapter is to demonstrate MEMS devices based on optical tunneling effects. Firstly, the frustrated total internal reflection (FTIR) optical barrier structure is presented and its transmission states are numerically studied via transfer

matrix method (§3.1). The design of MEMS optical double barriers switch will be first elaborated, followed by the theoretical and experimental analyses is shown in §3.2. Then, the application of the MEMS optical double barrier structure as the switchable polarization beam splitter is shown in §3.3. The optical tunneling effect is combined with the rib waveguide and form a reconfigurable optical tunneling junction is shown in §3.4 and followed by its applications on the wavelength de-multiplex system. Finally the conclusion is given in §3.5.

3.1 Design and numerical analysis

In this section, the FTIR optical barrier structures are numerically analyzed. The schematics of the single and double FTIR optical barrier are firstly given. Then followed by the introduction of the transfer matrix method which is used as the mainly tool for the numerical simulation in this chapter. Finally, the transmission coefficient of both single and double optical barriers structures are analyzed under different parameters. To avoid ambiguity, the simulation of this section is using the transverse magnetic (TM).

3.1.1 Single and double FTIR optical barriers.

The single optical barrier and the double optical barriers are illustrated in Figs. 3.1(a) and 3.1(b), respectively. The single optical barrier structure consists of two identical hemi-spherical dielectric prisms separated by a thin air gap. The FTIR condition is achieved by adjusting the incidence angle beyond the critical angle. As the prisms have higher refractive index, the air gap functions as an optical barrier as illustrated in Fig. 3.1(c). When a EM wave is incident on the single barrier, some of the photons tunnel through the barrier while others are reflected back. As the reflection always exists (unless the air gap width $d = 0$, i.e., no air gap), the transmission cannot reach 100%. The double barrier structure in Fig. 3.1(b) has one more dielectric rib between the two prisms. In this way, it forms two air gaps and thus double optical barriers as illustrated in Fig. 1(d). Analogy to the electron tunneling cases, the resonance of photons between two barriers could conceptually enhance the transmission to 100%.

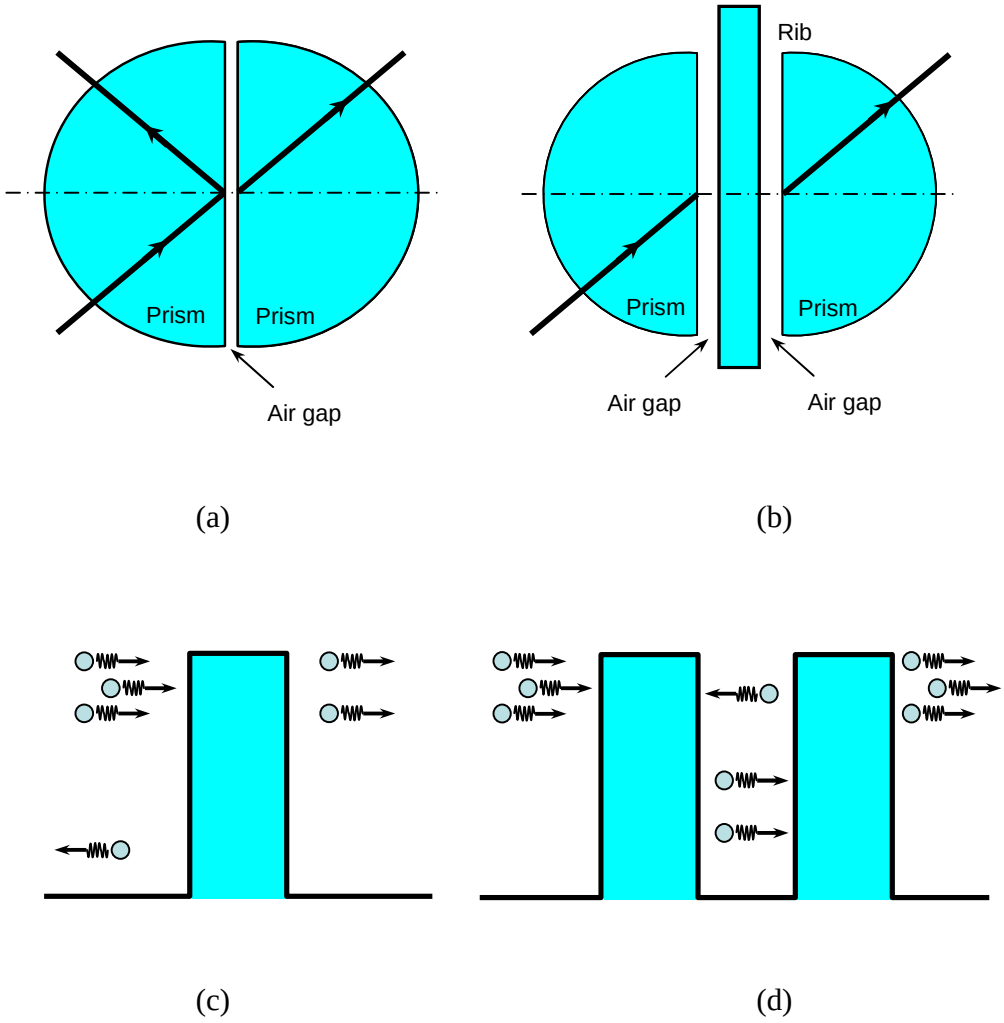

Fig. 3.1: Optical barrier structures and their tunneling effects. (a) Top view of the single optical barrier structure that has a thin air gap sandwiched between two hemispherical prisms; (b) top view of the double optical barrier structures, which has an addition central rib in the middle and has two thin air gaps; (c) optical tunneling effect through the single optical barrier, which can have only partial transmission; and (d) optical tunneling effect through the double optical barriers, which supports full transmission due to the resonance between the barriers.

The actually relationship should be analyzed as below. It should be noted that the radius of the prisms is much larger than the air gap width. The choice of the hemi-spherical shape is for the convenience of implementation. With proper parameters, the prism can act as a focus lens to collimate the light to be an exactly plane wave before hitting the air gap. The plane incident wave is critical to the uniformity of optical tunneling. The design of the hemi-spherical prisms is discussed in the next section §3.2.

3.1.2 The transfer matrix analyses on FTIR tunneling structures.

The analytical model of the double barriers is shown in Fig. 3.2. For simplicity, the two air gaps are chosen to be identical and the prisms are also identical. Besides, the prisms and the central rib share the same material. The air gap width and their distances are expressed as d and g respectively. In this letter, it is assumed to be silicon material, which has a refractive index n = 3.42 and a corresponding critical angle θ_c = 17.0 degrees. The transmission of the double barriers can be derived by the transfer matrix method. In the first step, the transfer matrix of a single barrier (the right half of Fig. 3.2) should be derived. The reflection coefficient R can be expressed as [161]

$$R = \frac{r_{10} + r_{02} e^{i\delta}}{1 + r_{10} r_{02} e^{i\delta}} \tag{3.1}$$

where r_{mn} and t_{mn} (m, n = 0, 1 or 2) are the reflection coefficient and transmission coefficient at different interfaces given by Fresnel equations. The phase term δ is given by

$$\delta = (4\pi d/\lambda)\sqrt{1 - n^2 \sin^2\theta} \tag{3.2}$$

Where d is the width of air gap and λ is the wavelength.

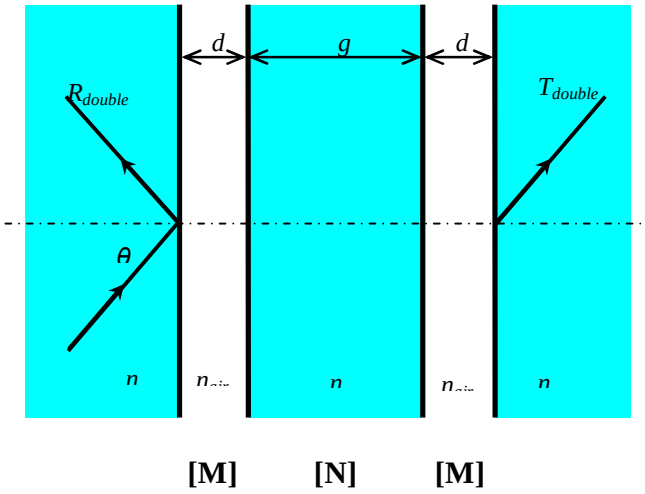

Fig. 3.2. Analytical model of the double optical barrier structure.

Due to the above critical angle condition, the phase shift of the light traveling through the air gap is imaginary which is resulted in the attenuation of the light amplitude. Therefore, the transmission coefficient T can be written as

$$T = \frac{t_{10}\, t_{02}\, e^{i\Delta}}{1 + r_{10} r_{02}\, e^{i\delta}} \tag{3.3}$$

where $e^{i\Delta}$ is the amplitude coefficient representing the attenuation of the light each time tunneling through the air gap which can be calculated as

$$e^{i\Delta} = \sqrt{\frac{1 - \left|\frac{r_{10} + r_{02}e^{i\delta}}{1 + r_{10}r_{02}e^{i\delta}}\right|^2}{\left|\frac{t_{10}t_{02}}{1 + r_{10}r_{02}e^{i\delta}}\right|^2}} \tag{3.4}$$

After certain derivation, the transfer matrix M for the single optical barrier can be expressed as

$$M = \begin{bmatrix} \frac{T^2 - R^2}{T} & \frac{R}{T} \\ -\frac{R}{T} & \frac{1}{T} \end{bmatrix} \tag{3.5}$$

In a similar way, the transfer matrix N of the central rib can be written as

$$N = \begin{bmatrix} e^{i\phi} & 0 \\ 0 & e^{-i\phi} \end{bmatrix} \tag{3.6}$$

where ϕ is the phase shift when the light travels through the rib.

With the transfer matrices of the air gap part and the central rib part, the overall transfer matrix M_{double} for the double optical barriers structure can be calculated as

$$M_{double} = MNM = \begin{bmatrix} m_{11} & m_{12} \\ m_{21} & m_{22} \end{bmatrix} \tag{3.7}$$

Therefore, the reflection coefficient R_{double} and the transmission coefficient T_{double} can be written as

$$R_{double}(n, d, g, \theta) = (-{}^{m_{21}}/_{m_{22}})^2 \tag{3.8}$$

$$T_{double}(n, d, g, \theta) = \left(\frac{m_{11}m_{22} - m_{12}m_{21}}{m_{22}}\right)^2 \tag{3.9}$$

It can be seen from Eq. (3.9) that the transmission coefficient is the function of four parameters, n, d, θ and g (the central rib width). Here d and g can be normalized with respect to the incidence wavelength so that the variable λ is not reflected in Eqs. (3.8) and (3.9). It should be point out that the distance between the air gaps cannot be too large so that it will not cause large space shift between reflected waves.

3.1.3 Transmission versus incidence angle

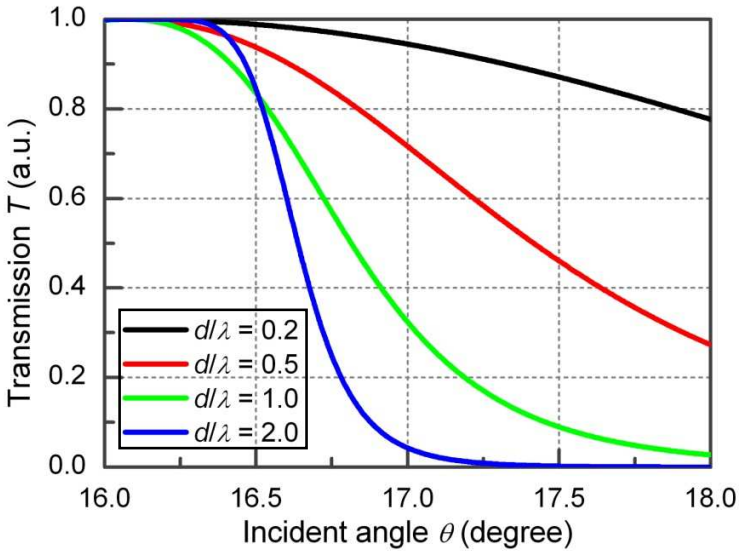

(a)

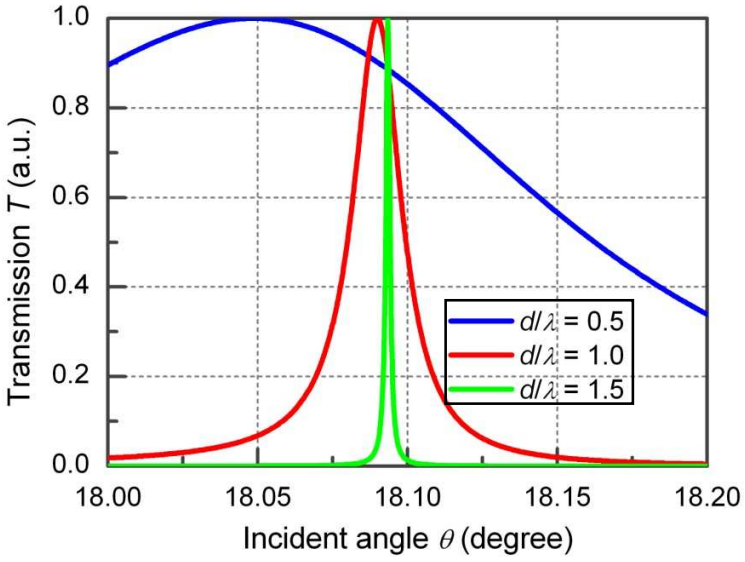

(b)

Fig. 3.3: The transmission versus incident angle at different air gap distances for both (a) single optical barrier and (b) double optical barrier.

The incident angle θ is one of the key parameters which determine the penetration energy of the photons passing through the optical barriers. The incident photons can penetrate the optical barriers with certain probability in form of evanescent waves. Generally speaking, the increasing of the incident angles reduces the penetration depth of the evanescent waves thus decrease the transmission of the optical barriers. The transmissions versus the incident angle for both (a) single and (b) double optical barriers are plotted in Fig. 3.3.

Fig. 3.3(a) shows the transmission of the single barrier when the incident angle θ is ranged from 16° to 18°. Here the refractive index of the hemi-spherical prism is set to be 3.42 which is the refractive index of silicon at infrared region (the critical angle θ_c is 17°.). The incident light in Fig. 3.3(a) is transmitted through the single optical barrier via refraction when $\theta < 17°$. In fact, the FTIR structure shown in Fig. 3.1(a) is not an optical barrier yet since it doesn't oblique the light. The optical barrier is formed when $\theta > 17°$. The transmission of the light is depended on the tunneling effect. It is shown in Fig. 3.1(a) that the transmission of the single optical barrier structure is decreasing as θ is increasing. The most rapidly drop of the transmission occurs near 17° where the total internal reflection happens. The ratio of the transmission drop to the incident angle change $\Delta T/\Delta\theta$ is depended on the width of the air gap *d*, because the larger the *d* is the smaller the transmission probability of the photons. Fig. 3.3(b) shows that the transmission of double optical barriers is not monotone decreasing as θ is increasing. The transmission can become 100% if the incident angle satisfies the resonance tunneling condition. The increasing of the air gap width decreases the full width at half maximum

(FWHM) of the transmission curve. It should be pointed out that the simulation range of Fig. 3.3(b) is from 18° to 18.2° which is different from that of Fig. 3.3(a). That is because the transmission of the double optical barriers structure is more sensitive to the incident angle change than that of the single optical barrier. The simulation range has to be decreased to resolve the transmission peaks. The transmission at the incident angle below the critical angle is shown in the later sections §3.5 and §3.6 which is not further discussed here.

3.1.4 Transmission versus the air gap distance

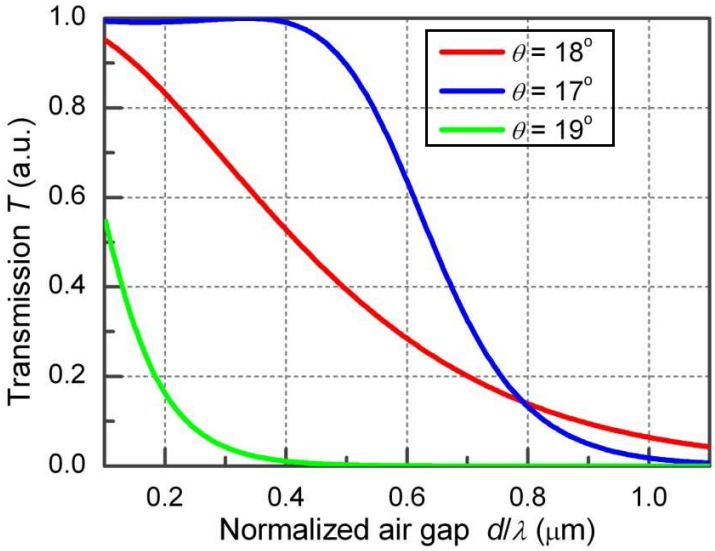

(a)

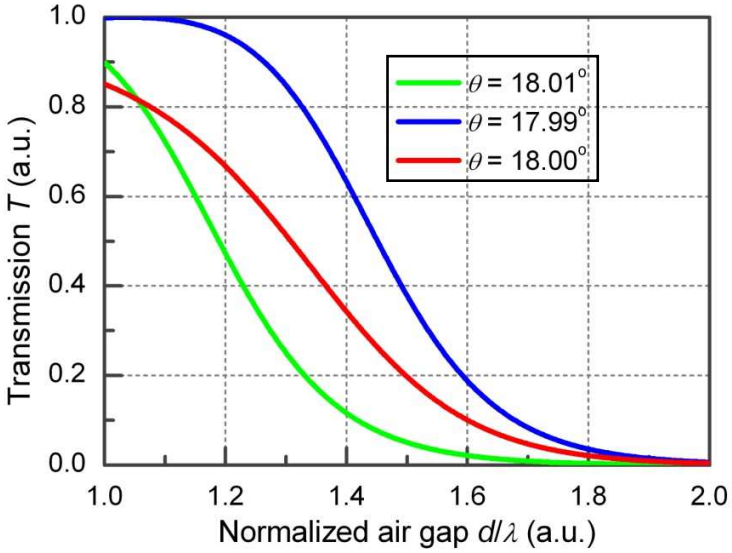

(b)

Fig. 3.4: The transmission versus air gap *d* at different incident angle for both (a) single optical barrier and (b) double optical barrier.

The transmissions at different incident angles for both Fig. 3.4(a) single optical barrier and Fig. 3.4(b) double optical barrier is inversely proportion to the air gap width *d*. Fig. 3.4(a) shows the transmission of the single barrier can drop from 100% to 0% when *d* changes from 0 to λ. The transmission of both single and double optical barrier can be eliminated when the change of the air gap distance $\Delta d > \lambda$. The ration of the transmission drop versus the air gap change $\Delta T/\Delta d$ of the double optical barrier structure is more sensitive to the incident angle than that of the single optical barrier structure.

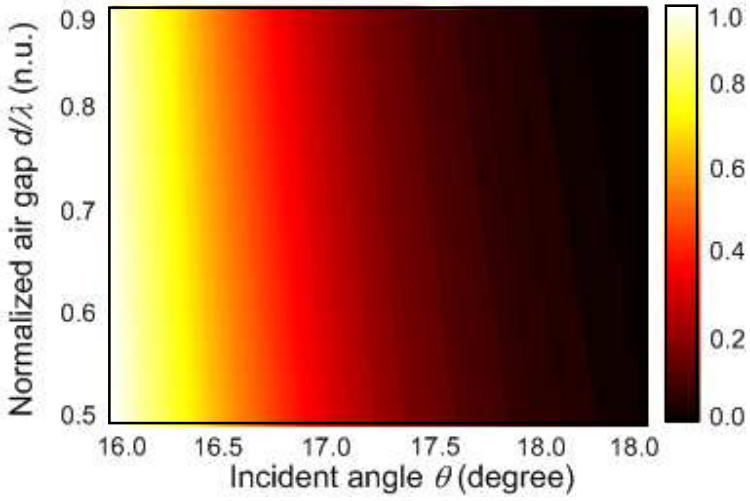

Fig. 3.5: The contour map of single barrier transmission at different incident angles and air gaps.

The effects of air gap *d* and incident angle θ on single barrier transmission is shown in Fig. 3.5. The bright parts represent the high transmission region while the dark parts represent the low transmission region. The simulation range of the incident angle is from 16° ($< \theta_c$) to 18° ($> \theta_c$) and the range of the air gap is from 0.5 λ to 0.9 λ. The single barrier transmission can be tuned from 100% to 0% by changing the incident angle. The

$\Delta T/\Delta\theta$ becomes maximum near the critical angle. However, the effects of the air gap change becomes obvious only at above the critical angle region when the transmission is depend on the tunneling other than the refraction. Therefore, the tuning of the incident angle of the single barrier structure can be used as the variable optical attenuator (VOA) or the optical switch. The air gap tuning of the single barrier structure has potential applications on VOA. The switching effect of the air gap tuning is not as good as that of the incident tuning. However, the linearity of the air gap tuning is better since there is not any abruptly drop of transmission near the critical angle.

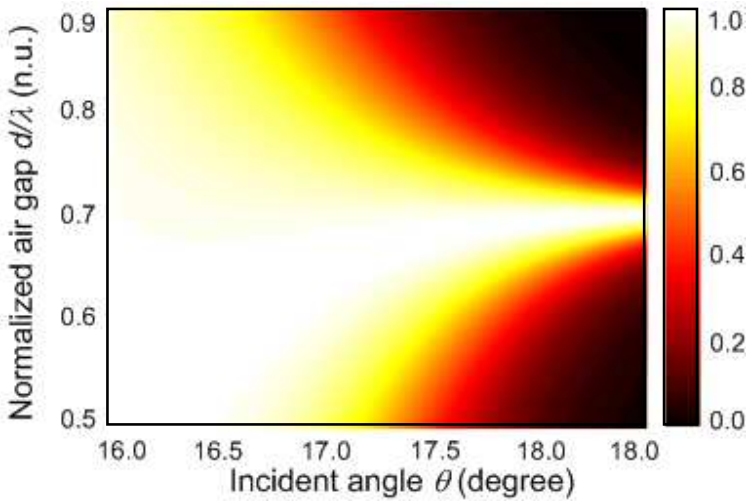

Fig. 3.6: The contour map of double optical barriers transmission at different incident angles and air gaps.

The effects of air gap d and incident angle θ on double optical barriers transmission is shown in Fig. 3.6. The bright parts represent the high transmission region while the dark parts represent the low transmission region. The simulation range of the incident angle is from 16° ($< \theta_c$) to 18° ($> \theta_c$) and the range of the air gap is from 0.5 λ to

0.9 λ. The change of the transmission by either the air gap tuning or the incident angle tuning is not obvious because the incident light is transmitted through via refraction other than the tunneling. However the high transmission region is limited within a very narrow region as the incident angle is larger than the critical angle. The tuning of the incident angle and the air gap of the double optical barrier structures has applications on both the optical switch and VOA.

3.1.5 Transmission versus the refractive index change.

Although the air gap width and the incident angle can be changed using MEMS system, the most stable and fast way to tune the micro-scaled devices is changing the refractive index of the device compositing materials. However, this tuning method is limited by the properties of the compositing materials. In this project, the demonstrated devices are all silicon based devices realized by MEMS technology. Here, the effects of refractive index change on the transmission of both single and double optical barriers are numerically analyzed. The experimental demonstration of such thermo tuning devices will be shown in §3.2 to §3.6.

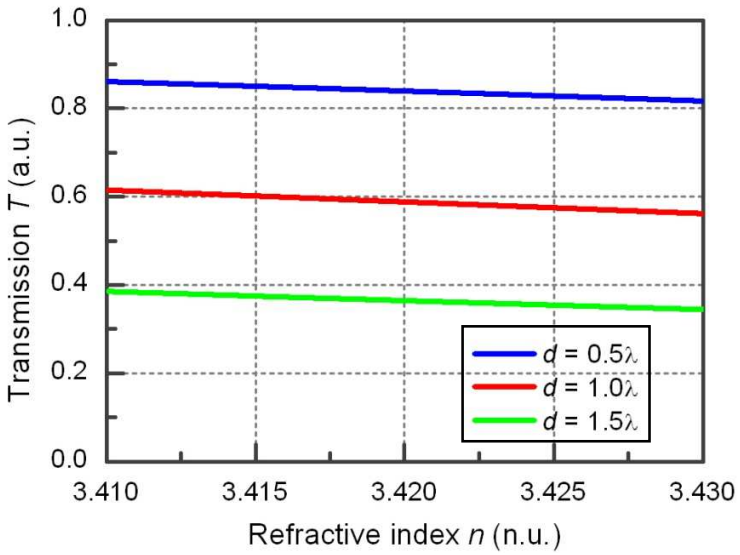

Fig.3.7: The transmission versus the refractive index change of single barrier structure.

Fig. 3.7 shows the transmission versus the refractive index change of single barrier structure at different incident angles. Since the refractive index of silicon is near 3.42 at infrared region, the simulation range of the refractive index is from 3.410 to 3.430 which is the 3.420 ± 0.010. The incident angle is chosen to be above the critical angle

(18°) so that only the transmitted light via tunneling are considered. The transmission is simulated when the air gap width *d* is chosen to be 0.5 λ, 1.0 λ and 1.5 λ respectively. It is shown in Fig. 3.7 that the transmission is almost linear to the refractive index in this region. The transmission change is only around 10% which is too small for applications such as variable optical attenuator (VOA) or optical switch. It should be point out that, if the incident angle is chosen to be near the critical angle, it is possible to change the critical angle by changing the refractive index of the compositing material. The incident light transmission can be changed from refraction to the tunneling which can have a larger tuning range.

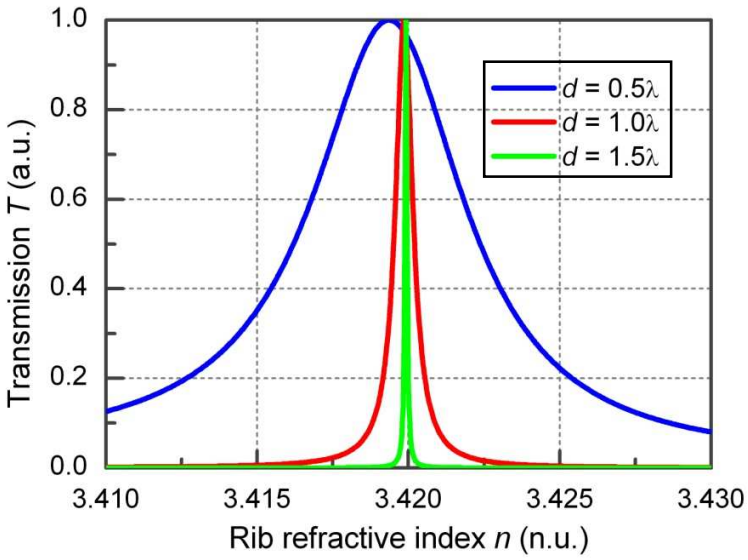

Fig. 3.8: The transmission versus the refractive index change of double barrier structure at different air gap width.

The transmission versus the refractive index change of double barrier structure at different incident angles is shown in Fig. 3.8. The simulation range of the refractive index is from 3.410 to 3.430 which are the same as Fig. 3.7. The incident angle is chosen

to be above the critical angle (18°) so that only the transmitted light via tunneling are considered. The transmission is simulated when the air gap width *d* is chosen to be 0.5λ, 1.0λ and 1.5λ respectively. Different from the single barrier transmission, the tuning range of the double barrier transmission is above 90%. The FWHM of the transmission spectrum become narrower when the air gap width is increasing. The tuning of the transmission of the double optical barrier structures can be 100% at the refractive index change less than 0.005.

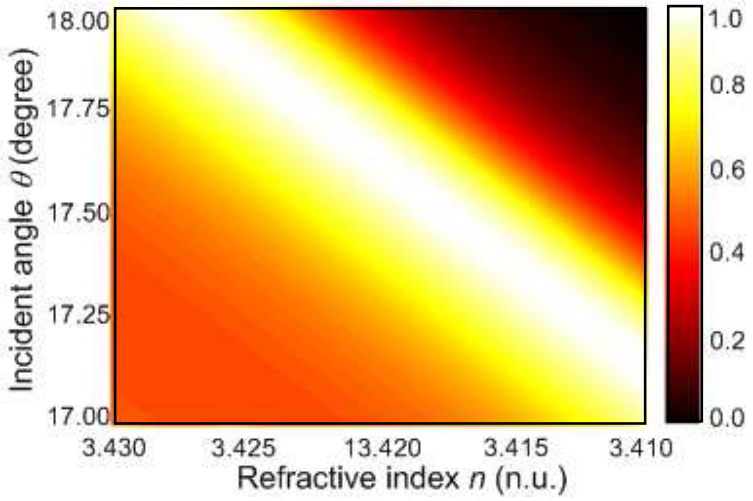

Fig. 3.9: The contour map of single barrier transmission versus the incident angle and refractive index.

The single barrier transmission at different incident angle and refractive index is shown in Fig. 3.9. The bright part represents the high transmission region and the dark part represents the low transmission region. The simulation range of incident angle is from 17° to 18° degree which is above the incident angle. The refractive index is changed from 3.410 to 3.430 which are 3.42 ± 0.010. It can be seen from Fig. 3.9 that the high

transmission region is at lower frequency and higher refractive index region. The refractive index change can change the critical angle of the silicon-air interface which makes the incident angle change has the same effects on the transmission as the refractive index change. The $\Delta T/\Delta n$ becomes maximum near the critical angle when the transmission is changed from tunneling effect to refraction. It should be point out that the interfaces between the two prisms (Fig. 3.1(a)) actually form a FP cavity which can enhance the transmission of the refraction. It explained why the transmission is not increased monotonously as the refractive index is increasing.

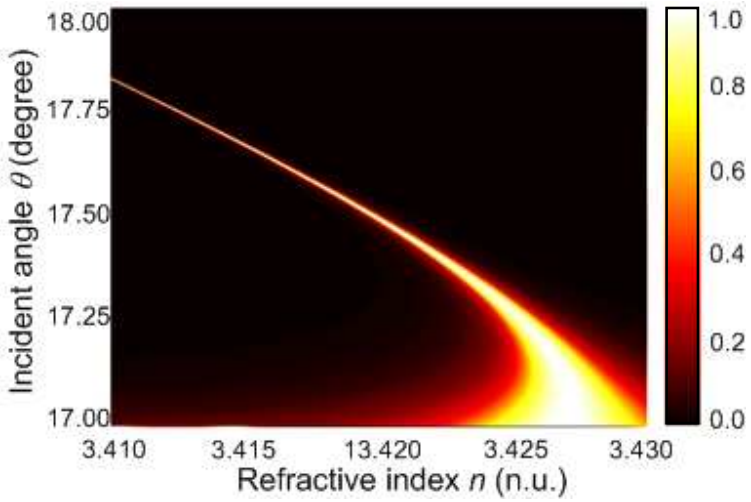

Fig. 3.10: The contour map of double barrier transmission versus the incident angle and refractive index.

The double barrier transmission at different incident angles and refractive indexes is shown in Fig. 3.10. The bright part represents the high transmission region and the dark part represents the low transmission region. The simulation range of incident angle is from 17° to 18° degree which is above the incident angle. The refractive index is changed

from 3.410 to 3.430 which are 3.42 ± 0.010. It can be seen from Fig. 3.9 that the high transmission region becomes narrower as the incident angle is increasing. The resonance tunneling condition is quite sensitive to both the refractive index and incident angle. Therefore, a small variation of the incident angle or refractive index can result in the sudden change of the transmission near the high transmission region.

3.1.6 Transmission versus the central rib width.

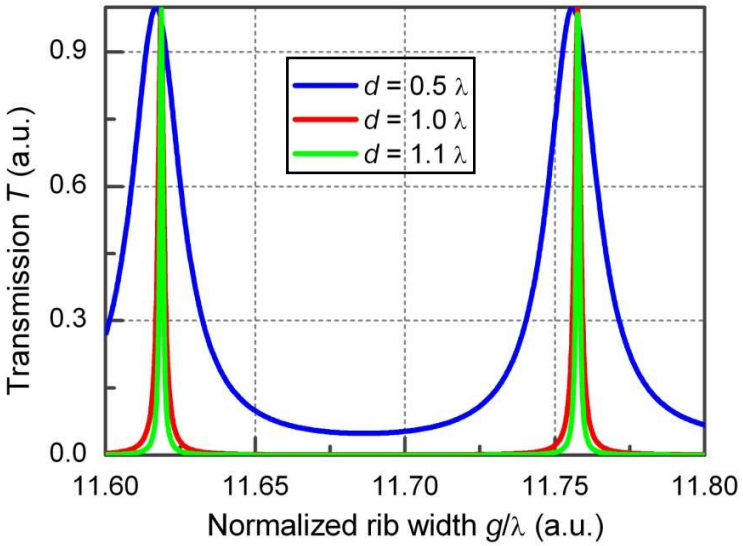

Fig. 3.11: The transmission versus the central rib width *g*.

The transmission as the function of the normalized central rib width *g* is shown in Fig. 3.11. The simulation range of the g is from 11.60 λ to 11.80 λ. The incident angle is set to be 18°. The transmission has periodical peaks as *g* is changing. It is because that the tunneled light is resonance within the central rib. The resonance condition is dependent on the optical length of the central rib. Therefore, the variation of the central rib width affects the transmission coefficient of the incident light. The position of the transmission peak is not affected much by the air gap distance *d*. However the FWHM of the transmission peak is affected by *d*. The larger the *d* is the narrower the FWHM of the transmission peak is. In other works, the sensitivity of the transmission on the variation of *g* is depended on d.

It can be summarized from Fig. 3.5, 3.6, 3.9 and 3.10 that, both the single barrier structure (Fig. 3.1(a)) and the double barrier structures (Fig. 3.1(b)) have applications on

optical switch and the VOA. As shown in Eq. 3.9, the transmission depends on incident angle θ, air gap distance d, refractive index n and the central rib width g. The transmission of the single barrier structure is mainly dominated by the way the incident light is transmitted (refraction or tunneling). Therefore, the transmission coefficient is determined by whether the incident angle is above or below the critical angle. In general, the double optical barrier structure is more sensitive to the parameters change than the single barrier structure do. Therefore, it can be used as optical switch or sensor which is required to have high sensitivity or fast switching speed. Furthermore, the sensitivity of the double optical barrier structure can be adjusted by optimizing the parameters such as g, θ and d. For example, if a double barrier optical switch is designed by changing the refractive index of the central rib width g, the refractive index change Δn required to have the switching effect can be adjusted by changing the air gap distance d which determines the sensitivity of the transmission on central gap width g (Fig. 3.11). In the following sections, the MEMS optical devices based on double barriers optical tunneling effects will be demonstrated.

3.2 MEMS thermo-optical switch

3.2.1 Design of the thermo-optical switch

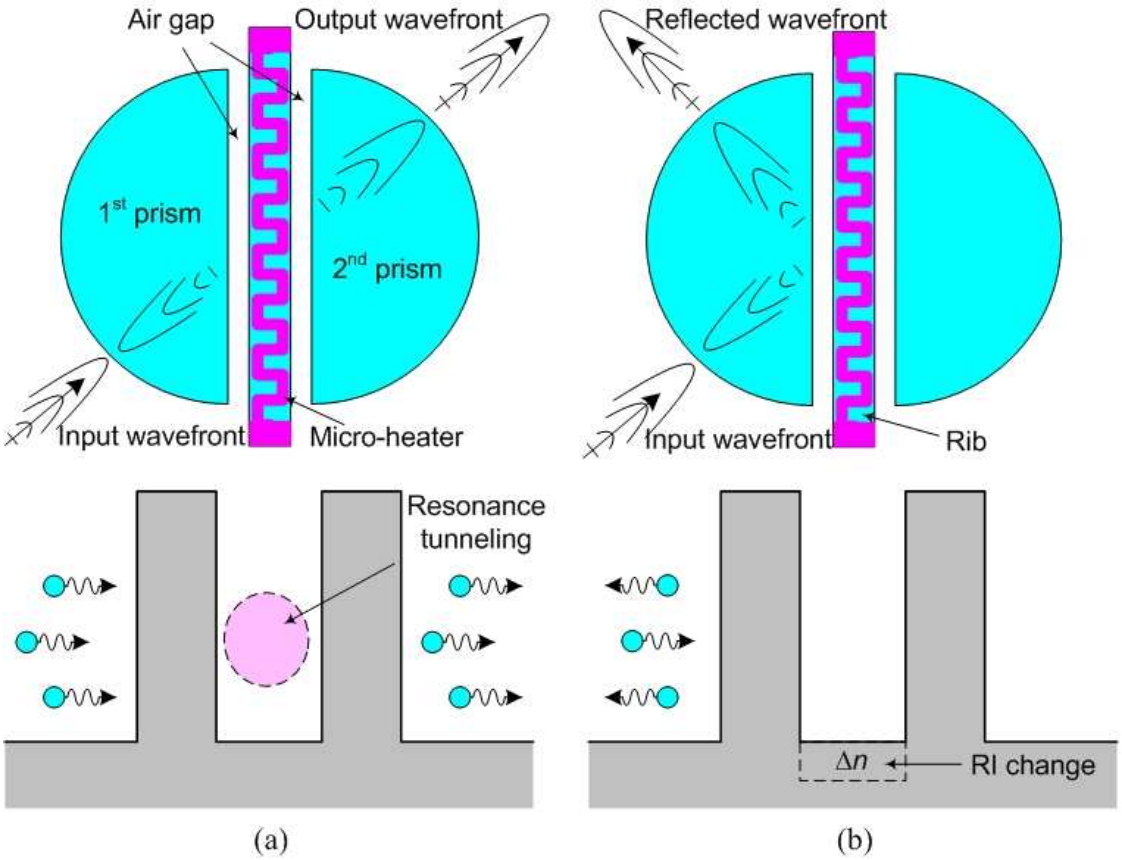

Fig. 3.12: Design and working principle of the optical double-well structure. (a) Top view and potential diagram in the ON state; (b) Top view and potential diagram in the OFF state.

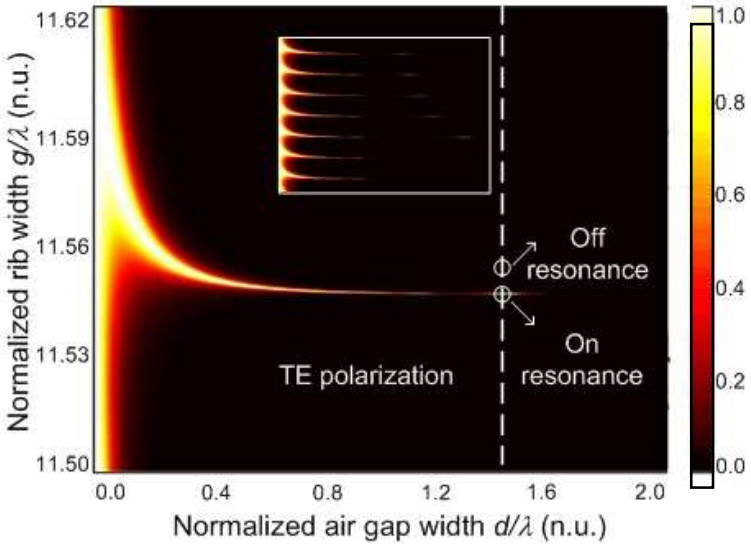

(a)

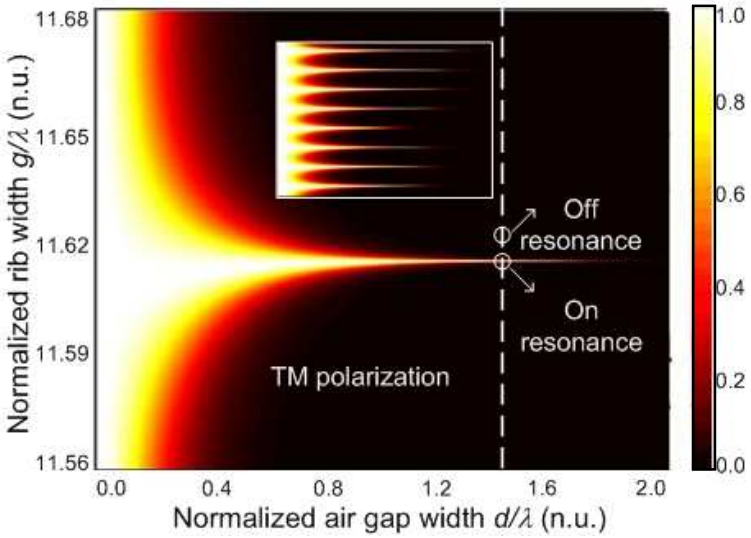

(b)

Fig. 3.13: Contour map of (a) TE and (b) TM light transmission as functions of d/λ and g/λ. Inset shows Transmission states of larger region.

The design and switching process of the thermo-optic switch is illustrated in Fig. 3.12 [162]. The double-well structure is consist of two hemi-cylindrical silicon prisms, two air gaps and a silicon rib, and maintains symmetry in the horizontal direction as shown in Fig. 3.12. The air gaps function as two optical barriers as the refractive index of air is smaller than that of silicon.

The corresponding optical potential diagrams are shown in Fig. 3.12. The rib region acts as a resonant cavity between the two optical wells. The resonance condition is highly dependent on the optical path length$L = n \cdot g$, where n is the refractive index of the rib and g is the physical length of the rib. A micro-heater is deposited on top of the rib region for adjusting the refractive index of the rib. In the initial state (Fig. 3.12(a)), the transmission reaches its maximum by choosing the proper parameters, corresponding to the ON state. The switching process is achieved by heating up the rib region. The increase of the rib's refractive index breaks the resonance condition and thus shut off the light transmission of the outputs (Fig. 3.12(b)), corresponding to the OFF state.

To obtain a maximum transmission for the initial state, it is necessary to choose the proper parameters. Due to the symmetry, the double-well construct in Fig. 3.12 has only 3 independent parameters for setting the initial operation condition, i.e., the incident angel θ, the normalized air gap width d/λ and the normalized rib width g/λ. The wavelength λ is not an independent variable since it can be normalized into d and g. Due to the use of silicon material, the refractive index n of the prisms and the rib is also fixed (here n = 3.42 for silicon). As the transfer matrix method has been proven effective in studying the multi-layered structures, it is adopted to analyze the double-well construct.

Following this method, the characteristic matrix M_{DB} of the optical double barriers switch can be expressed as,

$$M_{DB} = MNM = \begin{bmatrix} m_{11} & m_{12} \\ m_{21} & m_{22} \end{bmatrix} \tag{3.10}$$

where M and N are the characteristic matrices of the single well and the rib region, respectively.

Then the reflection and transmission can be determined from the matrix elements m_{ij} (i, j = 1 or 2). The incident angle θ is chosen to be 18°, greater than the critical angle 17°. So the transmission is only dependent on d/λ and g/λ. Fig. 3.13 shows the contour map for the TE and TM wave. The bright region represents high transmission while the dark part means low transmission. In Fig. 3.13(a), the transmission of the TE polarization is close to 100% when it has $d/\lambda < 0.05$ (the white region on the left side). This is because the thin air gap can be easily penetrated by incident light. Most of the light just travels through the gaps instead of being reflected back or resonating between the air gaps. Sharp peak can be observed when it has $d/\lambda > 1.2$, implying the transmission is very sensitive to the width of the central rib. By analogy, the air gap width is equivalent to the potential to the electron tunneling barriers. As the air gap is increased, more and more photons are reflected back by the interfaces. The width of central rib is actually the length of the resonance cavity between the two barriers and thus it determines how well the reflected light waves can cancel each other. This is why the transmission becomes more and more dependent on the central rib width when the air gap is widened up. The inset in Fig.

3.12(a) shows a larger range of central rib width. It can be seen that the peaks appear periodically with respect to the change of rib width. Such periodicity is a strong evidence of the existence of resonance between barriers. The sharpness of the peaks also implies that the central rib and the air gap should be carefully chosen to reach the full transmission condition. For the TM polarization, the periodicity and sharp peaks also exist as shown in Fig. 3.12(b) and its inset.

It can be observed that a sharp peak appears in between g/λ = 11.54 – 11.56 when it has d/λ > 0.4. And the peak narrows down with the increase of d/λ. The inset figure shows a larger range of the rib width. The peaks appear periodically with respect to the change of the rib width. This periodicity provides evidence on the existence of resonance between optical wells. The sharpness of the peaks implies that the transmission is very sensitive to the rib width change. And it should be equally sensitive to the rib's refractive index change since the rib width and refractive index have the same contribution to the optical path length. This is the physical mechanism that facilitates the thermo-optic switching by heating up the rib. Based on the numerical analysis using Eq. (3.10), the designed parameters are chosen to be g/λ = 11.55 and d/λ = 1.5 which ensure the high transmission (ideally lager than 99%) in the initial state and low refractive index change ($\Delta n = 2.57 \times 10^{-4}$) required by the switching process. For λ = 1550 nm, there are g = 17.9 μm and d = 2.3 μm.

The choice of the cylindrical shape of the prisms is for collimating the Gaussian waveform from the input fiber to the approximate plane waveform and converts the tunneled plane waveform into the output. As the plane wave is required during the

resonance tunneling between the two optical barriers, the radius of the output wave has to be as large as possible. According to the lens equations of the Gaussian beam, the input wavelength λ, the lens radius r and the distance between fiber and the input prism L satisfy,

$$r = \left(L + {Z_r^2}/{L}\right) * (n-1) \tag{3.11}$$

where Z_r is the Rayleigh length of the Gaussian beam $Z_r = \pi * w_0^2/\lambda$ where w_0 = 4.2 μm which is the waist radius of the Gaussian beam of the incident light in the experiment.

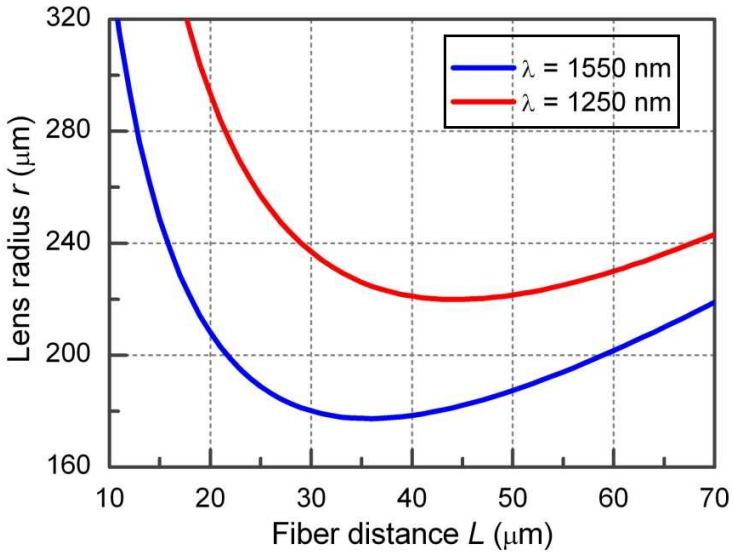

Fig. 3.14: The lens radius versus fiber distance at different incident wavelength.

The relation between the lens radius and the distance between fiber and the input prism is shown in Fig. 3.14. The best choice for the fiber distance is L = 34.5 μm and correspondingly r = 179 μm. It is because that $\Delta r/\Delta L$ = 0 which means the largest

tolerance to the fabrication imperfection. However, as the single mode fiber used in the experiment is around 125 mm wide and the incident angle is 18°, there is not enough space for the fibers if L = 34.5 μm. In this work, the distance between fiber and the input prism is chosen to be 170 μm. There are two solutions for this problem. One is removing the fiber which collecting the reflected light (Fig. 3.15). If the optical switch is designed to be two ported, the fiber for reflection is not compulsory in this design. The other solution is increasing the distance between the reflection fiber so that the input fiber can be put nearer to the input prism. An extra lens has to be put between the reflection fiber and the input prism. It will increase the loss between the reflection fiber and the input prism.

3.2.2 Fabrication of thermo-optical switch

After the design, the device is fabricated by deep reactive ion etching on a silicon-on-insulator wafer, which has a 75-μm structural layer bonded on a handling wafer through a 2-μm oxide layer. The overview of the fabricated thermo-optic switch is shown in Fig. 3.15 after the integration of three single mode fibers (one for input, one for reflection and another for transmission). Each of the two silicon prisms is supported by a bi-directional actuator. The core part of the switch is within a footprint of 400×400 μm^2. The micro-heater is formed by patterning a serpentine-shaped aluminum wire (0.2 μm thick) on top of the rib. The fiber grooves are etched to ensure the incident angle of 18º. The bi-directional actuator provides a maximum displacement of 5 μm in any direction under a driving potential of 6.8 V. The air gaps between the rib and prisms can be finely

adjusted by the tuning the driving voltage of the actuator for optimizing the initial working condition.

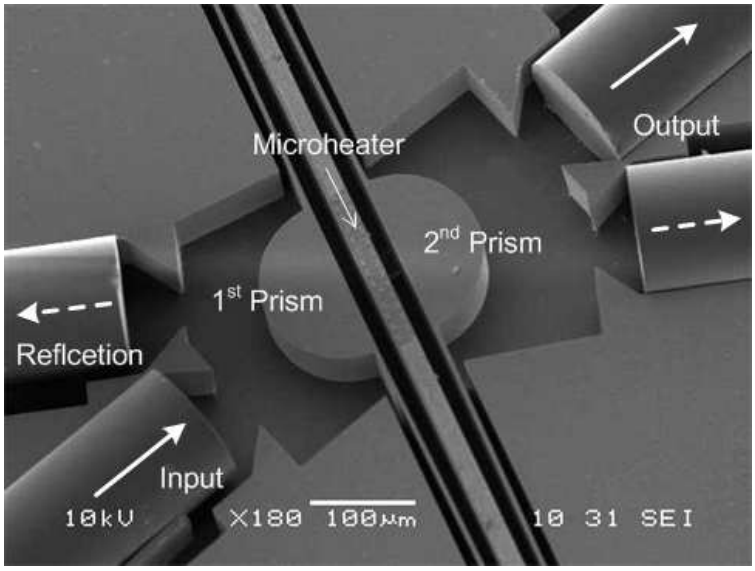

Fig. 3.15: Scanning electron micrograph of the fabricated thermo-optic switch.

At the initial state, both the TE and TM are fully transmitted. With the increase of $|\Delta n|$, the transmissions of both the TE and TM drop dramatically. At $|\Delta n| = 1 \times 10^{-3}$, the TE goes down to -41 dB while the TM goes to -25 dB. In this paper, TE polarization is chosen for the experiment for better sensitivity. In general, only a change in the refractive index of order 10^{-3} is required to achieve a contrast of transmission by 30 dB. For the silicon material, the refractive index change is approximately linear near the room temperature.

The refractive index change of the order 10^{-3} can be easily achieved by thermo effects. It should be noted that the change in the refractive index of the central rib is equivalent to the change in the width of the central rib since the resonance condition is

determined by the optical path length, which is a multiplication of the refractive index and the width of the central rib.

3.2.3 Experimental demonstration of thermo-optical switch

The experiment setup is shown in Fig. 3.16. The incident light is generated by a Tunable laser source with the wavelength tuning range from 1520 nm to 1620 nm. The incident light is input to and collected from the optical switch by single mode fibers which are fixed on the optical table during the experiment to maintain the polarization state of the input light. The micro-heater is pumped by a source measurement unit (SMU). The pumping current is around 50 mA. The transmitted light is collected by a photo detector which is connected to the optical spectrum analyzer (OSA) or the oscilloscope for further analyze.

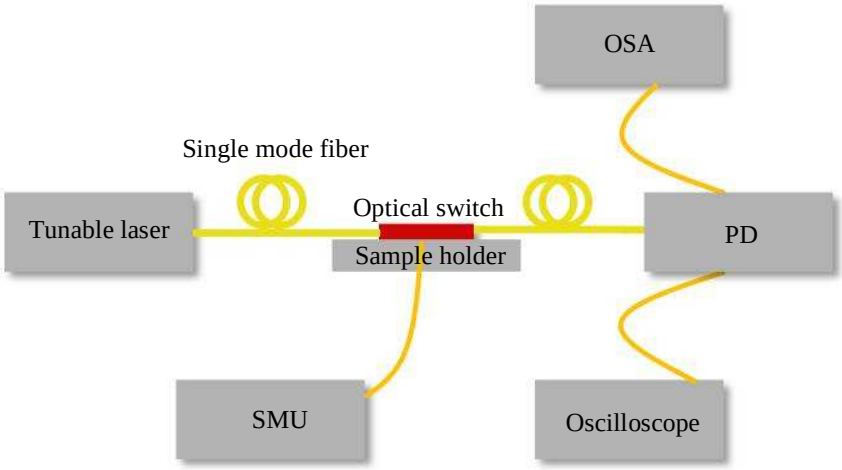

Fig. 3.16: Experimental setup of the thermo-optical switch

As there are always fabrication errors, the maximum transmission may not occur at the designed 1550 nm. Therefore the first step of experiment is to measure the transmission spectrum of the optical switch. The result is shown in Fig. 3.17. At room temperature, the peak transmission occurs at 1548.7 nm with a bandwidth of 0.8 nm. Correspondingly, the Q factor is around 2×10^3.

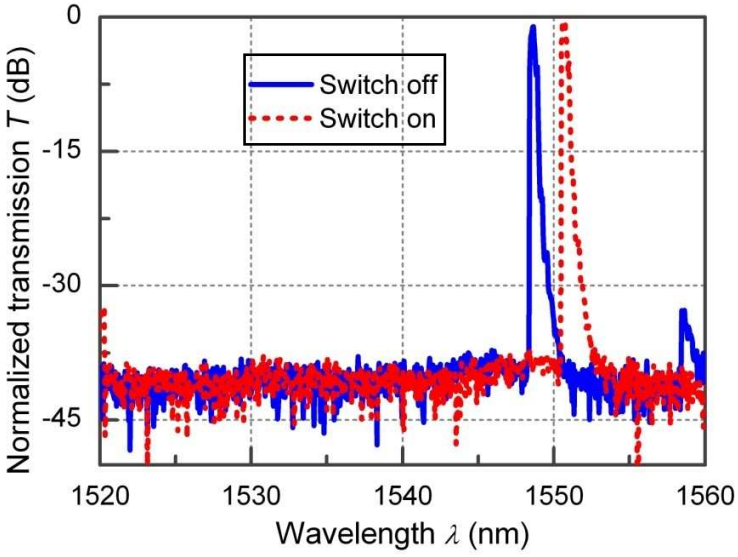

Fig. 3.17: Transmission spectrum of the optical switch. The blue solid line refers to the off-state of the optical switch and the red dotted line refers to the on-state.

According to the simulation, the Q factor on order of 10^4 which is one order lager than that of the experimental results. The discrepancy is mainly due to the lack of collimation in the vertical direction of the optical double barriers structure. When the rib region is heated up, the transmission spectrum would be changed. Fig. 3.17 shows that the peak wavelength is shifted by 2 nm when the micro-heater is under a static driving current of 75 mA.

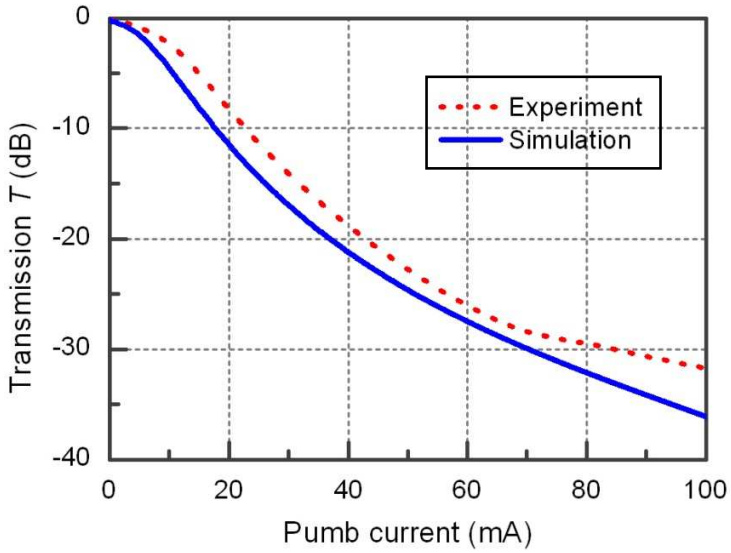

Fig. 3.18: The static tuning process of the thermo-optical switch. The transmission is measured at different pumping current. The red dotted line shows the experimental results and the blue line shows the simulation results.

The static switching characteristics are plotted in Fig. 3.18. The optical power is normalized with respect to the maximum output power. The insertion loss is around 10 dB. The incident light is from a laser light source (Ando AQ4321D) with an input power of 0 dBm. The wavelength follows the peak wavelength of the transmission spectrum as measured above. A polarization controller is used to maintain the TE polarization. The electrical current generated by a source measurement unit is applied to the micro-heater via micro-probes. Here the electric current is chosen as the control parameter because the actual temperature and refractive index change cannot be measured directly during the experiment. With the gradual increase of the heating current, the output power dropped dramatically. The measured extinction ratio is 31.7 dB, which roughly matches the predicted value of 35 dB given by the simulation.

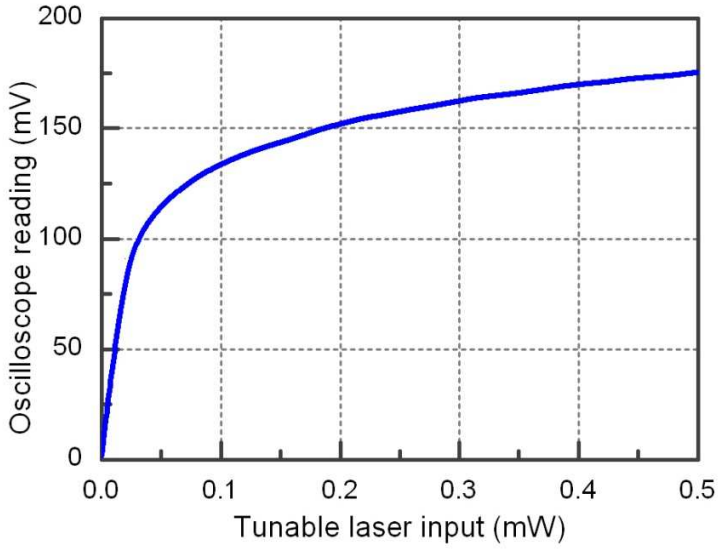

Fig. 3.19: The dynamic tuning process of the thermo-optical switch. The transmission is measured as the function of time. The blue solid line shows the optical output power

The switching process is monitored by an oscilloscope (TDS360) which is connected to the photo detector. The transmitted light is collected by the photo detector and the voltage signal is read by the oscilloscope. Firstly, the readings given by the oscilloscope is calibrated by the tunable laser source. It is shown in Fig. 3.19 that the reading of the oscilloscope is not linear to the input power of the light. Therefore, the measured signal from the oscilloscope has to be normalized by the measurement results shown in Fig. 3.19.

The dynamic switching process is shown in Fig. 3.20. Here a square voltage pulse of 10 V (duration 1 μs) from a waveform generator (HP 33120A) is applied to the micro-heater. The response time (ON to OFF state) is measured to be 1 μs, which is the same as the duration of the driven signal. This suggests that the response time could be further

decreased by a shorter driven voltage pulse. However the relaxation time (25 μs) of the optical switch is much longer than the response time due to the slow heat dissipation.

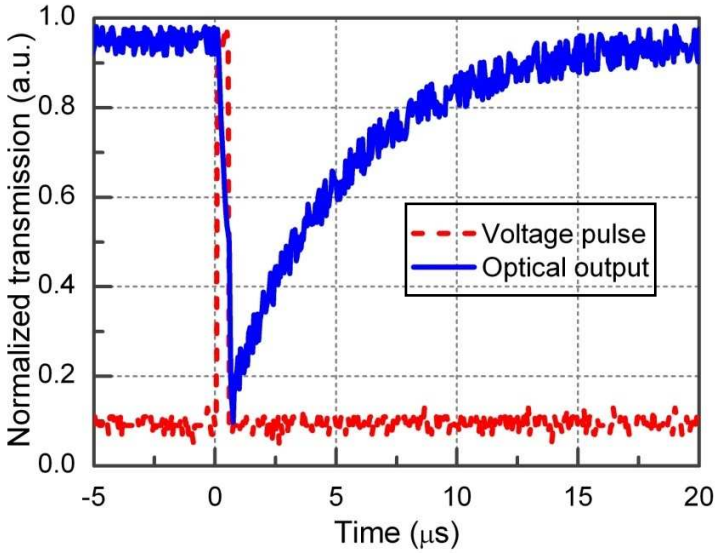

Fig. 3.20: The dynamic tuning process of the thermo-optical switch. The transmission is measured as the function of time. The blue solid line shows the normalized optical output power. The red dashed line shows the pumping voltage generated by the SMU.

In conclusion, this work has demonstrated a fast thermo-optic switching process by the resonant tunneling effect of a silicon micromachined optical double barrier structure. In the static and dynamic experiment, the extinction ratio of larger than 30 dB and the switching speed of 1 μs are achieved. The VOA function of such double barriers structure is also shown in Fig. 3.18. This thermo-optic switch design not only inherits the merits of the micromachining such as compact footprint, fine tuning structures and easy integration with the external fiber optics but also distinguishes itself by its fast switching speed, low power consumption and in-plane light modulation.

3.3 MEMS switchable polarizer

Traditional polarizer used in MEMS systems is prisms which refract or reflect the light regarding its polarization state. For example, when the incident angle of the light is equal to the Brewster's angle, only TE polarized light can be reflected. Therefore, the traditional PBS has two major drawbacks. One is the TE and TM polarized light is not totally separated in the refraction so that the extra component is needed to obtain the pure TM polarized light. The other drawback is traditional polarizer is not easy to be tuned. The main tuning method for the traditional MEMS polarizer is to change the incident angle by mechanically rotating the prisms which is not easy since the incident angle has to be precisely controlled [163].

As shown in Fig. 3.13, the resonance tunneling condition for TE and TM polarized light is different. Therefore, the double barriers structure is polarization selective. Although the resonance tunneling condition for both TE and TM polarized light are periodical, the period for TE and TM polarized light is the same. Therefore, the double optical barrier structure cannot transmit the TE and TM polarized light simultaneously no matter how its parameters been changed. For example, if the double optical barriers structure allows TE polarized light to transmit through, the TM polarized light will be reflected back which is functions as a polarization beam splitter. In the previous section, it has been demonstrated that the resonance tunneling condition can be tuned by changing the refractive index of the central rib. Therefore, it is possible to switch the tunneling condition between the TE light and TM light thus makes the PBS tunable.

3.3.1 Design of the MEMS switchable polarizer

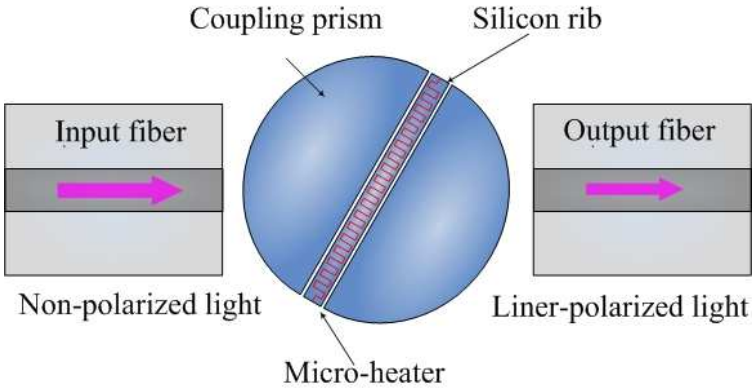

Fig. 3.21: The schematic of MEMS switchable polarizer

Fig. 3.21 shows the schematic of the MEMS switchable polarizer. It consists of three parts: an input and an output fiber, coupling prisms and a central rib. The spacing between the rib and the prisms are smaller than the working wavelength. The input fiber is aligned with the semi-cylinder prism so that non-polarized light can be incident on parallel surfaces above the critical angle and transmits through the polarizer via resonant enhanced optical tunneling effect which is highly sensitive to the polarization state of the incident light. It allows only one polarization state to pass through the polarizer while blocks the other. The required polarization state for the polarizer can be tuned to the perpendicularly direction via changing the refractive index of the central rib.

The transmission of the double barriers structure is simulated using transfer matrix method to choose the optimized parameters for the MEMS switchable polarizer. Since the polarizer is designed to be tuned by changing the refractive index of the central

rib only, air gap width of the design is fixed at 1.8 μm and the central rib width is chosen to be 18 μm.

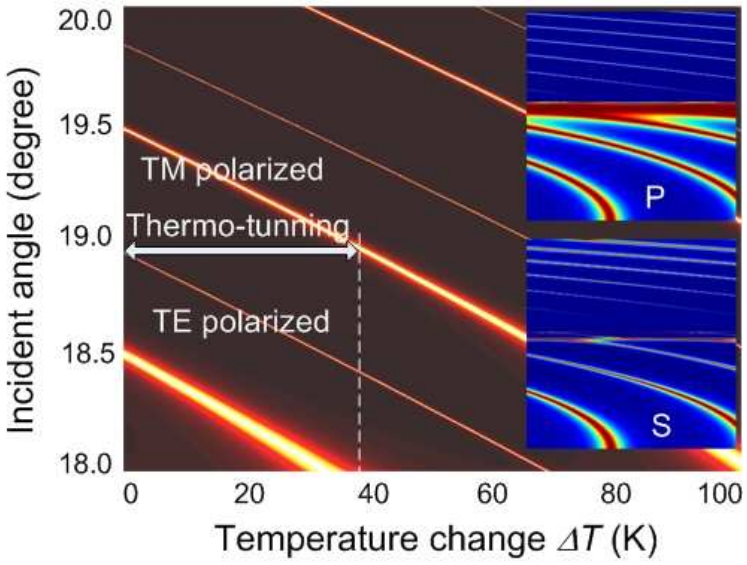

Fig. 3.22: Contour map on the transmission versus different temperature and incident angle for both TE and TM polarized light. Inserts show the large scale of the contour maps.

The contour map of the output laser power versus wavelength and refractive index change is shown in Fig 3.22. The bright color represents high transmission while the dark one stands for low transmission. It can be seen from the simulation results that both the transverse electric (TE) polarization and the transverse magnetic (TM) polarization have a bright stripe in the region of interest. The two stripes are separated but share the same inclination. The separation implies that it is not possible to get high transmission for both the TE and TM with a given combination of the refractive index change and the wavelength. In another word, the transmission is highly selective to the

polarization state. The inclination suggests that the wavelength of the laser output is red shifted with the increase of the refractive index of the central silicon. This acts as the fundamental mechanism for the wavelength tuning even though the cavity length between the fiber end and the HR laser facet does not change. It can be observed from Fig. 3.22 that the TE light have narrower stripe width than the TM light because the TM light is easier to penetrate the optical tunneling structure than the TE light due to the in-plane electric field.

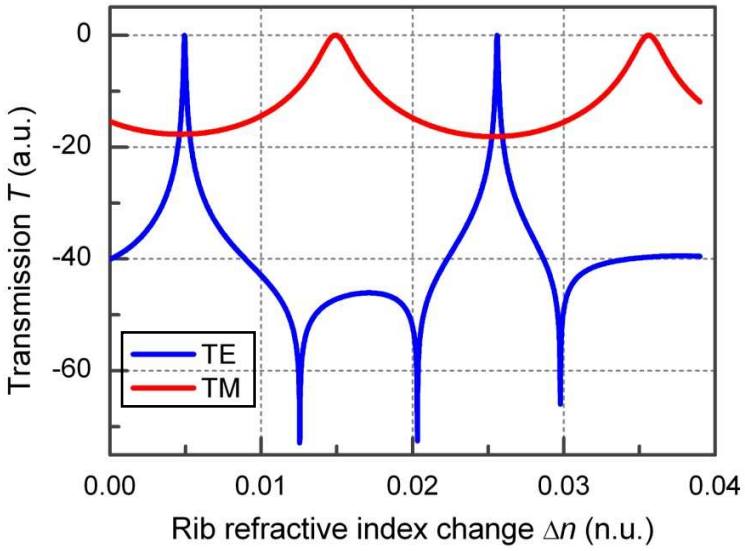

Fig. 3.23: The transmission as the function of the refractive index change of the central rib for the input wavelength at 1550 nm.

The numerical results are shown in Fig. 3.23 for the transmission of the optical tunneling structure versus the refractive index change of the central silicon layer. The incident angle is 18°. According to the simulation results, the polarization state remained unchanged when the refractive index change Δn is less than 0.01. Under this condition, the refractive index change only affects the wavelength of the peak transmission.

However, when the Δn is larger than 0.01, the polarization of the transmitted light is switched to its perpendicular position. Thus make the required polarization state for transmitted light changes from TE to TM. The free spectrum range (FPR) of the optical tunneling spectrum can reach 30 nm.

3.3.2 Fabrication of the MEMS switchable polarizer

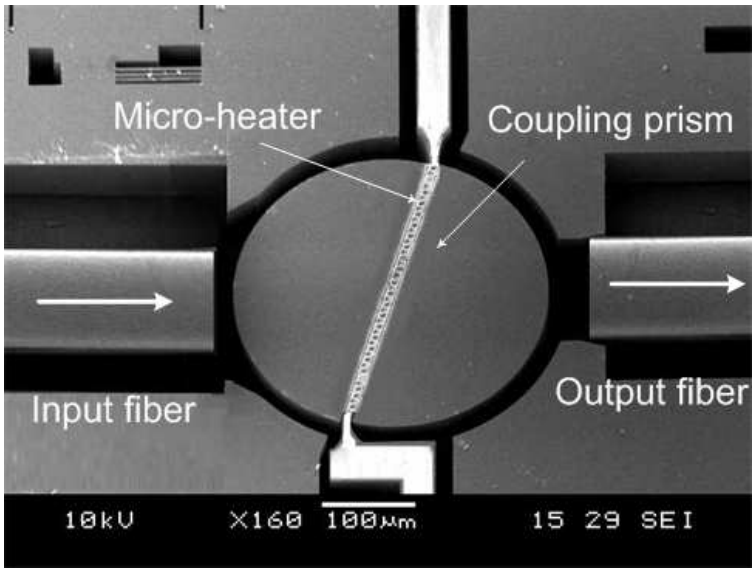

Fig. 3.24: Scanning electron micrograph of the fabricated switchable polarizer.

The overview of an integrated MEMS switchable polarizer is shown in Fig. 3.24 by a scanning electron micrograph (SEM). The whole structure is fabricated on a SOI wafer with a silicon structure layer of 75 μm thick. The input and output fiber is aligned by the fiber groove. The semi-cylinder shaped prism is fabricated to have a radius of 170 μm for the optimal coupling of the light into the fiber. The distance of the fiber to the input prism is 34.5 μm which can be adjusted by the fiber stage during the experiment. The air gap between the central silicon layer and the prism is 0.9 μm and the central

silicon layer is 30 μm wide. The incident angle of the light is 18°, larger than the critical angle of 17° for the silicon/air interface. The output fiber is connected to an optical spectrum analyzer (OSA) to monitor the alignment of the device. The position of the fiber is adjusted by the fiber stage until a single mode output with relatively strong power is achieved.

3.3.3 Experimental results and discussions

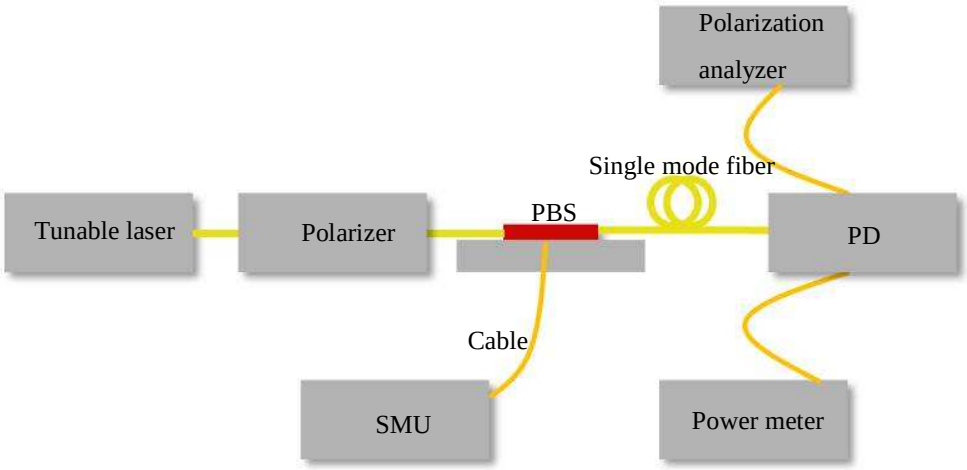

Fig. 3.25: The experimental setup of the MEMS switchable polarizer

The experimental setup is similar as that of the thermo-optical switch which is shown in Fig. 3.16. The incident light is generated by a tunable light source ranged from 1520 nm to 1620 nm and the polarization state of the incident light is controlled by a polarizer. The polarizer is not necessary during the practical application of the switchable polarizer. During the measurement the incident polarization is controlled to demonstrate the transmission coefficient of different polarization state. The single mode fibers used to guide light from the tunable laser source to the switchable polarizer and then to the

polarization analyzer are fixed on the optical table to maintain the polarization state of the light. The SMU is used to pump the micro-heater of the PBS thus control the refractive index of the central rib. The transmitted light is analyzed by the optical power meter for the transmission at different polarization states. A polarization analyzer is used to analyze the polarization state of the output light.

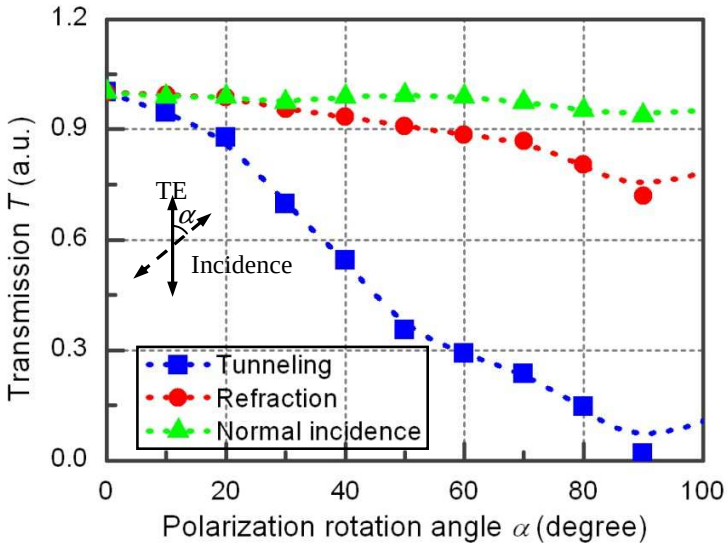

Fig. 3.26: The normalized transmission versus the polarization rotation angle at different incident angles. The green triangle, red circular and blue square represent the normal incidence $\theta = 0°$, refraction $\theta = 10°$ and tunneling $\theta = 18°$ respectively.

The normalized transmissions versus the polarization rotation angle at three different incident angles are measured to illustrate the polarization dependence on the incident angle. The polarization rotation angle means the angle between the electric field of the incident light and the TE polarized light (Fig. 3.26 inserts). The experiment is performed on the double barrier structure without the fiber groove which is shown in the insert SEM graph of Fig. 3.26. In this way, the incident angle can be tuned freely by the

fiber stage. The green triangle, red circular and blue square represent the normal incidence $\theta = 0°$, refraction $\theta = 10°$ and tunneling $\theta = 18°$ respectively. It is show in Fig. 3.26 that the polarization state has little effects on the transmission of the normal incidence. The variation of the transmission can be caused by the polarizer which controls the polarization state of the tunable laser source. The polarization states have a small effect on the transmission for the refraction when the incident angle is 10°. However, the transmission of the tunneling light is highly depended on the polarization state which means the double optical barriers structure can be used as a polarizer.

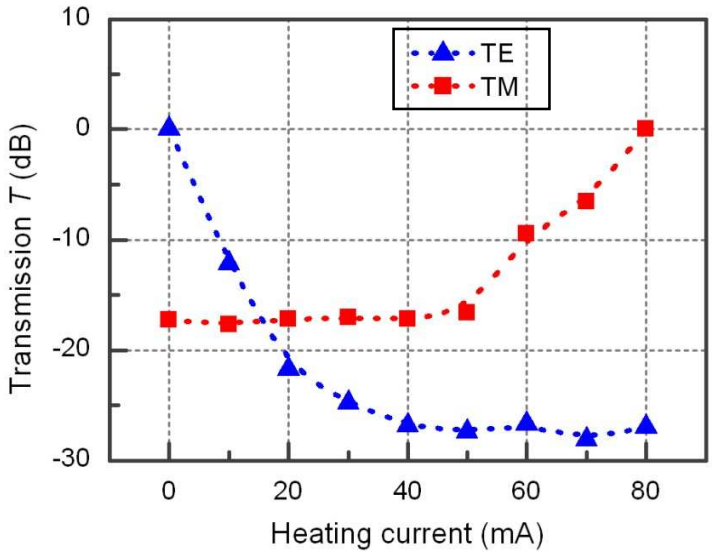

Fig. 3.27: The normalized transmission versus the heating current of the micro-heater. The blue triangle dashed line represents the TE polarized light and the red square dashed line represents the TM polarized light.

The normalized transmission of the incident light is measured under different pumping current of the micro-heater located on the central rib for both TE and TM polarization states. The heating current is ranged from 0 mA to 80 mA. The refractive

index change of the central rib cannot be measured directly since the device is of the micro-scale. The initial state the polarizer is to allow the TE polarized light to transmit through and reflect the TM polarized light. However, the transmission of TE polarized light is decreasing as the heating current is increasing. When the heating current is above 60 mA, the transmission of the TM polarized light become nontrivial and finally it increased to its maximum when the heating power is 80 mA.

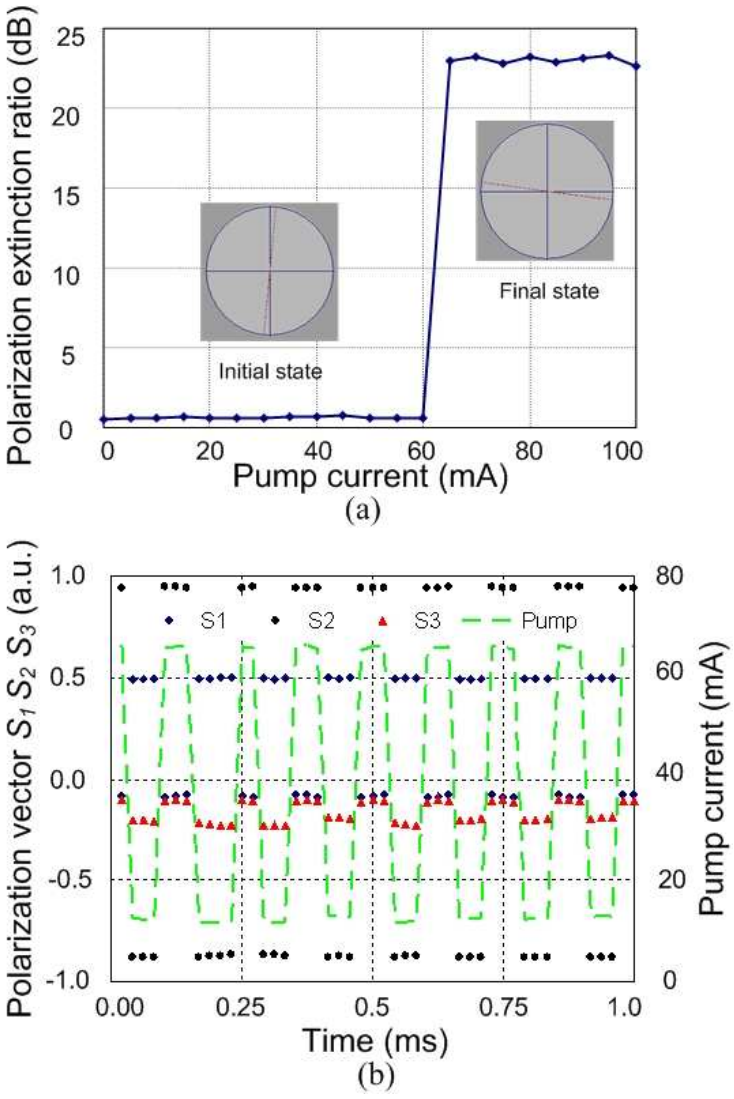

Fig. 3.28: Experiment results of MEMS switchable polarizer. (a) the static switching process of the PER as the pump current increase. (b) the dynamic response of the polarization state of the output when pumped with periodically changed heating current. The dashed line shows the time variation of the pumping current.

Fig. 3.28 shows the experimental results of the MEMS switchable polarizer. The polarization extinction ratio (PER) is defined as power ration of the TM polarized light to the TE polarized light which is measured using a polarization analyzer (POD-101A). The change of the PER between the initial and finial states is larger than 23 dB. The pumping current of the micro-heater is tuned from 0 mA to 100 mA. As shown in Fig. 3.28(a), the polarization state is switched from the initial state to the perpendicular final state when the electrical pumping current is above 60 mA. The Poincaré sphere diagrams show that the polarization state of the initial state and the final state are almost perpendicular to each other. Fig 3.28(b) shows the dynamic response of the output polarization states under the periodical pumping current. S1, S2 and S3 are vector parameters which represent the polarization state in Poincaré sphere. The dashed line is the electrical pumping current with the periodicity of 125 μs. The polarization vectors are changed according to the pumping current which indicates that the switching time of the polarizer is less than one period (125 μs). However, the switching period chosen in the experiment is limited by the response time of the polarization analyzer. The shorter switching time is not demonstrated in this experiment. According to the experimental results shown in Fig. 3.20, the typical switching time of the MEMS polarizer is around several micro seconds.

3.4 Optical tunneling junction on optical waveguide for reconfigurable WDM system.

In previous sections, the double optical barriers which the input and output light is coupled by prisms are demonstrated as optical switch, VOA and polarizer. The double optical barriers coupling light from free space using prisms have merits such as flexible configuration, fast tuning speed and fabrication convenience. However, there are two drawbacks which limit the double barriers structures form been further integrated into the photonic circuit. One drawback is the device scale is very large (typically 400 μm × 400 μm) which prevent the massive integration of such devices. The device scale is mainly determined by the size of the prisms which are the largest components of the double barrier structures. Although the size of the prisms can be reduces by some smart designs, it cannot be smaller than the spot size of the Gaussian beam from the single mode fiber. The other drawback is that the divergence of the Gaussian beam is very large when propagating a large distance. Although the Gaussian beam can be temporally transformed to approximate plane wave to meet the requirement of the resonance tunneling condition, it will become Gaussian beam again after propagating a short distance from the prisms. The divergence increases the spot size of the Gaussian beam thus increases the loss of the integrated structures. Optical waveguides have been used as components in integrated photonic circuits or as the wave guiding medium in optical communication systems for many years. In this section, an optical tunneling junction and its application on

reconfigurable WDM system are demonstrated by combing the double barriers structures with the optical waveguide.

3.4.1 Design of the optical tunneling junctions

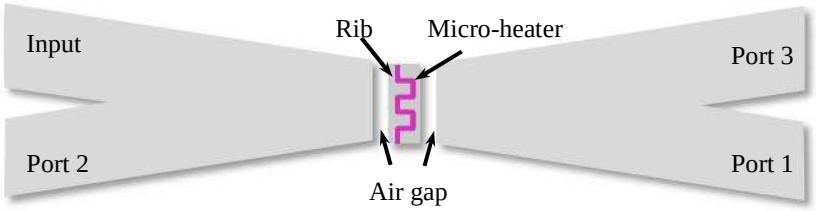

Fig. 3.29: The schematic of optical tunneling junction

The schematic of optical tunneling junction is shown in Fig. 3.29. The optical tunneling junction is based on a cross-shaped waveguide with four ports: one port for input light, port 1 for transmission, port 2 for reflection and port 3 for reference. The central rib is formed by cutting two symmetry gaps at the cross region. A micro-heater is located on the rib region to control the resonance tunneling conditions from input to port 1. The working principle of the optical tunneling junction is similar to the prim coupled double barriers structures discussed in pervious sections. The angle of two crossed waveguide is 36° which is two times of the incident angle of the input light on the interface between the waveguide and the air gap. The optical barriers are formed since the incident angle is 18° which is larger than the critical angle. The transmission between the input and port 1 is depended on the resonance tunneling effect.

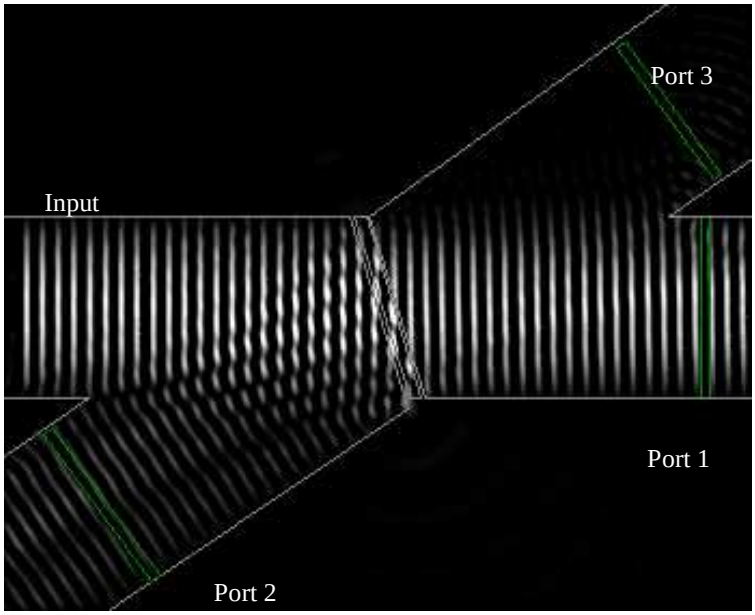

(a)

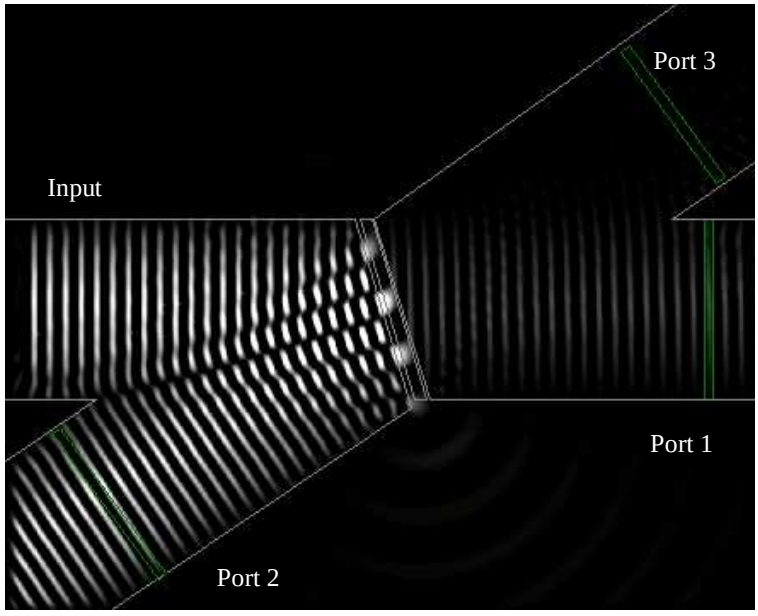

(b)

Fig. 3.30: Electric field distribution of optical tunneling junction when the rib temperature is (a) 293 K and (b) 310 K respectively.

The micro-heater is patterned on the rib structure to control the resonance tunneling condition of the junction via changing the refractive index of the rib. Port 2 is to collect the reflected light which is not satisfied the resonance tunneling condition. Port 3 is kept to monitor the cross talk from the input port. It should be pointed out that, the incident light has to satisfy both the resonance tunneling condition and the waveguide propagating condition to be transmitted from input port to port 1.

The electric field distribution calculated by the finite differential time domain (FDTD) method is shown in Fig. 3.30. The bright parts represent the high electric field concentration and the dark parts represent the low electric field concentration. The air gap is set to be 0.5 μm, the rib width is 1.64 μm and the waveguide width is 9 μm. The input wavelength is chosen to be 1550 nm and the incident angle is 18°. In the initial state (Fig. 3.30(a)), most of the light is transmitted from input to port three since the resonance tunneling condition is satisfied. Here the refractive index of the central rib is set to be 3.420 which is the refractive index value of silicon at room temperature (293 K). Fig. 3.30(b) shows the FDTD simulation results when the rib refractive index changes from 3.420 to 3.423. The refractive index change Δn is 0.003 which can be caused by rising the temperature of silicon by 17 K. According to Fig. 3.30(b), most of the light is reflected back to port 2 as the rib refractive index is changed.

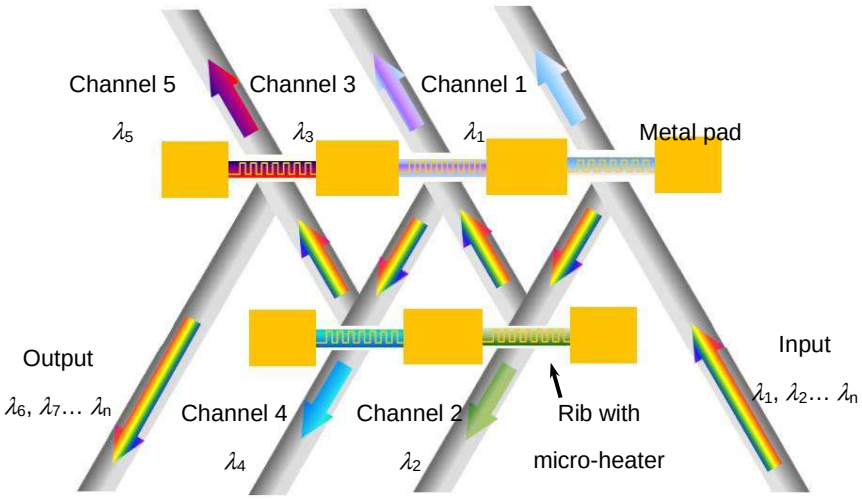

Fig. 3.31: The schematic of the reconfigurable WDM system integrated by optical tunneling junctions

The schematic of reconfigurable wavelength de-multiplexer (WDM) system is shown in Fig. 3.31. The reconfigurable multiplexer consists of one input channel, one output channel and five drop channels which are controlled by the heating current induced by the metal pad. Light can be transmitted from the input channel to the output channel by total internal reflection. Here, the path way from the input channel to the output channel is called the transport waveguide (the waveguide with rainbow arrows). The transport waveguide and the waveguides for the drop channel (channel 1 to 5) are separated by a rib structure. The transport waveguide and the drop channel form a Y-shape optical tunneling junction which allows the light with certain wavelength dropping from the transport waveguide to the drop channel. The dropped wavelength of each junction is controlled by the heat current induced by the micro-heater.

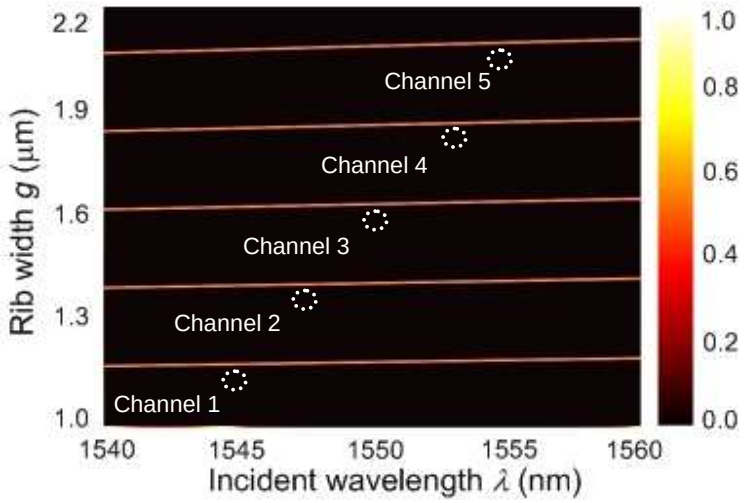

Fig. 3.32: The contour map of the transmission of the tunneling junction at different incident wavelengths and rib widths.

Fig. 3.32 shows the contour map of the tunneling junction transmission at different rib widths and wavelengths. The bright part is the high transmission region which shows the output wavelength is determined by the rib width. The rib width of each channel is varying from 1.2 μm to 2.0 μm so that the output of each channel is different from each other. Other wavelengths which do not satisfy the resonance condition of the tunneling junctions (dark region of Fig. 3.32) remains in the transport waveguide and are transmitted to the output port. Small vibration of rib optical length can be induced by the thermo-optical tuning of the rib refractive index which can finely tune the drop wavelength of each channel. In this way, the drop frequency can cover the frequency span from 1545 nm to 1555 nm.

3.4.2 Experimental results and discussions

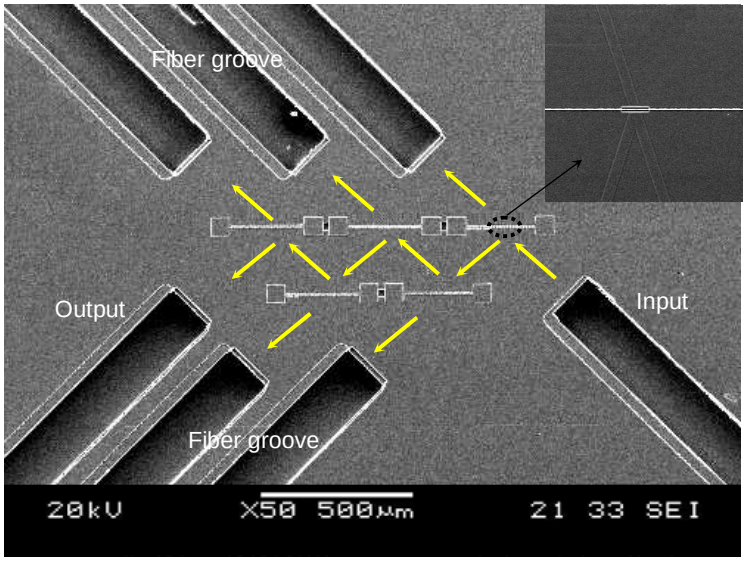

Fig. 3.33: Scanning electron micrograph of the reconfigurable WDM system.

Figure 3.33 shows the scanning electronic micrograph (SEM) of the fabricated MEMS tunable add-drop multiplexer. The inset shows the enlarged picture of the tunneling junction which is connected to the fiber groove by the ribbed waveguide. The tilt angle of the fiber grooves is 45 degree while the incident angle of each tunneling junction is 18° since the fiber grooves and the optical tunneling junctions are connected by curved waveguide. Both the metal pad and rib are coated with aluminum so that the ribbed region can be heated via the pumping current introduced by the micro-needle connected with the aluminum pad. The rib widths of the tunneling junctions vary from 1.15 μm to 1.95 μm which ensure the output wavelength is different at each channels. The tunable add-drop multiplexer is fabricated using silicon-on-insolate wafer with the working depth of 7 μm.

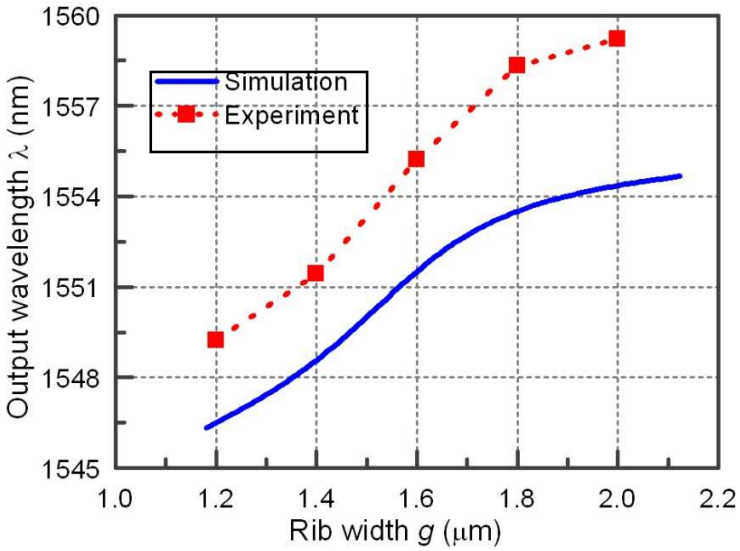

Fig. 3.34: Experiment results of the output wavelength at different rib width.

Fig. 3.34 shows the measured output of each channel. The experiment results show the same tendency as the simulated results. The difference between the measured and the simulated output wavelength is mainly induced by the fabrication imperfect of the rib width. According to the measured output, the fabricated rib width is 100 nm wider than expected which is within the mismatch tolerance of the masks.

3.5 Summary

In this chapter, the double optical barrier structure realized by MEMS technology is demonstrated for different photonic devices. The frustrated total internal reflection (FTIR) optical barrier structure is presented and its transmission states are numerically studied via transfer matrix method. Then three switchable photonic devices is demonstrated using MEMS system. A thermo-optic switching characteristics of an optical double optical barrier structure is demonstrated, which has a high-low-high-low-high

refractive index construct formed by micromachined silicon prisms and air gaps. Analysis shows such structure features full transmission (i.e., ON state) and requires low refractive index change for switching function. The device is fabricated on silicon-on-isolator wafer using deep etching process. In experiment, it measures a switching speed of 1 μs and an extinction ratio of 30 dB. A switchable polarizer is demonstrated using the double optical barrier structure. In experiment it measures a PER of lager than 23 dB when the pumping current is above 60 mA. The switching time is shorter than 125 μs which is limited by the polarization analyzer used in the experiment. A MEMS tunable add-drop multiplexer is finally presented, the output of which can be tuned by thermo-optical effects. The tunable add-drop multiplexer is based on Y-shape optical double barriers tunneling junction which are realized by MEMS technology. In the experiment, a five-channel prototype of the tunable add-drop multiplexer is demonstrated. The measured output is ranged from 1549.24 nm to 1559.21 nm.

CHAPTER 4

TUNABLE SLOW LIGHT METAMATERIALS

This chapter is focused on the tuning of the slow light metamaterials via the refractive index change of the substrate. The tunablility of the tunable metamaterial is limited by the material properties of the substrate, the tuning range of which is normally not very large. The objective of this chapter is to find a new metamaterial structure which can enhance tunability of the tunable metamaterials. Furthermore, the tuning of the group velocity index of such tunable metamaterials is also numerically studied.

4.1 Design of metamaterial slow light waveguide

Light can be slowed within either the homogenous materials or waveguides. For homogenous materials, light is interact with the electron gases of the atoms or molecular which results in the delay of the propagation of the light waves. The slow light factor is equal to the refractive index of the homogenous materials which is typically low in nature material. The slow light waveguides are typically realized by enhanced dispersion caused by the waveguide geometry. The light waves are forced to resonance within the waveguide so that the effective propagation constant can be very large. In this way, the propagation speed of the light can be slowed down in the slow light waveguides.

Similar as the CROW waveguide consists of dielectric optical micro-cavities, the magnetoinductive slow light waveguide is consisted of magnetically coupled metal ring arrays (Fig. 4.1). The magnetoinductive slow light waveguides can be divided into two groups: in-plane coupling waveguides (Fig. 4.1 (a)) and multi-plane coupling waveguides (Fig. 4.1 (b)) based on their geometries. Metamaterial slow light waveguides are constructed with unit cells which are typically metal rings. Constructed by sub-wavelength unit cells, metamaterials can be treated as the homogenous materials the refractive index of which can be very large. Furthermore, the metamaterials can be used as the waveguide the slow light factor of which can be further increased by the resonance between the couplings of the unit cells. Therefore, metamaterials are ideal building blocks for slow light waveguides.

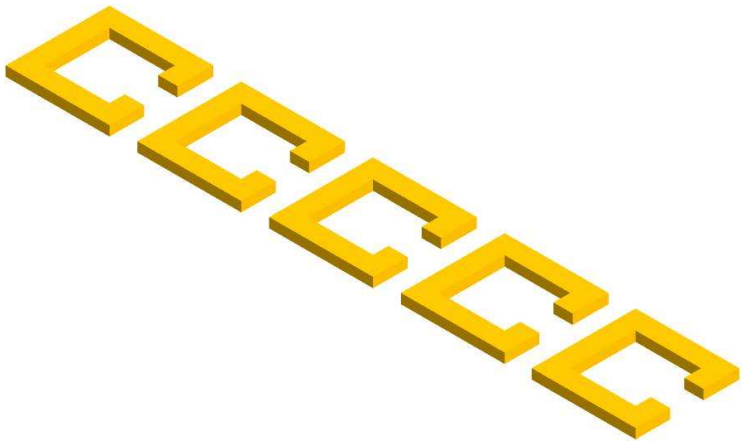

(a)

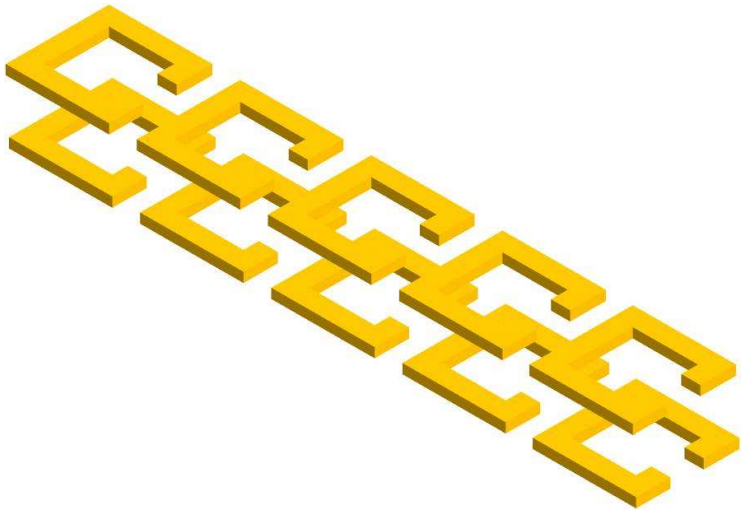

(b)

Fig. 4.1: Schematic of magnetoinductive slow light wave guide. (a) coupling within a single layer (b) coupling between two layers.

The dispersion relation of magnetoinductive waves can be written as

$$j\omega L + \frac{1}{j\omega C} + R + 2j\omega M \cos k\alpha = 0 \tag{4.7}$$

where *L*, *C*, and *R* are the self-inductance, capacitance and resistance of the metal rings respectively. *M* is the mutual inductance between the nearest rings. *k* is the wave number and α is the period of the array.

For multi-layer waveguides, the dispersion relation of magnetoinductive waves can be written as

$$\left(j\omega L + \frac{1}{j\omega C_1} + R_1 + 2j\omega M_1 \cos k\alpha\right) \times$$

$$\left(j\omega L + \frac{1}{j\omega C_2} + R_2 + 2j\omega M_2 \cos k\alpha\right) = -\omega^2 M \tag{4.8}$$

where the top and bottom metal rings are of the same self-inductance. Both the transmission and slow light factor are highly depended on the coupling of the top and bottom metal rings.

The unit cell structure must satisfy the following two conditions to achieve the high tunability of the tunable metamaterial. One of the conditions is to concentrate the electric field within the substrate. The other condition is to find a method the control the surface current of the metal films using the refractive index change of the substrate.

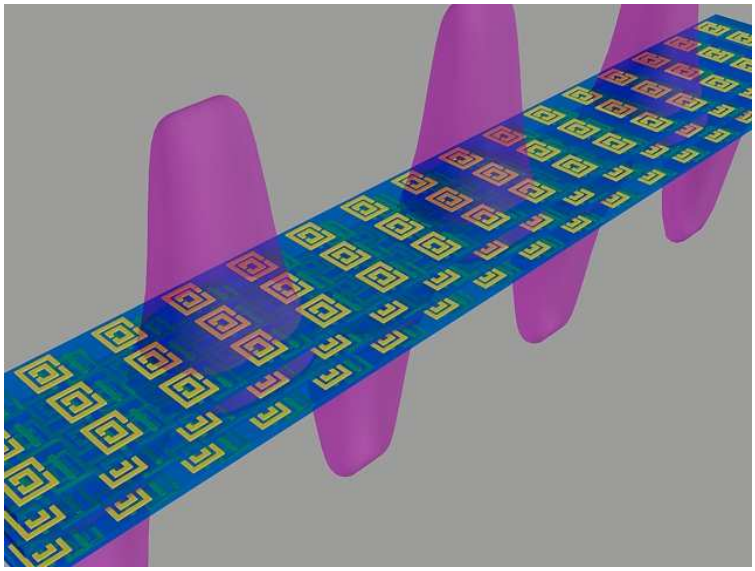

(a)

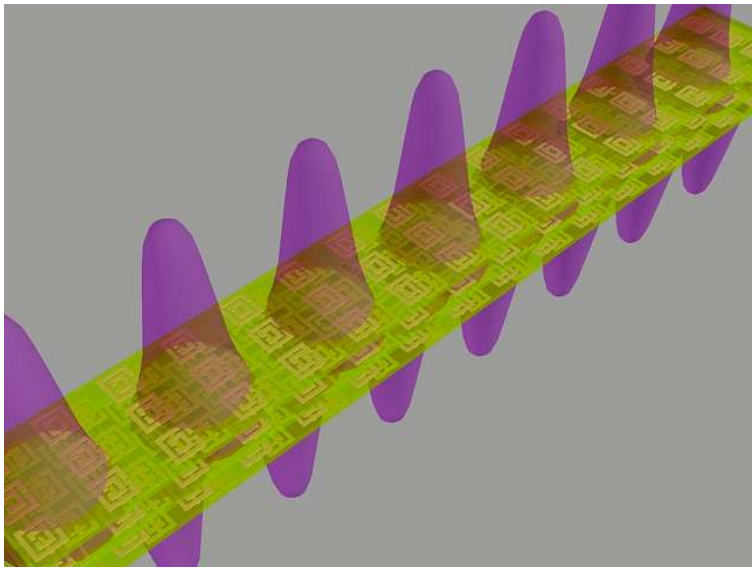

(b)

Fig. 4.2: Schematic of the metamaterial slow light waveguide. (a) and (b) are schematics of the slow light waveguide which shows the light propagating along the waveguide before (a) and after (b) the permittivity of the substrate is changed.

To increase the tunability of the unit cell by changing the substrate permittivity, a coupled SRR structure is designed as the unit cell of the metamaterial waveguide. Fig. 4.2 shows the schematic diagram of the unit cell and its inset shows the side view. The unit cell consists of two identical SRRs, each has an inner ring and an outer ring. Both rings are square and split. The side length of the inner ring is a_i = 150 nm and that of the outer ring is a_o = 270 nm. All the wires has the same width w = 30 nm. The gap of the splitting is G = 30 nm. The two ring resonators are located at the front and back side of the substrate, respectively. The gap of the outer ring overlaps with each other in the magnetic field (H field) direction. In addition, two wires are buried in the central plane of the substrate. In the light propagation direction P_k, the wires are aligned to the central lines of the two resonators, respectively. The lattice constant is 300 nm along the electric field (E field) direction PE and is 600 nm along P_k. The substrate is 60 nm thick and the material is chosen as silicon in the calculation while the metal parts are made of perfect electric conductor (PEC) material. As the electric field is concentrated within the gaps of the outer rings, the coupling of the two SRRs is highly dependent on the spacing between the two gaps. Although the distance between the SRRs (i.e., the thickness of the substrate) cannot be changed easily once they are fabricated, the refractive index (i.e., the permittivity and/or the permeability) between them can be tuned without much difficulty, which is equivalent to a thickness change of the substrate. Therefore, the electric response of the unit cell to the incident terahertz (THz) waves is dependent on the refractive index of the substrate. For the magnetic response of metamaterials, it is actually induced by the surface current of the metal, which is different from the traditional magnetic materials. In the coupled SRRs, the surface current of the two split

rings goes to opposite directions of the overlapped region. The induced electromotive force is dependent on the coupling of the surface currents, which also varies with the permittivity of the substrate. Therefore, both the electric response and the magnetic responses of the unit cell can be tuned by varying the permittivity of the substrate. By using the above unit cell as the building block, the THz slow light waveguide is constructed as shown in Fig. 4.2(a) and Fig. 4.2(b). It consists of infinite layers of unit cells at both E and H directions. When a THz wave is input to the slow light waveguide, its propagation speed would be tunable by varying the permittivity of the substrate since the unit cell has different electric and magnetic responses to such variation.

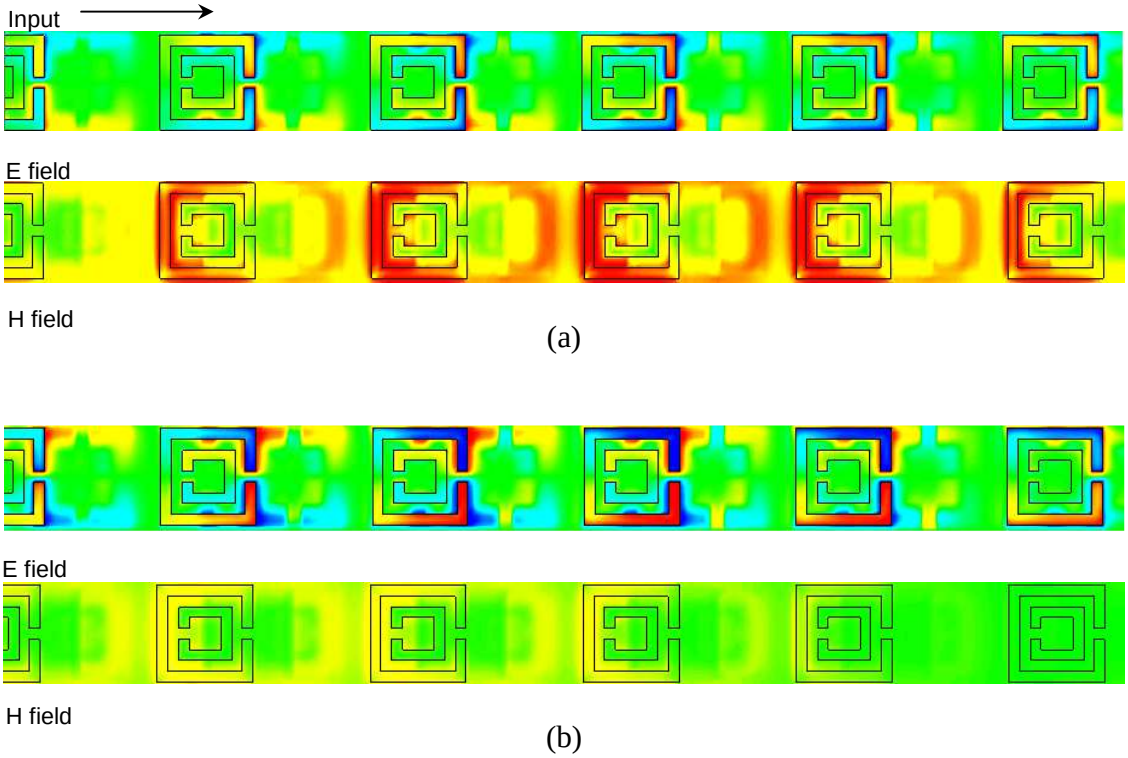

Fig. 4.3: Electric and magnetic field distributions of the slow light waveguide when the substrate permittivity is set to be (a) 12.0 and (b) 12.1 respectively. The incidence

frequency is 43.73 THz. In (a), the electric response is weak but the magnetic response is strong. In (b), they are just opposite.

The characteristics of the slow light waveguide are demonstrated in Fig. 4.3. The light propagation of the THz wave is examined using the Finite-difference time-domain (FDTD) method. The substrate permittivity is set to be 12.000 (Fig. 4.3(a)) and 12.100 THz (Fig. 4.3(b)) respectively. The periodical boundary condition is introduced to mimic the infinite unit cell array. The band width of the waveguide is 0.421 THz. Fig. 4.6 exemplifies the electric and magnetic field distributions of linked unit cells for two cases substrate permittivity □sub = 12.000 and sub = 12.100. The coupling of the two split ring resonators is changed due to the variation of the permittivity of the substrate. As illustrated in Fig. 4.3, the electric field of coupling of the unit cells is enhanced as the substrate permittivity increases. However the magnetic field response to the incidence light becomes weaker as the substrate permittivity changes from 12.000 to 12.100.

4.2 Basic study on fishnet unit cell

The metamaterials can be made tunable by changing the refractive index of their substrate or the surrounding medium. The schematic of the tunable metamaterial via substrate refractive index change is shown in Fig. 4.4.

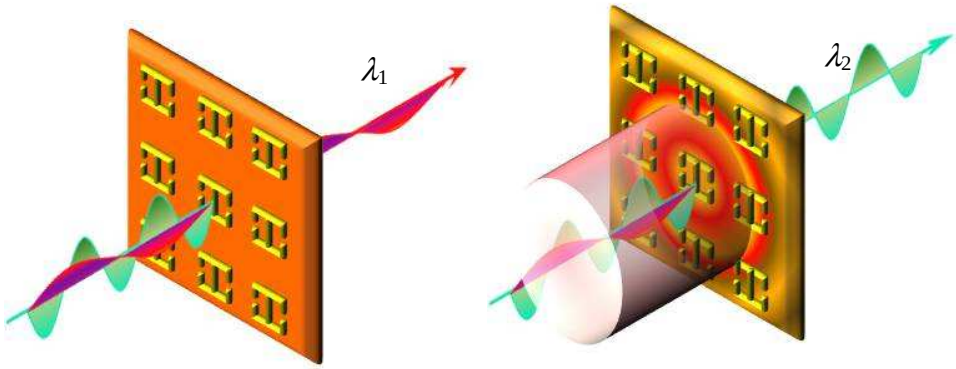

(a) (b)

Fig. 4.4: the schematic of the tunable metamaterial. (a) before the substrate refractive index change the resonance frequency is λ_1. (b) after the substrate refractive index change via the external pumping, the resonance frequency is λ_2.

4.2.1 Design of unit cell

The unit cells of the metamaterials are sub-wavelength optical cavities which control the optical response of the metamaterials by their resonance nature. The metamaterial can be viewed as the continuous materials because the dimension of the unit cells is much smaller than the resonance wavelength. Therefore, the resonance nature of

the metamaterials is one of the most important features which determine the optical properties of the metamaterials. The resonant frequency of the metamaterial unit cells can be changed by the variation of the substrate refractive index which also controls the coupling between the unit cells. The optical response of the metamaterials can be changed by the variation of the substrate refractive index. The schematic of a tunable metamaterials is shown in Fig. 4.4. Metamaterials can be used as wavelength selective devices such as the filter due to their resonance nature. For example, a metamaterial slab allows the incident wavelength $\lambda_{1,}$ which induces strong resonance of the unit cells, to pass through while stop other wavelengths (Fig 4.4(a)). The resonance frequency can be changed by the variation of the refractive index of the substrate. In this way the metamaterial slab can be used as a tunable filter which can be controlled via nonlinear effects such as thermo-optical effects, photon induced free carrier effects and electrical free carrier pumping effects etc.

A fishnet metamaterial is numerically characterized as an example to demonstrate how the effects of the substrate refractive index change of the metamaterials. The unit cell of the finished net metamaterial is shown in Fig. 4.5.

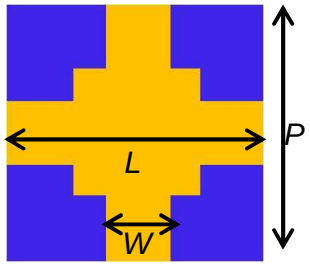

(a)

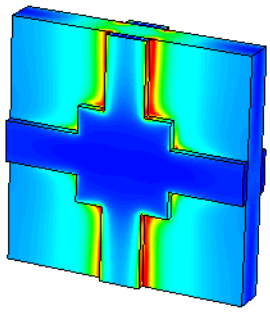

(b)

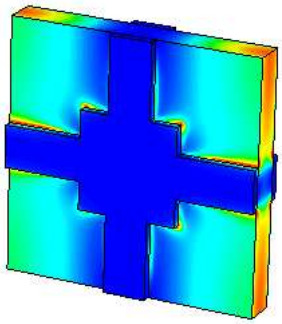

(c)

Fig. 4.5: the 3D contour map showing the (a) electric field and (b) magnetic field distribution of the fishnet unit cell. The side wall length of the central square L = 3.5 μm.

The metal strip width W = 1.5 μm. The period P = 9 μm. The metal thickness t = 0.3 μm and the substrate thickness D = 1.2 μm.

The fishnet unit cell is consisted of three layers, two symmetric metal layers and one substrate. The metal layer has a cross shaped metal strip with the length equal to the period P = 9 mm and a central metal square pad with the side wall length L = 3.5 mm. The metal is chosen to be aluminum during the simulation. The width and the thickness of the aluminum strip is W = 1.5 mm and t = 3 mm respectively. The substrate thickness is D = 1.2 μm.

The EM wave is incident perpendicular to the surface of the fishnet unit cell with the electrical field perpendicular to the aluminum strip. The electric field distribution shows that the energy of the electrical field is focused on the small depth of the aluminum -substrate interface. Some energy, which is concentrated on the corner of the unit cells, manages to penetrate the substrate and resonance between the two metal layers (Fig. 4.5(a)). The distribution of the magnetic field is also mainly concentrated on the surface of the aluminum strip which is perpendicular to the magnetic component of the incident EM wave (Fig. 4.5(b)). The penetrating energy of the magnetic field is focused on the gap between the two aluminum strips which are located on the opposite side of the substrate. The electrical response of the fish net metamaterial can be tuned by changing the refractive index of the substrate which dominate the resonance condition of the penetrating electric field within it. However, the substrate here is chosen to be silicon which does not have directly response to the incoming magnetic field. The tuning of the

substrate refractive index only has minor effect on the metamaterial magnetic response which is caused mainly by changing the surface current of the aluminum strips.

4.2.2 S-parameter analysis

The S-parameter of the fishnet metamaterial (Fig. 4.6) is calculated using the FDTD method which is discussed in §4.1. The boundary condition is chosen to be the unit cell boundary to mimic the real structure with infinite unit cell array. The S_{11} shows the amplitude of the reflection coefficient spectrum which has the resonance frequency of 50.1 THz. The transmission coefficient amplitude spectrum (S_{22}) shows a resonance peak of 48.5 THz which is different from the resonance peak of the reflection. This is due to the absorption in the resonance region which is different from frequency to frequency.

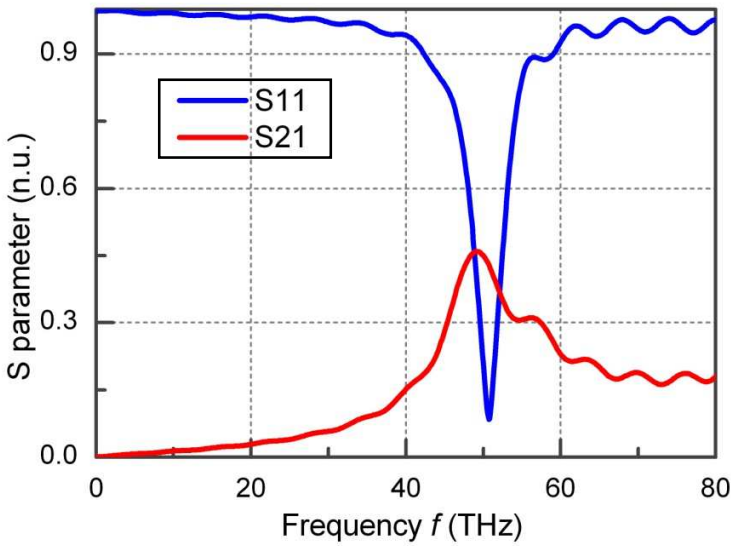

Fig. 4.6: the calculated S-parameter of the fish net metamaterial. S_{11} (the blue line) is the amplitude of the reflection coefficient and S_{21} (red line) shows the transmission coefficient amplitude.

The S-parameter not only can be used to derive the effective refractive index of the fish net metamaterials but also can tell the resonance region of the unit cell. As shown in Fig. 4.6, the resonance peaks for both S11 and S_{21} around 50 THz. Therefore, the following calculation on the effective group index of the fish net metamaterial is ranged from 40 THz to 60 THz to make the spectrum near the resonance more clear.

It has been proposed that electromagnetic metamaterials composite structured materials, formed either from periodic or random arrays of scattering elements should respond to electromagnetic radiation as continuous materials, at least in the long wavelength limit. In recent experiments and simulations, it has been demonstrated that certain metamaterial configurations exhibit scattering behavior consistent with the assumption of approximate frequency dependent forms for ε and μ. However, the techniques applied in those studies probed the materials indirectly, and did not provide an explicit measurement that would assign values for ε and μ.

The S-parameter retrieval method utilizes the transmission and reflection coefficients (S parameters) which can be calculated for a wave normally incident on a finite slab of metamaterial. The scattering data is inverted to determine refractive index *n* and impedance *z*, for systems of several thicknesses, from which we obtain self-consistent values for ε and μ. The technique is applicable to the experimental characterization of metamaterial samples whenever the scattering parameters are known.

The common method of characterizing the electromagnetic scattering properties of a homogeneous material is to identify its z and n. While it is possible to completely specify the scattering in terms of z and n, it is often more convenient to choose a second set of analytic variables that carry a direct material interpretation. These variables are the electric permittivity $\varepsilon = n/z$, and the magnetic permeability $\mu = nz$. Both n and z, and therefore ε and μ, are frequency dependent complex functions that satisfy certain requirements based on causality. For passive materials, Re(z) and Im(n) must be greater than zero. At a given frequency, any material that supports only one propagating mode will generally exhibit a well-defined refractive index n, whether the material is continuous or not. Photonic bandgap materials, for example, are characterized by dispersion curves from which an effective index can be extracted, even for bands well above the first bandgap, and well-defined refraction phenomena can result. However, it is generally not possible to assign an impedance z to a noncontinuous material, except in those cases where the wavelength in the material is much larger than the dimensions and spacing of the constituent scattering elements that compose the medium. If z depends strongly on the surface termination, or if z depends on the overall size of the sample, then z is ambiguous, and it is not possible to assign intrinsic values for ε and μ.

The transmission coefficient for EM wave which incident normally to the face of a one-dimensional (1D) slab of continuous material in vacuum with length d is related to n and z which can be expressed as

$$t^{-1} = [\cos(nkd) - \frac{i}{2}\left(z + \frac{1}{z}\right)\sin(nkd)]e^{ikd} \tag{4.1}$$

where k = ϖ/c is the wavenumber of the incident wave. The incident wave is assumed to travel rightward along the positive *x* axis, with the origin defined as the first face of the material seen by the radiation. To improve the clarity of the subsequent formulas, we introduce the normalized transmission coefficient $t' = \exp(ikd)t$. The reflection coefficient is also related to *z* and *n* which can be expressed as

$$\frac{r}{t'} = -\frac{1}{2}i\left(z - \frac{1}{z}\right)\sin(nkd). \tag{4.2}$$

Equations (4.1) and (4.2) can be inverted to find *n* and *z* as functions of t' and *r*. Performing this inversion leads to the following expressions

$$\cos(nkd) = \frac{1}{2t'}[1 - (r^2 - t'^2)]$$

$$= Re\left(\frac{1}{t'}\right) - \frac{1}{2|t|^2}(A_1 r + A_2 t') \tag{4.3}$$

and

$$z = \pm\sqrt{\frac{(1+r)^2 - t'^2}{(1-r)^2 - t'^2}} \tag{4.4}$$

where $A_1 = r^*t' + t'^*r$ and A2 = 1-$|r|^2$-$|t'|^2$ are both real valued functions that go to zero in the absence of material losses. Note that while the expressions for n and z are relatively uncomplicated, they are complex functions with multiple branches, the interpretation of which can lead to ambiguities in determining the final expressions for ε and μ. We can resolve these ambiguities by making use of additional knowledge about the material. For example, if the material is passive, the requirement that Re(z) > 0 fixes the choice of sign in Eq. (4.4). when Im(n) > 0 leads to an unambiguous result for Im(n) can be expressed as

$$Im(n) = \pm Im\left(\frac{cos^{-1}\left(\frac{1}{2t'}\left[1-\left(r^2-t'^2\right)\right]\right)}{kd}\right) \tag{4.5}$$

When solving the right-hand side of Eq. (4.5), whichever of the two roots yields a positive solution for Im(n). Re(n). The branches of the arccosine function is complicated

$$Re(n) = \pm Re\left(\frac{cos^{-1}\left(\frac{1}{2t'}\left[1-\left(r^2-t'^2\right)\right]\right)}{kd}\right) + \frac{2\pi m}{kd} \tag{4.6}$$

where m is an integer. When d is large, these branches can lie arbitrarily close to one another, making the selection of the correct branch difficult in the case of dispersive materials. For this reason best results are obtained for the smallest possible thickness of sample, as has commonly been known in the analysis of continuous materials. Even with a small sample, more than one thickness must be measured to identify the correct

branches of the solution which yields consistently the same values for n. Note that the requirement that Im(n) > 0 uniquely identifies the sign of Re(n), which is essential when the material may potentially have regions which are left-handed, that is, materials in which Re(n) may be negative.

Fig. 4.7 shows the calculated effective group index $N_g = V_g/c$ where V_g is the group velocity of the EM wave within the fish net metamaterial. The blue line shows the effective group index when the substrate permittivity is 11.9. The red line shows the effective group index when the substrate permittivity is increased to 12. It can be seen from Fig. 4.7 that the range of the effective group index is from 1.7 to 5.6 which means the variation of the light speed within the tunable fish net metamaterial is varying from c/1.7 to c/5.6.

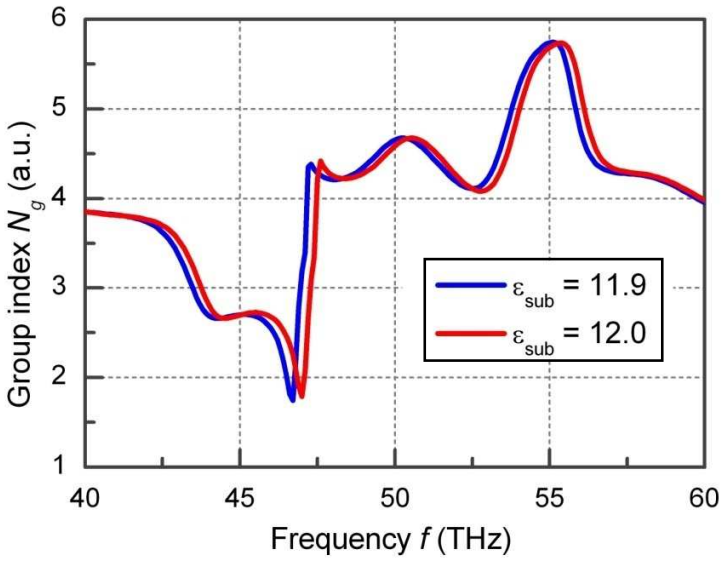

Fig. 4.7: the calculated group index Ng versus the frequency at different substrate refractive index. The blue and red lines represent the group index when the substrate permittivity is 11.9 and 12.0 respectively.

It should be point out that the highest frequency shift occurs at frequency of 47.1 THz which has the transmission less than 10%. However the effective group index change near the transmission peak 48.5 THz is only around 0.1. The tunability of the fishnet structure is quite limited. There are two methods to increasing the tunability of the tunable metamaterial. One is to change the substrate material to have a higher refractive index tuning range. The other way is to design a new unit cell to have better sensitivity to the substrate refractive index change.

4.3 Design of coupled SRR unit cell structures

As discussed in pervious section, it is possible to increase the tenability of the tunable metamaterial by changing the geometry of the metamaterial unit cell. In this section, a new metamaterial unit cell structure is proposed which has much larger tunability than the fish net unit cell metamaterial.

4.3.1 Inner and outer ring design

Fig. 4.8 shows the schematic diagram of the unit cell and its inset shows the side view. The unit cell consists of two identical SRRs, each has an inner ring and an outer ring. Both rings are square and split.

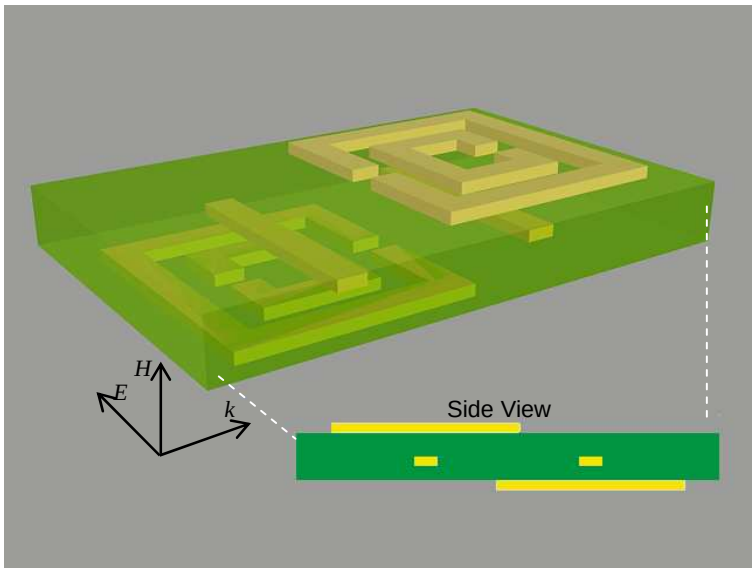

Fig. 4.8: The schematic of coupled split ring unit cell.

The coupled SRR unit cell is designed to increase both the electrical and the magnetic response of the tunable metamaterial on the variation of the substrate refractive

index. Two aluminum SRR unit cells are separated from each other by the substrate. Therefore, the surface current induced by the incident EM wave is coupled through the overlap region of the SRR unit cells. In this way, the magnetic response can more or less controlled by the substrate refractive index change. Two aluminum metal bars are buried within the substrate. The electric field is concentrated within the substrate since the metal strips are designed to response mainly the incoming electrical field. In this way, the sensitivities of both the electrical and the magnetic response of the tunable metamaterial are increased. There are four major parameters which control the resonance condition of the coupled SRR unit cell. They are the gap width of the spitted ring, the length and width of the buried metal bars and the thickness of the substrate. In this section, the geometry parameters of the coupled SRR unit cell is numerically characterized and discussed.

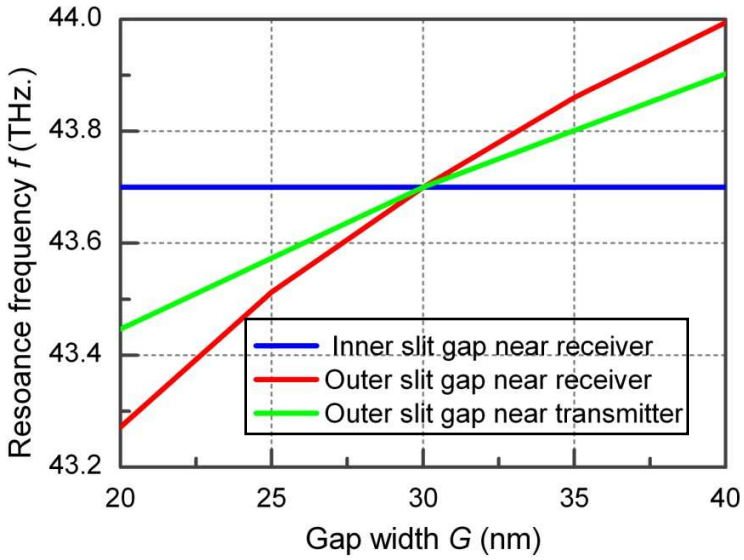

Fig. 4.9: The resonance frequency change versus the gap width. The blue, red and green lines show the change of the gap width at different positions.

The effects on the resonance frequency versus the gap width at different gaps are shown in Fig. 4.10. The blue line shows the gap width change of the inner gap on the top of the substrate (Fig. 4.8). The red line and blue line shows the outer gap change above and below the substrate respectively. The inner ring doesn't change much of the resonance frequency. However the both of the outer gap width can shift the resonance frequency around 0.8 THz when the gap width is changed from 20 nm to 40 nm. It can be seen from Fig. 4.10 that the outer ring has larger effects on resonance frequency than the inner ring. This is because that the outer ring determines the coupling between the SRR within the coupled SRR unit cell which is very important to the resonance frequency of the coupled SRR unit cells.

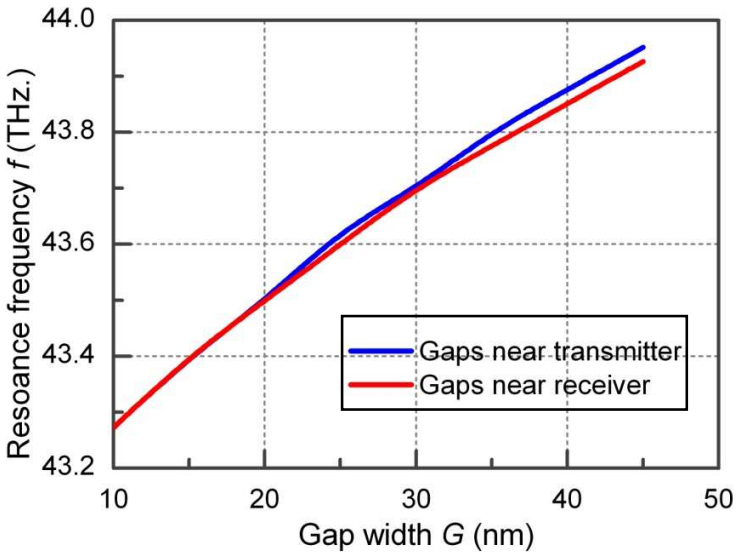

Fig. 4.10: The resonance frequency change versus the gap width. The blue and red line shows the gaps change of the lower split ring and upper split ring.

The effects on the resonance frequency versus the gap width of upper (red line) and lower (blue line) SRR unit cell is shown in Fig. 4.11. The upper SRR gaps and lower

SRR gaps change has the similar effect on the resonance frequency change that is from 43.28 THz to 43.94 THz. The tuning range of the gap width is from 10 nm to 45 nm. The resonance frequency shift is mainly caused by the asymmetry introduced by changing the gap widths of only one split ring which explains the reason that the gap change of the upper SRR unit cell and the lower one has the approximately the same effect on the resonance frequency shift.

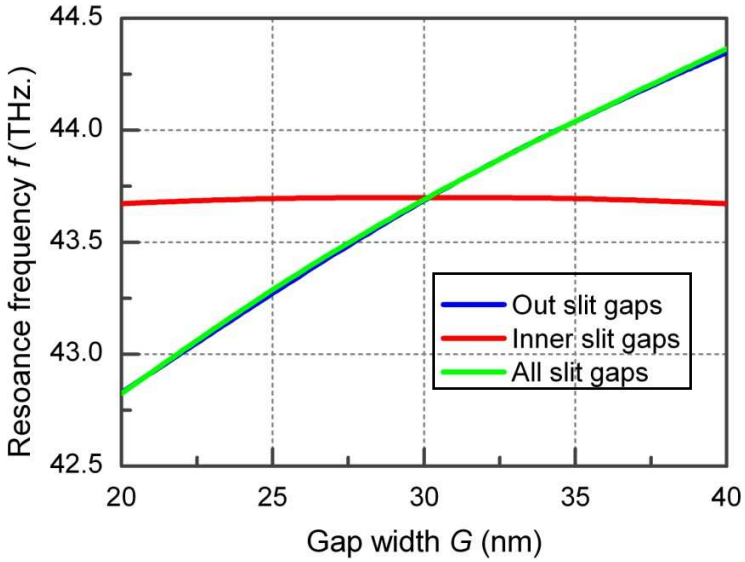

Fig. 4.11: The resonance frequency change versus the gap width. The blue and red line shows the gaps change of inner and outer gaps width respectively and the green line shows the effects when all the gap widths are changed.

The resonance frequency versus the gap width is shown in Fig. 4.12. The tuning range of the gap width is 20 nm (from 20 nm to 40 nm). The blue and green line shows the tuning of the outer gaps and all the gaps respectively. The red line shows the tuning of the inner gap only. It can be seen from the simulation results that tuning all the gaps has the same affects on the resonance frequency shift as the tuning of the outer gaps only.

Moreover, the tuning of the inner gaps has little affects on the resonance frequency. Therefore, it can be concluded that the resonance frequency is highly dependent on the outer gap which control the coupling of the SRRs within the unit cell. Tuning the refractive index of the substrate is equal to the tuning of the effective optical length between the two outer gaps which is one of the key parameters of the couple SRR unit cell.

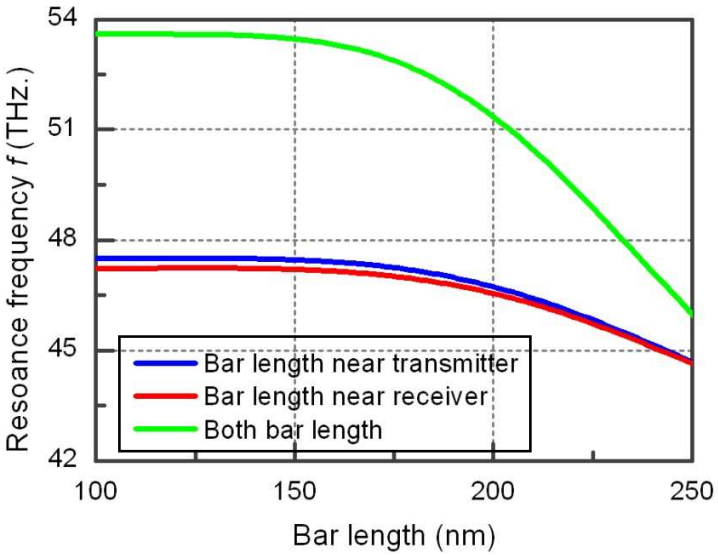

Fig. 4.12: The resonance frequency change versus the buried aluminum bar length. The blue and red line shows the bar length change of the split ring unit cell near and far from the incident EM wave respectively and the green line shows all the bar length changed simultaneously.

The buried bar is designed to response the electrical field of the incoming EM waves. The bars are surrounded by the substrate and thus sensitive to its refractive index change. Fig. 4.13 shows the tuning of the bar length separately (red and blue line) and

simultaneously (green line). Similar to the gap tuning, changing the length of one bar only introduce the asymmetry to the coupled SRR ring unit cell. Therefore, it does not matter which of the bar length is changed. However, changing both of the bars within one coupled SRR unit cell has great effect on the electrical resonance of the unit cell. Thus cause the resonance frequency shifts from 42.9 THz to 53.7 THz.

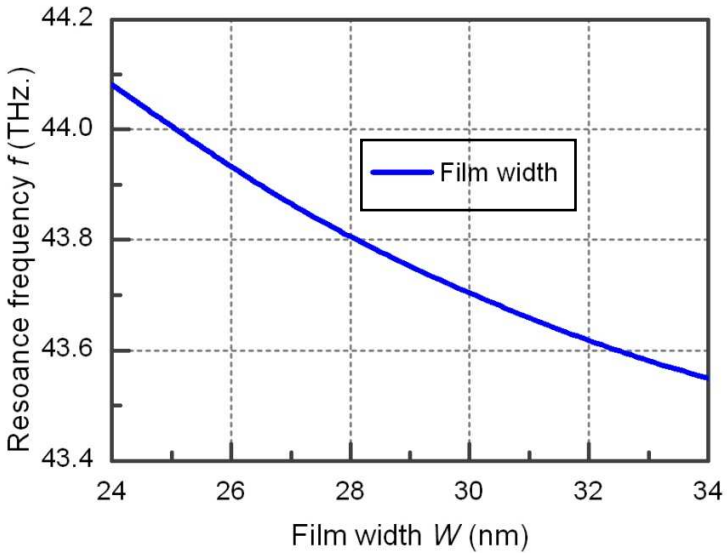

Fig. 4.13: The resonance frequency change versus the film width.

The film width of the split ring is tuned to illustrate its affect on the resonance frequency of the coupled SRR unit cell. The change of the film width affects the capacitance between the gaps. Thus it has similar effect on the gap width tuning of the SRR unit cells. The capacitance between the gaps is proportionally to the film width and inversely proportional to the gap width. Therefore, the gap width and the film width has the opposite effects on the resonance frequency shift. When the film width is changing from 20 nm to 35 nm, the resonance frequency shift is from 43.48 THz to 44.09 THz

which is similar to that of the gap width change.

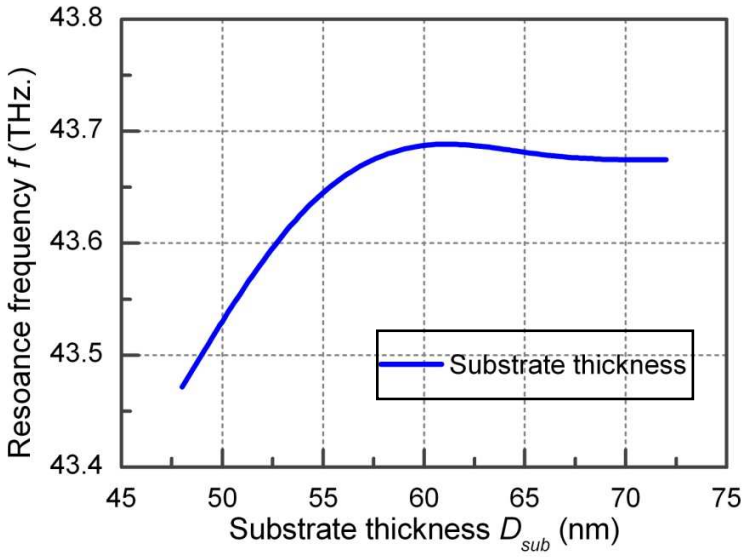

Fig. 4.14: The resonance frequency change versus the substrate thickness.

The resonance frequency versus the substrate thickness is shown in Fig. 4.15. The change of the substrate thickness actually changes the coupling between the upper and lower SRR unit cells. The thicker the substrate is the weaker the coupling between the SRR unit cells is. Therefore, changing the substrate thickness has much larger effect on the resonance frequency change (from 43.57 THz to 43.7 THz) when it is less than 60 nm. When the thickness of the substrate is thicker than 60 m, further change of the substrate depth has little effect on the resonance frequency shift.

The electrical response of the coupled SRR unit cell is determined by the buried aluminum bars and the magnetic response is determined by the coupling of the two SRR resonators. According to Fig. 4.13 and Fig. 4.15, tuning of the substrate refractive index has greater impact on the electric response of the coupled SRR. However, the electric and magnetic response can be tuned separately via changing the buried bar length and

substrate respectively.

4.3.2 S-parameter analysis

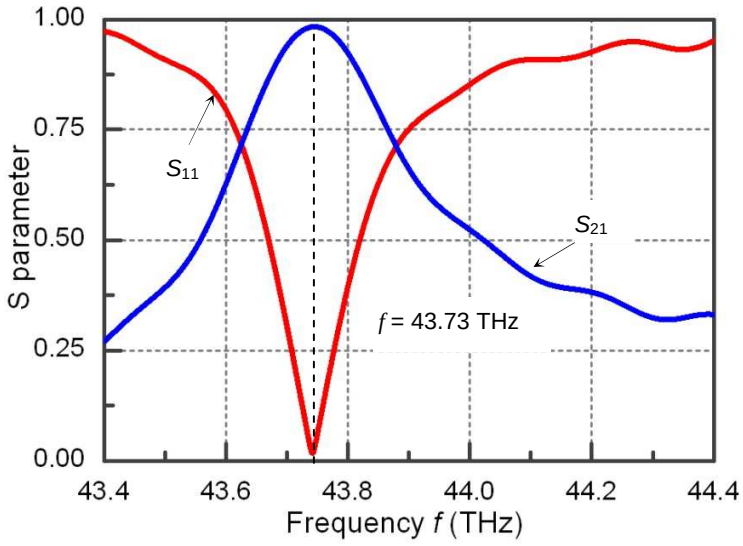

(a)

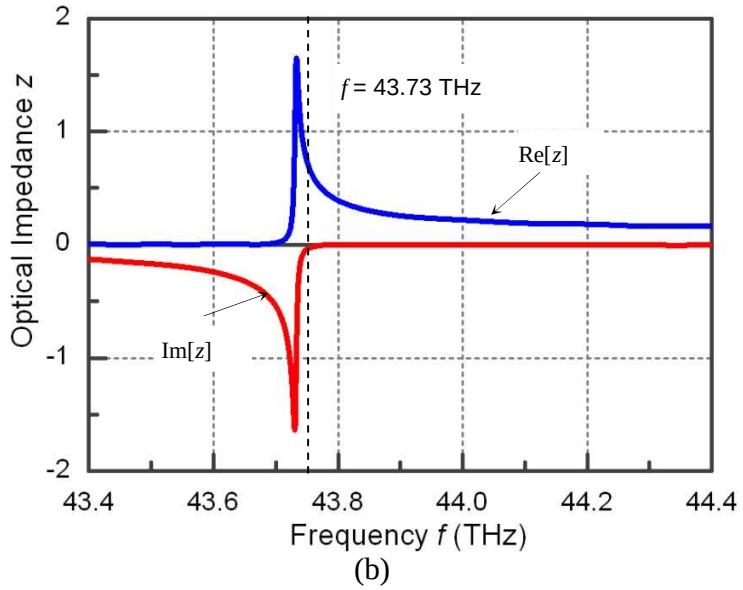

(b)

Fig. 4.15: (a) S-parameters of the unit cells as the function of incident frequency, (b) optical impedance of the unit cell of the metamaterial slow light waveguide (ε_{sub} = 12). The blue line shows the real part of the impedance and red line shows the imaginary part

of the impedance.

Since the optical properties of the metamaterials come from its unit cells, it is essential to characterize the unit cell in the THz region before investigating the light propagation of the metamaterial waveguide. The *S* parameter of the unit cell is plotted in Fig. 4.15(a) with the ε_{sub} = 12.00. The S parameters are square root of the transmission and reflection coefficient. S_{21} shows the forward transmission of the couple split ring unit cells which is determined by both the resonance condition and coupling conditions of each unit cells. The resonance condition is satisfied at 43.73 THz, at which S_{21} is close to 100%. The Q factor of the unit cell is approximately 100. For comparison, the reflection coefficient S_{11} is also plotted in Fig. 2(a). At 43.73 THz, it has minimum reflection. The optical impedance *z* (Fig. 4.15(b)) can be deduced by the *S* parameter retrieval method. Since the group index n_g can be written as $n_g = n + \omega dn/d\omega$, it is important to choose the working frequency at which n_g is highly frequency dependent. Such choice is favorable for tuning the speed of light by varying the incident frequency or for obtaining different slowing effect at different incident frequencies. The impedance matching condition ($z \approx 1$ in Fig. 4.15(b)) is also satisfied near 43.73 THz.

The working frequency of the slow light unit cell is chosen to be 43.73 THz due to the following two reasons. The first reason is that the working frequency has to be located at high dispersion region for large slow light factors. The dispersion of this frequency (43.73 THz) is since it is located on the resonance peak shown in Fig. 4.15(a). The other reason is that the frequency should have relatively low loss. It can be seen in

Fig. 4.15(b), the loss of the chosen frequency is out of the high absorption region where the imagery part of the impendence is larger.

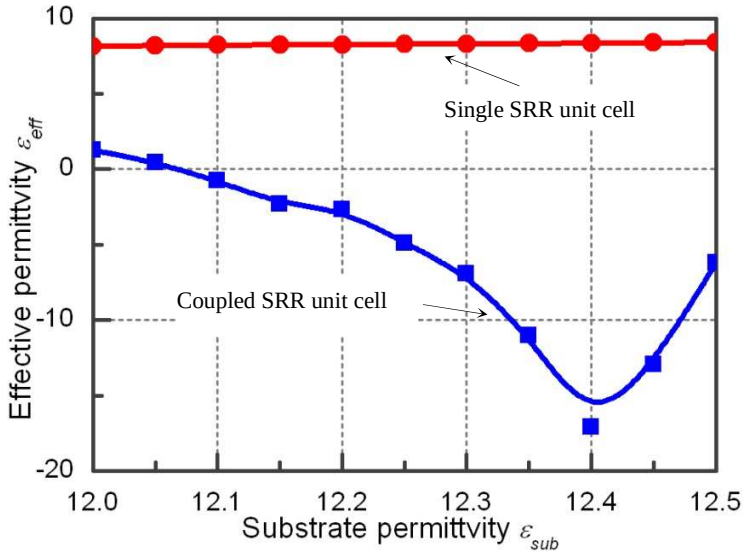

(a)

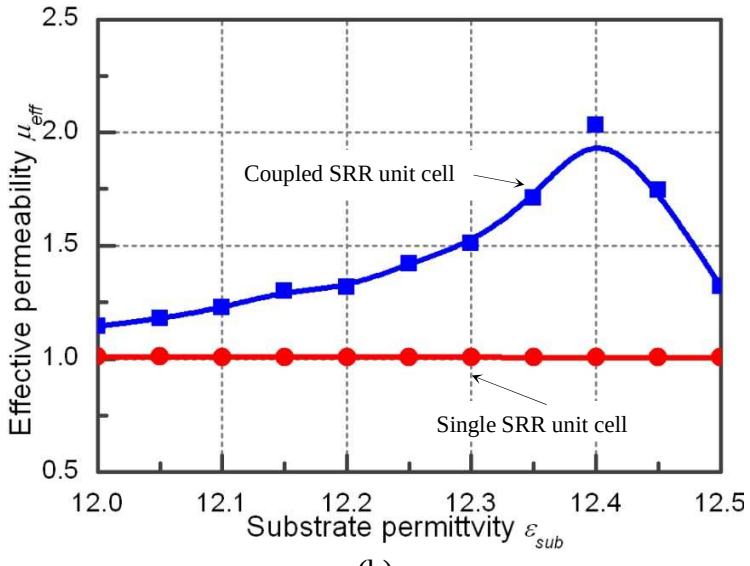

(b)

Fig. 4.16: (a) The effective permittivity ε_{eff} and (b) the effective permeability μ_{eff} versus the substrate permittivity ε_{sub} for both the coupled SRR lattice and the single SRR lattice. The frequency of incident light is 38.65 THz which is the resonant frequency of the

single SRR unit cell. The change of the substrate permittivity $\Delta\varepsilon_{sub}$ is 0.5. The ε_{eff} of coupled SRR lattice and the single SRR lattice have the tuning range of 18.42 and 0.25 respectively. The μ_{eff} of coupled SRR lattice and the single SRR lattice have the tuning range of 0.8874 and 0.038 respectively.

The effective permittivity ε_{eff} and effective permeability μ_{eff} of the coupled SRR lattice and single SRR lattice are simulated to illustrate the improvement of tunability of the coupled SRR unit cells (Fig. 4.16). The parameters of both coupled and single SRR unit cells are identical to those in Fig. 1. The period boundary condition is applied to both *H* and *E* direction while the open boundary condition is applied to the *k* direction. Generally speaking, the sensitivity to the substrate permittivity becomes higher when the incident frequency approaches the resonance frequency. Therefore the frequency of the incident light is chosen to be 38.65 THz which is the resonant frequency of the single SRR unit cell. As shown in Fig. 4.16(a), the effective permittivity ε_{eff} of the coupled SRR lattice is tuned from -17.068 to 1.350 while the effective permittivity ε_{eff} of the single SRR lattice is tuned from 8.135 to 8.387. The tuning range of the ε_{eff} for the coupled SRR lattice is more than 70 times larger than the single SRR lattice. The tuning range of μ_{eff} for coupled SRR lattice and the single SRR lattice is 0.887 (from 1.145 to 2.032) and 0.004 (from 1.006 to 1.010) respectively (Fig. 4.16(b)) which shows the tuning range of the μ_{eff} for coupled SRR lattice is 200 times larger than the single SRR lattice.

4.4 Tuning of the group velocity

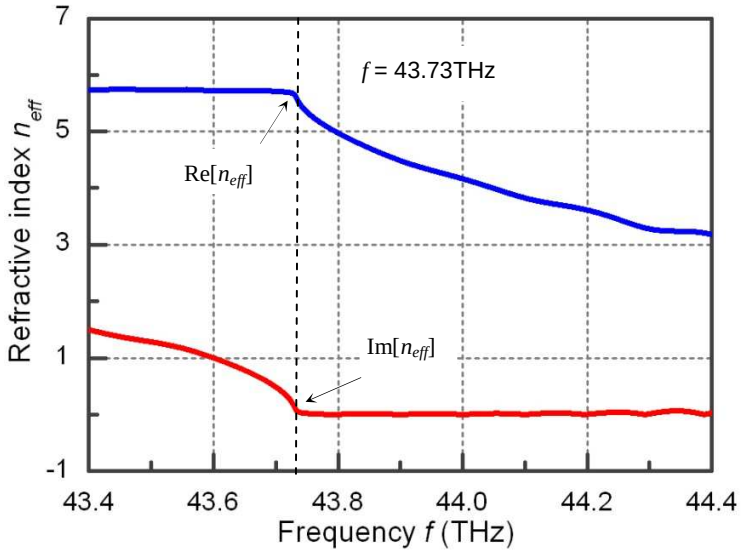

(a)

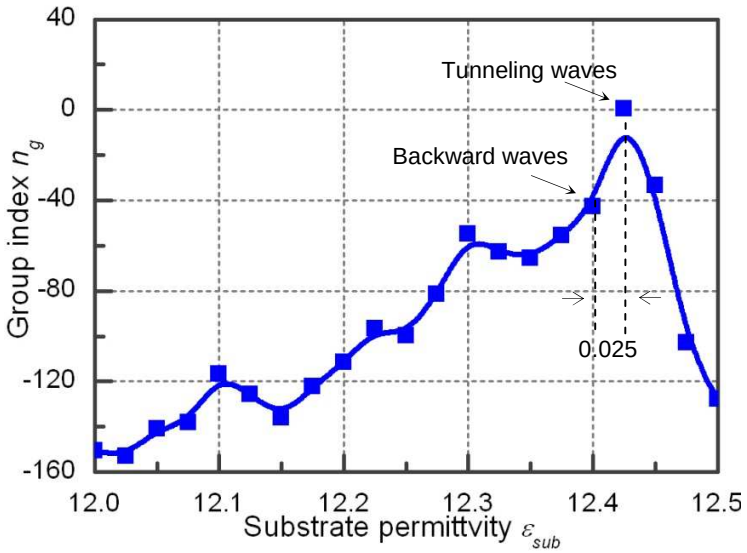

(b)

Fig. 4.17: The group index as a function of the substrate permittivity. The incidence frequency is 43.73 THz. The propagated light is tuned from a slowed backward wave to a

tunneling wave in response to a change of substrate permittivity by 0.025.

The effective refractive index n_{eff} (Fig. 4.17 (a)) and the optical impedance z (Fig. 4.16(b)) can be deduced by the S parameter retrieval method. Since the group index n_g can be written as $n_g = n + \omega dn/d\omega$, it is important to choose the working frequency at which n_g is highly frequency dependent. According to Fig. 4.17 (a), $dn/d\omega$ is large near 43.73 THz and the imagery part of the effective refractive index Im[n_{eff}] approaches zero which indicates low absorption. The impedance matching condition ($z \approx 1$ in 4.13(b)) is also satisfied near 43.73 THz.

The group index shows directly the slowing effect when the light propagates along the metamaterial slow light waveguide. As discussed above, the group index is highly dependent on two parameters, the substrate permittivity and the light frequency. Fig. 4.17(b) plots the relationship between the group index and the substrate permittivity. At the resonance frequency 43.73 THz, the group index is highly sensitive to the substrate permittivity especially when $\varepsilon_{sub} = 12.425$. In the observation window of ε_{sub} = 12.000 to 12.500, n_g first increases gradually to its maximum and then decreases sharply. Sharp slope occurs over the range ε_{sub} = 12.400 to 12.425 (i.e., 0.2% change). For large tunability, such range is selected as the targeted working range. Correspondingly, the group index is tuned from -42.79 to 0.19. Therefore, the propagation light is tuned from slowed backward wave ($n_{\text{g}} < 0$) to tunneling wave ($n_{\text{g}} \approx 0$) by a variation of 0.2% of the substrate permittivity. Therefore, the propagation speed of the light in the metamaterial slow light waveguide can be tuned by finely adjusting the substrate permittivity.

4.5 Discussion on absorption

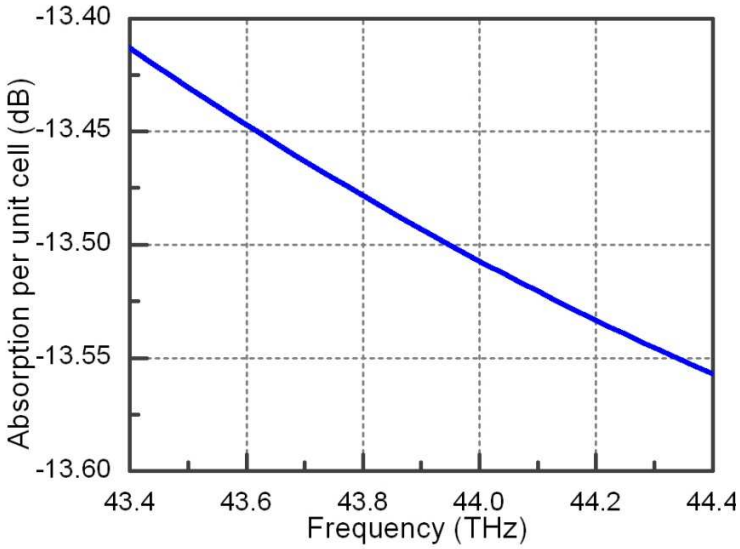

(a)

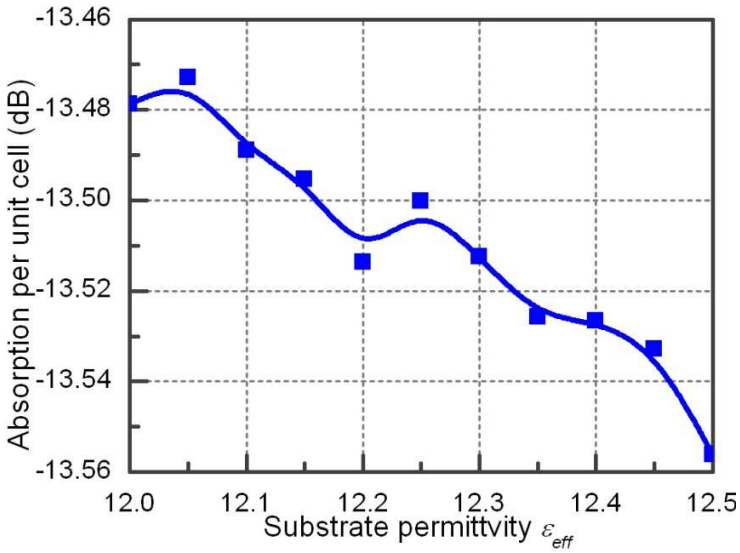

(b)

Fig. 4.18: The absorption per unit cell (a) at different incident frequencies (b) at different substrate permittivity.

The absorptions as functions of the incident light frequency and the substrate permittivity as plotted in Fig. 4.18(a) and Fig. 4.18(b), respectively. The typical loss per unit cell is -13.5 dB. The fluctuation of the absorption due to the incident frequency (Fig. 4.18(a)) and the substrate permittivity (Fig. 4.18(a)) is less than 1.5%, which will not cause severe dispersion problem. Although the absorption of this waveguide is very large from the engineering point of view, the coupled SRR structure is proven to be useful as the building block of the tunable slow light waveguide.

4.6 Summary

In summary, tunable slow light metamaterial via tuning the substrate refractive index is numerically studied. Firstly, the numerical study on a fish net unit cell shows the possible method to improve the tunability of the tunable metamaterial is to concentrate the electric field on the substrate and control the surface current. Base on this method, a couple SRR unit cell is finally proposed and numerically characterized. The simulation results show that the coupled SRR design improves the tunability of the effective permittivity and the effective permeability by 70 and 200 times, respectively The required permittivity change is only 0.025, which can be achieved by either thermal-optic effect or photon induced free carrier effect of the semiconductor materials. By use of the tunable metamaterial, this slow light overcomes the problems associated with the conventional micro-cavities approaches such as the rapid drop of transmission at a fixed working frequency in the process of the light speed tuning. Therefore, it may find

potential applications in data storage, photonic circuits, optical communications and bio-sensors.

CHAPTER 5

TUNABLE METAMATERIAL VIA MEMS TECHNOLOGY

Metamaterial can be designed to have very sensitive response to the external excitation, such as heating, carrier injection and photoelectric effect. However, the excitation of the metamaterial depends on the change of the refractive index of the compositing materials of the metamaterial unit cell which is the same as the modulation of the dielectric optical resonators (chapter 3). The metamaterial unit cells are sub-wavelength resonators which can be used to enhance the light-material interaction as the dielectric optical resonators do. Previous researches show that the ultra-high Q optical resonators can be used for fast optical modulation such as, switching, signal generation or even slowing the light. Although most of the nature materials are too stable to have the refractive index change larger than 5%, high Q optical resonators can enhance the excitation of the nature materials thus make the fast optical modulation feasible. Practically speaking, metamaterials cannot have a very high Q resonance because the absorption of the metal part limits the photon lifetime within the unit cells. Therefore, metamaterials need a new tuning method to further increase the tunablility.

The objective of this chapter is to show a new way to tune the optical properties of the metamaterials. This tuning method combines micromachined technology with the design of the metamaterial unit cells. It can make the metamaterials tunable without exciting their compositing materials. Therefore, the tunablility of the metamaterial is no

longer limited by the refractive index change of the nature materials. In this chapter, a split ring structure is selected to demonstrate the tuning method. The electrical and magnetic response of the tunable metamaterial is demonstrated both numerically and experimentally. This chapter is organized as follows: 5.1 shows the design of the tunable metamaterials. 5.2 and 5.3 shows the electrical and magnetical response of the structure. 5.4 shows the experimental results of the light speed modulation of the tunable metamaterials and 5.5 give the conclusion.

5.1 Design of the tunable metamaterials

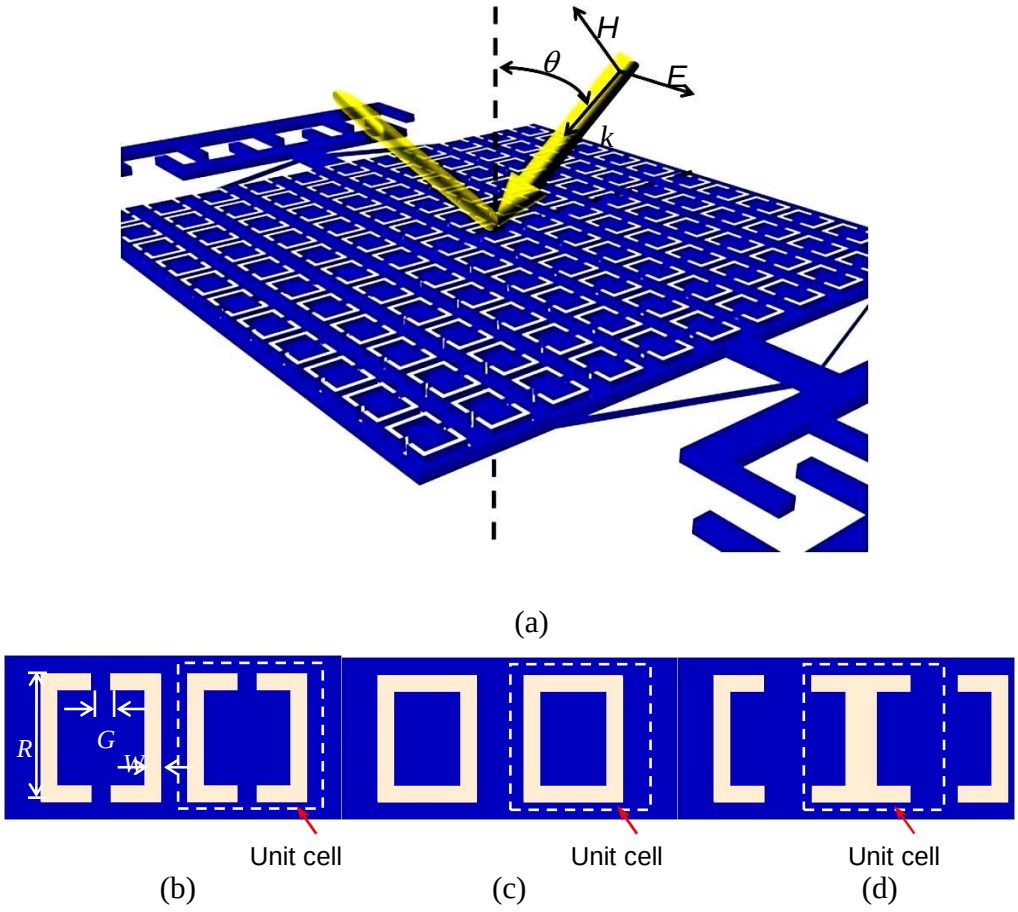

Fig. 5.1 Schematic of the tunable metamaterials using MEMS technology. (a) the top view of the tunable metamaterials. The frame part is connected with the comb drive which is used to tune the gap of within the unit cells. (b) The unit cell consists of two semi-square split rings separated by a small gap *G*. One is movable while the other is fixed. In the initial state the unit cell is in the "[ ]" shape. The unit cell can be changed to (c) the shape "□" and (d) the shape "I" by simply translating all the movable rings at the same time. *W* is the width of the metal strip and *R* is the side length of the split ring.

Although the changes of the surrounding media or the composting materials have certain effect on the metamaterials, the optical property of metamaterials is mainly determined by the geometries of its unit cells other than the composting materials. Therefore, the metamaterials can be tuned by changing the geometry of its unit cells other than exciting its compositing materials.

Fig. 5.1 shows the generic architecture of the tunable metamaterials using MEMS technology. The unit cell of the tunable metamaterials is chosen to be the split ring resonator which consists of two split semi-squares. *R* is the side length of the unit cells and *W* is the width of the metal stripe. One of the semi-squares is connected with the MEMS comb drive [7-10] which can be moved by the static electric forces. The other semi-square is fixed on the substrate. Therefore, each split ring resonator unit cell consists of one movable semi-square and one fixed semi-square, the gap between which can be tuned by the MEMS comb drive. In the initial state the gaps between each semi-square are set to be identical for the fabrication convenience. The moving direction of the comb drives are controlled by the external pumping voltage. Therefore, the gap *G* between the two semi-squares within one unit cell (Fig. 5.1 (b)) can be reduced or increased which depends on the moving direction of the comb drive. Fig. 5.1 (c) shows the geometry of the unit cell become shape "□" when the gap between the two semi-squares are reduced to minimum. And Fig. 5.1 (d) shows the geometry of the unit cell becomes shape "I" when the gap between the two semi-squares is increased to maximum. In this way, the geometry of the unit cells can be changed simultaneously by the MEMS comb drive.

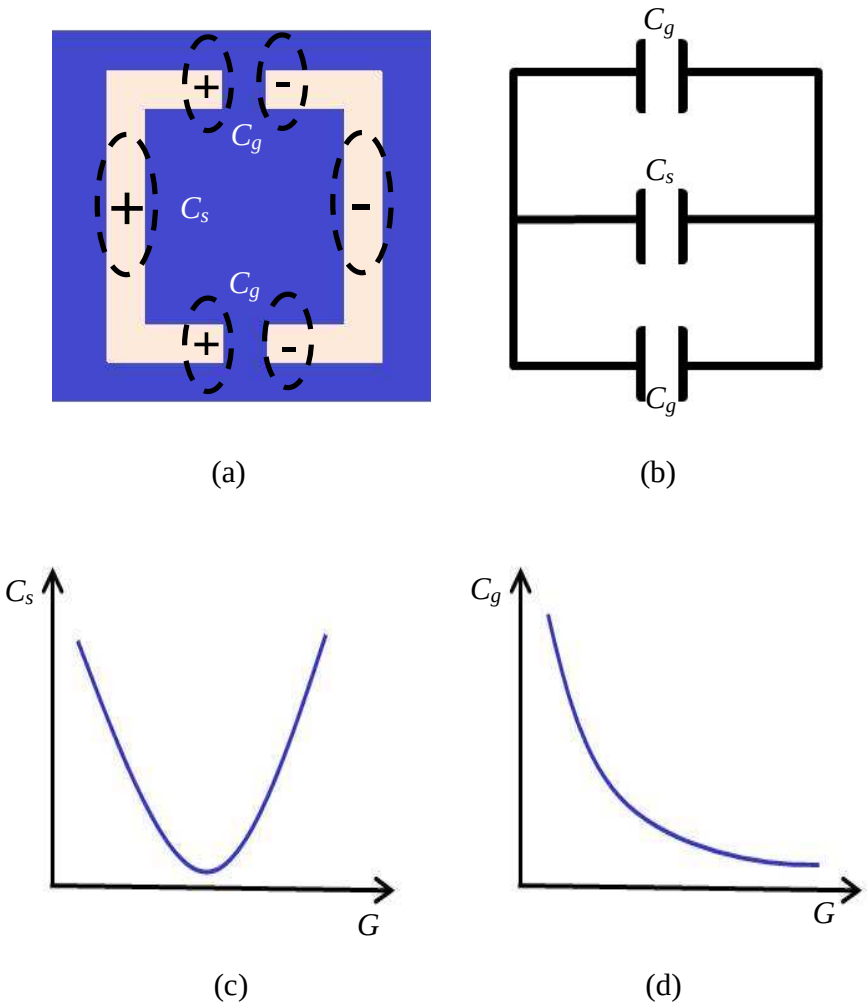

Fig. 5.2: Equivalent circuit analysis of the tunable metamaterial unit cell. (a) shows the schematic of the unit cell. The "+" and "-" stand for the accumulation of the electrons induced by the external electric field. (b) the equivalent circuit of the unit cell (a). (c) and (d) show the capacitance change during the gap increasing.

The tuning effect of the gap can be analyzed by the equivalent circuit which is shown in Fig. 5.2 (b). There are two kinds of the capacitors within one unit cell. One is the capacitors formed by the gaps between the two semi-squares Cg and the other one is

the capacitors formed by the adjacent side wall of the unit cell Cs (Fig. 5.2 (a)). Cg and Cs has different dependence as the gap G change. The capacitance C is inversely proportional to the distance d between the two metal slips which form the capacitor. (5.1) Therefore, Cg is always decreasing as the gap G is increasing (Fig. 5.2 (d)). Cs shows the same trend as the G increasing. However, as the G is further increasing, the Cs becomes lager and lager as the capacitance formed between the adjacent unit cell side walls becomes dominate (Fig. 5.2 (c)). As shown in Fig. 5.2 (b), the total capacitance of the equivalent circuit is given by,

$$C_{total} = \frac{C_g{}^2 C_s}{2C_s C_g + C_s{}^2}$$

When the gap is very small C_g is much larger than C_s,

$$C_{total} = \frac{C_g}{2} \tag{5.2}$$

As the gap is increasing, C_g become smaller and smaller and C_s become dominant,

$$C_{total} = C_s \tag{5.3}$$

If the two semi-square are connect to each other (Fig. 5.1 (b) and (c)), the gap between the two metal slips vanished and the total capacitance becomes zero.

The total capacitance is controlled by the gap *G* of the two semi-squares. The electrical response of the unit cell can be tuned by changing the *G* because the total capacitance dominant the resonance induced by the external electrical field. Moreover the gap *G* also affects the surface current induced by the external magnetic field. Therefore,

both the electrical and magnetic response of the unit cell can be tuned by changing the gap distance *G* of the unit cell. In this way, the optical response of the metamaterial can be tuned without changing the refractive index of any compositing materials.

5.2 Numerical results and discussions

5.2.1 Numerical analysis of the electrical response

The side wall length of the split ring resonator affects both the capacitance between the two semi-squares C_s and the instinct resonance frequency of the split ring resonator. Fig. 5.5 shows the FDTD simulation results of the split ring resonator metamaterial with different side wall length (R = 35 μm, R 30 μm and R = 25 μm). The period and gap is fixed at P = 40 μm and G = 5 μm respectively. The resonances, which become higher when R is decreasing, appear to be a sharp dip as shown in the transmission spectrum. The dip frequency varies from 2.3 THz to 3.09 THz which shows 34% frequency change as the R changes from 35 μm to 25 μm.

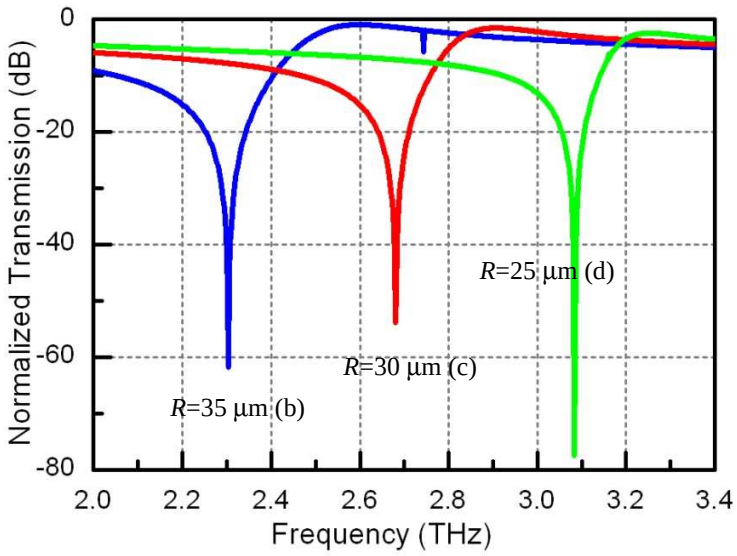

(a)

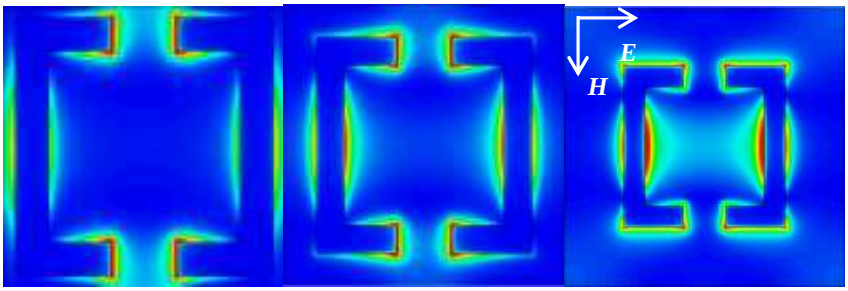

(b) (c) (d)

Fig. 5.3: Numerical analysis on the side wall length effect of the split ring metamaterial. (a) the transmission spectrum. The electric field distribution shows when (b) R = 35 μm, (c) R = 30 μm and (d) R = 25 μm respectively.

The dip frequency change is caused by two reasons. One is the instinct resonance frequency of the split ring resonator is increase since the split ring resonator becomes smaller as the R is decreasing. The other reason is that the capacitance between the semi-squares of the adjacent unit cells is changed. The capacitance $C \propto L/d$, where L is the

length of the metal slit which equal to the *R* here and *d* is the distance between the two metal slit. The change of the *R* does not affect the capacitance between the two semi-squares, since both *L* and *d* equal to R here. However, the capacitance between the two semi-squares which belong to the different unit cells decreases when *R* is decreasing (Fig 5.3(b), 5.3(c) and 5.3(d)). That is because that both *L* and *d* are inversely proportional to *R*. Therefore, the total capacitance of the unit cell decreases as *R* is decreasing. As the resonance frequency$\omega = \sqrt{LC}$, the decreasing of the capacitance actually shifts the dip frequency to the lower frequency which is the opposite to the effect of the instinct resonance frequency change. The instinct frequency of the split ring resonator unit cell dominates the dip frequency which is shown in Fig. 5.5(a). The dip frequency shifts to higher frequency region as *R* is decreasing.

The period of the tunable metamaterial can change the coupling strength of the semi-squares between the adjacent unit cells which is similar to the effect of the side wall length of the split ring resonator unit cell. However, the change of the period does not affect the instinct resonance of the split ring resonator because the geometry of the resonator does not change.

The simulation results of different period are shown in Fig 5.6. Here, the side wall length and the gap width is fixed at *R* = 22 μm and *G* = 5 μm. The transmission spectrum shown in Fig. 5.4(a) is similar to the transmission spectrum shown in Fig. 5.3(a). The resonance dip shifts to higher frequency region as the period is decreasing. Fig. 5.3(b), Fig. 5.3(c) and Fig. 5.3(d) show the electric field distribution of the unit cells at different period. Here, the side wall length is identical in Fig. 5.3(b), Fig. 5.3(c) and Fig. 5.3(d). It

looks different because the simulation region is chosen to be one unit cell and the period of the unit cells are different in Fig. 5.3(b), Fig. 5.3(c) and Fig. 5.3(d).

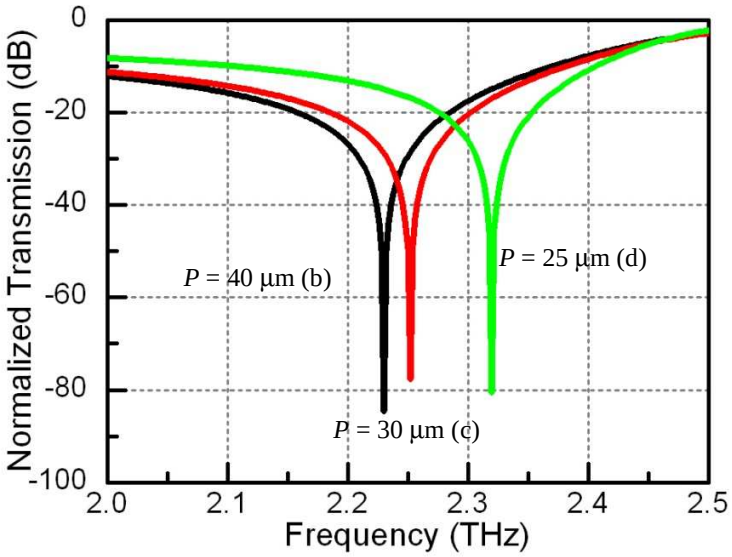

(a)

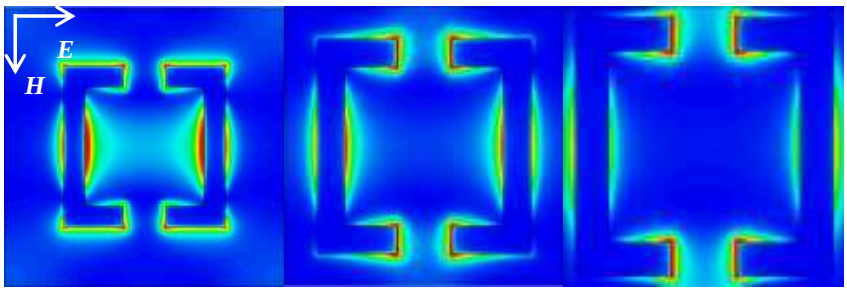

(b) (c) (d)

Fig. 5.4: Numerical analysis on the different period of the split ring metamaterial. (a) the transmission spectrum. The electric field distribution shows when (b) P = 40 μm, (c) P = 30 μm and (d) P = 25 μm respectively.

The change of the period affects the capacitance between the semi-squares which belong to the adjacent split ring unit cells. The capacitance of the semi-squares become

smaller as the period is increasing. That is because the distance between the two metal slits becomes lager when the period is increasing. That explains why the frequency shifts to the higher region when the period is decreasing. The dip frequency is changed from 2.23 THz to 2.32 THz which is much smaller than change the side wall length *R* of the unit cells. This is because that the changes of the period only affect the coupling between the adjacent unit cells and leave the geometry of the unit cells unchanged.

The gap width *G* determines the gap capacitance C_g, the side wall capacitance C_s and the instinct frequency of the split ring resonator unit cells. C_g is the capacitance formed by the gap between the two semi-squares within the split ring resonator unit cell (Fig. 5.2(a)). The length of the metal slit for C_g is fixed during the change of the gap width *G*. However, the distance between the two metal silts is proportional to the gap width *G*. Therefore, C_g becomes smaller as *G* is increasing (Fig. 5.2(d)). C_s is the capacitance formed by the side wall of the two adjacent semi-squares. When *G* is very small, the two semi-squares within one split ring resonator unit cell are close to each other. The coupling between those two semi-squares dominates the C_s. The distance between the two semi-squares becomes larger as *G* is increasing. Therefore, C_s is inversely proportional to *G* when *G* is very small. However, the coupling of the semi-squares becomes weaker as *G* is further increasing. The coupling between the semi-squares from the adjacent unit cells become lager and lager and finally dominate the side wall capacitance C_s. Then, C_s becomes larger when *G* is further increasing (Fig. 5.2(c)). It can be seen from Fig. 5.1(d), the shape of the unit cell can be totally changed by the gap distance *G*. Generally speaking the instinct frequency of the split ring resonator is

inversely proportional to the size of the unit cell. The effective size of the unit cell becomes larger when *G* is increasing. Therefore, the instinct frequency of the split ring resonator is inversely proportional to the gap width *G*.

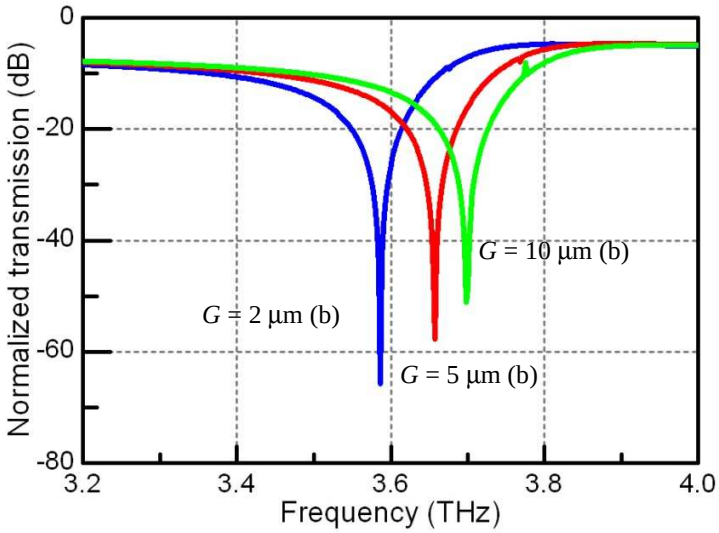

(a)

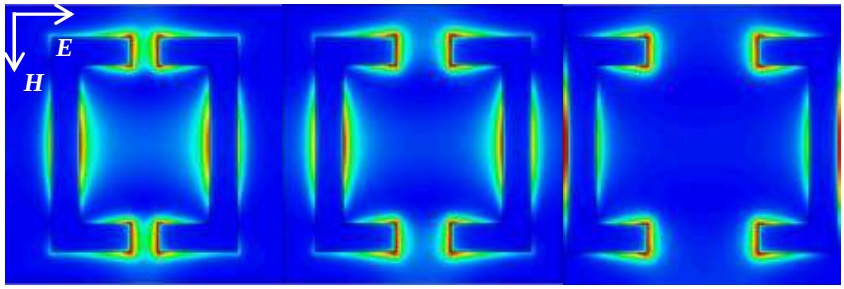

(b) (c) (d)

Fig. 5.5: Numerical analysis on the different gap width *G* of the split ring metamaterial. (a) the transmission spectrum. The electric field distribution shows when (b) *G* = 2 μm, (c) *G* = 5 μm and (d) *G* = 10 μm respectively.

Fig. 5.5 shows the simulation results of the split ring resonator metamaterial at different gap width *G*. The dip frequency shifts to the higher frequency region as shown in Fig. 5.5(a). As discussed before, the increasing of the gap width *G* decreases the gap capacitance and the instinct frequency which results in the decreasing of the dip frequency. The dip frequency can only be increased by the side wall capacitance *C*s which agrees the simulation results in Fig. 5.5(a). Therefore, the effects of the side wall capacitance change dominate in this case.

5.2.2 magnetic response

The compositing material of the tunable metamaterial is aluminum and silicon which are not ferromagnetic materials. Therefore, the magnetic response of the metamaterial is solely depended on the structure of the metal parts. In the previous section, the incident EM wave is perpendicular to the surface of the split ring unit cell. The external magnetic field is within the plane of the split ring resonator the surface current of which cannot be induced by the external magnetic field. In this section, the incident EM wave is tilted so that the magnetic field has perpendicular component to the surface of the split ring resonator. According to the Gauss's Law, the perpendicular component of the magnetic field can induce the surface current within the split ring resonator which in turn generates the induced magnetic field. In this way, the split ring resonator unit cells can response to the magnetic field of incident EM wave.

The following discussion will be focused on the different incidence conditions, such as the incident angle, the polarization state and the incident frequency etc. and their effects on the magnetic resonance of the unit cells. The incident angle determines the strength of the perpendicular component of the incident magnetic field. The larger the incident angle is the stronger the induced magnetic resonance will be. The frequency of the incident EM waves determines whether the induced magnetic resonance can be enhanced or suppressed by the split ring resonator. The induced magnetic field tends to cancel that of the magnetic field from the incident EM waves which means a stronger magnetic resonance results in larger negative response of the tunable metamaterials.

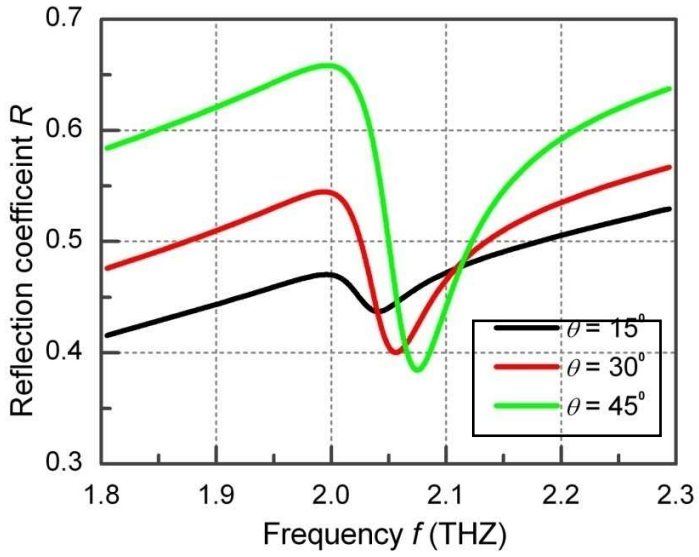

(a)

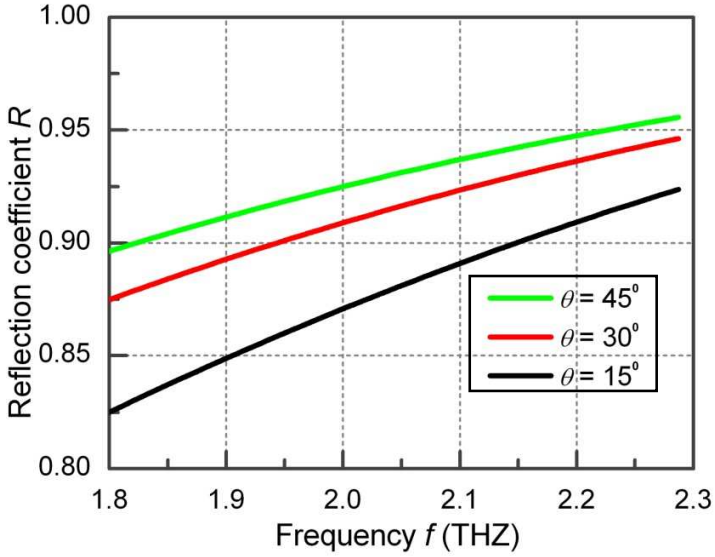

(b)

Fig. 5.6: The simulated reflection spectrum of the tunable metamaterial at different incident angles. (a) with and (b) without perpendicular magnetic field component to the surface of the unit cell.

The reflection spectrums of the tunable metamaterial at different incident angles are shown in Fig. 5.6. The black, red and green lines stand for the incident angles of 15°, 30° and 45° respectively. Fig. 5.6(a) shows the simulation results of the reflection spectrum of the tunable magnetic field when the incident EM wave (TE polarized) have the perpendicular magnetic field component to the split ring resonator (See inserts for details). The reflection spectrum shows a dip at resonance frequency (near 2.05 THz). The change of the incident angle causes a very small resonance frequency variation Δf = 0.05 THz around 2.5% of the resonance frequency. However, the frequency becomes much deeper when the incident angle is increasing. The frequency dip when the incident angle is 45° is around 0.25 which is more than five times larger than that of the 15° incident angle. The variation of the reflection spectrum at different incident angle is caused solely by the orientation of the incident magnetic field because the change of the incident angle does not affect the incident electric field. The perpendicular component of the magnetic field is proportional to the incident angle. Therefore, the resonance dip becomes deeper as the incident angle is increasing. Fig. 5.6(b) shows the simulation results when the incident light is TM polarized. The resonance dip caused by the magnetic field is vanished because the incident magnetic field is always within the surface plane of the unit cell. The change of the incident angle does not have much effect on the reflection spectrum as the electric resonance region is not within this simulation region.

5.3 Fabrication process

The tunable metamaterials are fabricated using the process which is similar to those of the MEMS photonic devices. The fabrication process including dry photolithography, wet etching, sputtering deposition, low pressure chemical vapor deposition (LPCVD) and wet releasing. Of all the technology used for the fabrication of MEMS devices, such as bulk micromachining, surface micromachining and reactive ion etching (RIE), the RIE technology is the most practical one for the manufactory of tunable metamaterials due to the its merits such as high selectivity, anisotropy, arbitrary structure profiles and easy for integration.

Over the last past ten years, the deep reactive ion etching (DRIE) process has been developed into a full-fledged technology which is used in the fabrication of micro-scaled devices such as MEMS devices and Dynamic random access memory (DRAM) memory circuits. The micro-scaled silicon structures can have a very high aspect ratio which is more than 50:1 using the DRIE process. It provides a method for etching silicon at high rate with excellent anisotropy. The silicon etch rate is higher than 20 μm/min for a typical DRIE process. The DRIE process is very useful for the fabrication of the tunable metamaterials which consists of a large number of identical unit cells because each unit cell requires the same fabrication condition.

The tunable metamaterials is fabricated by deep reactive iron etching process (DRIE) using the Surface Technology Systems (STS) inductively coupled plasma (ICP) deep etching systems. The whole fabrication process can be divided into four major steps.

First, the aluminum thin film of 0.5 μm is deposited on the surface of 8 inch silicon on insulator (SOI) wafer. The photo resist (PR) is patterned on the aluminum thin film according to the design of the design of the metamaterial unit cell and electrodes of the comb drive. The extra part of the aluminum film is removed by the lam etch. Then, the hard mask is patterned to etch the structure of the comb drive and supporting frame of the metamaterial unit cells. The DRIE etch is applied through the device layer while the microstructures patterned on the hard mask oxide layer protected by the patterned PR layer. To prevent the notching occurs at the bottom of the wide trenches, PECVD dioxide is then employed to cover the top surfaces, bottoms and sidewalls of the etching trenches. The notching effect is carefully minimized for the coupling of the adjacent semi-squares of the unit cell. The next step is to free the movable structures using wet release with buffered oxide etchant (BOE). This is another critical step for the whole fabrication process. The release time has to be precisely controlled so that the comb drive and movable frame can be released before the anchor parts become movable too. In this project, the typical release time is around 15 minutes. However, it depends on the design of the metamaterial unit cell and release condition such as the density of the BOE. The last step is to make sure the two semi-squares can become conductive when the gap width reaches its maximum or minimum. The unit cells are covered by the shadow mask for aluminum deposition along their side walls. The coated metal can bridge the gap between the semi-squares when they are moved close enough by the comb drives.

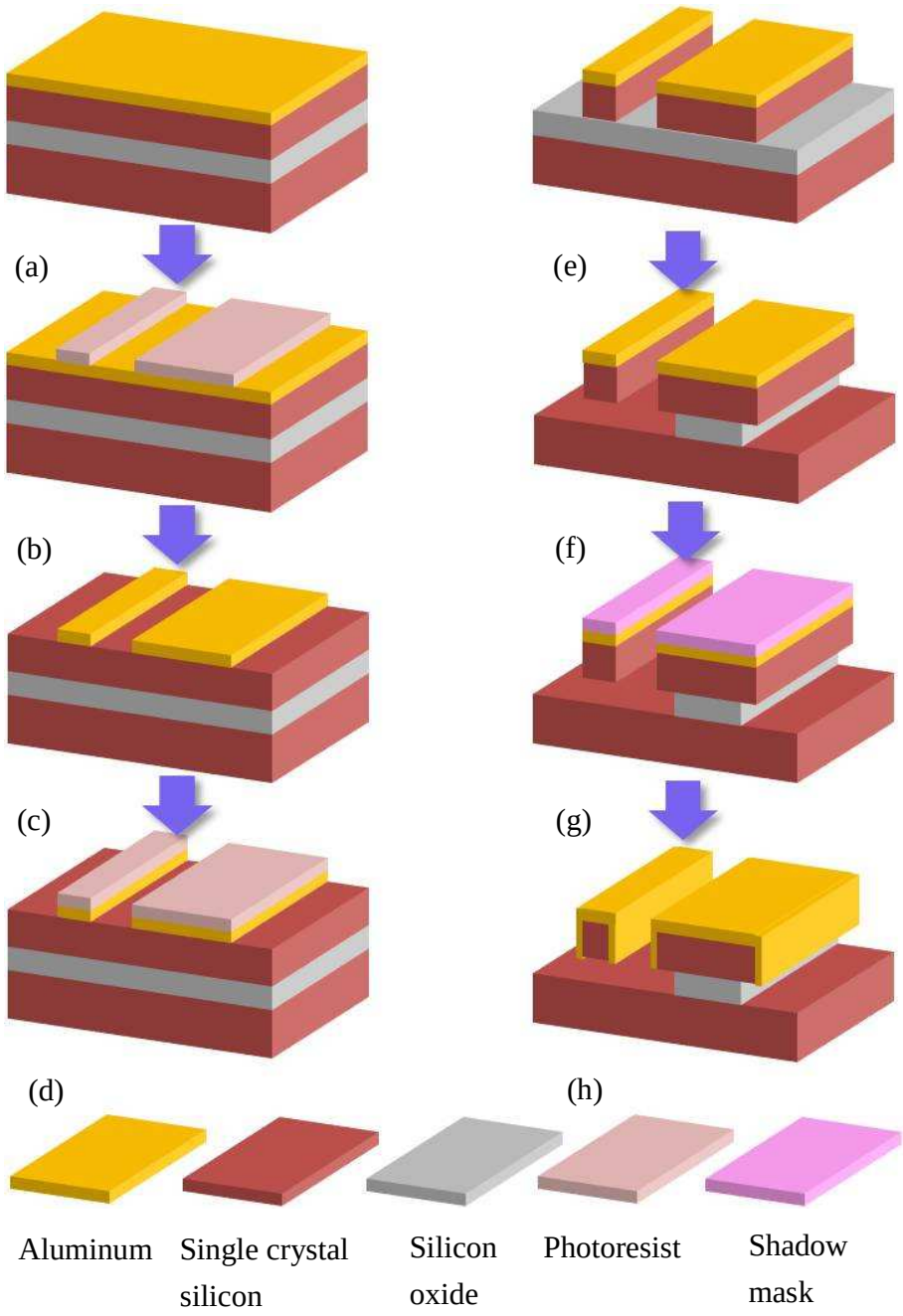

Fig. 5.7: Schematic of the process flow for tunable metamaterials. The fabrication process flow consists of eight steps which are shown from (a) to (h). The inserts show the legend of the colors which represent different materials.

Fig. 5.7 shows the process flow developed for the fabrication of tunable metamaterials. The process flow is derived from a stander process used for the fabrication of MEMS photonic devices which can be divided into eight steps as addressed in Fig. 5.7 ((a) to (h)). Here, different colors are used to represent different materials which are shown in the inserts below.

First of all, a thin aluminum film is coated on the SOI wafer using the sputtering deposition. This makes a four-layer structure which is shown in Fig. 5.7 (a). The first layer is the 0.5-μm aluminum thin film which is used for the metal structure of the metamaterial unit cells. The second layer under the aluminum thin film is a 75-μm single crystal silicon used for the substrate of the unit cells. The third layer is the 2-μm silicon oxide layer which is used as the stop line for the etching process. The last layer is a 600-μm thick single crystal layer serves as the back side of the whole structure. The thickness of each layer can be adjusted for different fabrication purposes.

The second step shown in Fig. 5.7 (b) is to pattern a photoresist (PR) layer and a hard mask layer according to the design of the unit cells so that the unwanted part of metal film can be removed. It should be point out that a hard mask (silicon dioxide thin film) is deposited for the etching process of microstructures such as unit cells, comb-drive actuators and supporting structures. The PR layer is used for the protection of the hard masks during the etching for the dicing lines which is a stander process during the DRIE etching for silicon based photonic circuits and will not be further discussed. Such multi-layer patterning method is used for the etching from the structure layer (75-μm

single crystal silicon) to the back side layer (600-μm single crystal silicon) and keeping all the other parts protected by the PR.

After the depositing of the hard mask and PR, the unwanted part of the metal thin film is removed by the lam etching (Fig. 5.7(c)). In this way, the metal parts of the unit cells such as the split rings and wires can be patterned directly on the structure layer of the SOI wafer. The metal patterns are limited by the minimum feature size of the photo masks which is 1 μm in this fabrication.

Then the PR is patterned on the top of the metal layers and some parts of the 75-μm single crystal layer to protect the micro-structures during the DRIE etching process (Fig. 5.7(d)). In this fabrication process, some parts of the metal pattern have very large silicon substrate so that they will not be released after short releasing time. However some metal parts have very small silicon substrate which can be easily released.

DRIE process is applied for the etching of the silicon micro-structures after the pattern of the PR (Fig. 5.7(e)). The uniformity of the substrate side wall is controlled by the sidewall passivation process which is realized by vertically etching the silicon substrate one short distance per step.

Wet releasing (Fig. 5.7(f)) is the most critical step during the whole process flow. After the DRIE process for silicon micro-structures, the movable part of the unit cells is released with buffered oxide etchant (BOE). The BOE will etch the silicon oxide layer both below the movable parts and the fixed parts of the unit cells. However, the substrate of the movable parts is much smaller than that of the fixed parts. As the results, the releasing time of the movable parts of the unit cells is much shorter than that of the fixed

parts of the unit cell. By controlling the releasing time, the movable parts of the unit cell is released while the fixed parts are still stick to the backside of the 600-μm silicon. It should be pointed out that the releasing process of the comb drive happens simultaneously with that of the movable parts of the unit cells. Therefore, it is better both of the comb drive and the unit cell movable parts have the same releasing time. The releasing time is controlled by two major conditions. One is the chemical and the concentration of the chemical solution. The other one is the size and spacing of between each micro-structure. The movable parts and comb drives are designed to be 3 μm both in width and in spacing between adjacent micro-structures.

After wet releasing, a shadow mask is used for pattern the metal thin film on the side wall of the unit cell gaps in order to ensure the electrical contact when the displacement of the movable part reaches its maximum or its minimum (Fig. 5.7(g) and Fig. 5.7(h)). In this way, the geometry of the unit cells can be changed from split ring to shape "□" or shape "I'. The coating of the side wall metal is done by BLAXER sputtering system (Sitek Process Solution Inc.). The thickness of the side wall coating is 0.2 μm.

In summary, the tunable metamaterial is fabricated using the DRIE process derived from the MEMS photonic fabrications process. The fabricated unit cells are consisted with two parts one movable parts and one fixed parts which is realized by the controlled wet releasing process. Theoretically speaking, the over etching phenomenon caused by long etching time of the DRIE process can be used for releasing the movable structures without wet release. However the uniformity of the substrate cannot be guaranteed in this process.

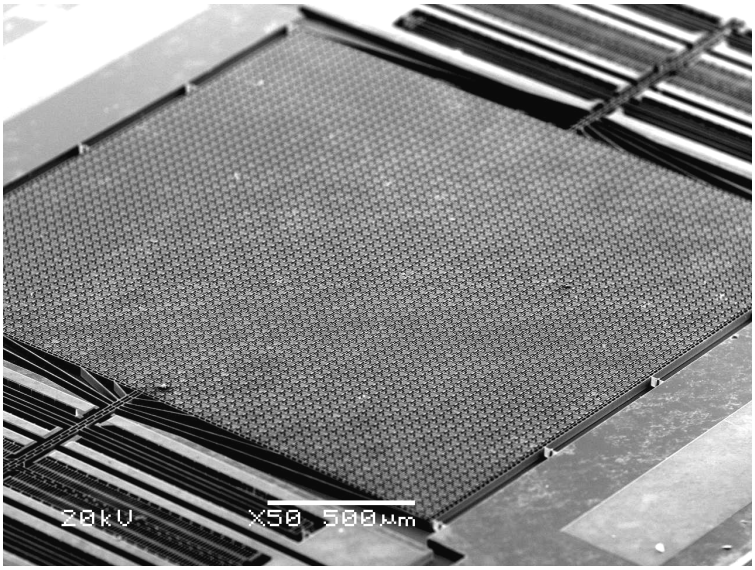

(a)

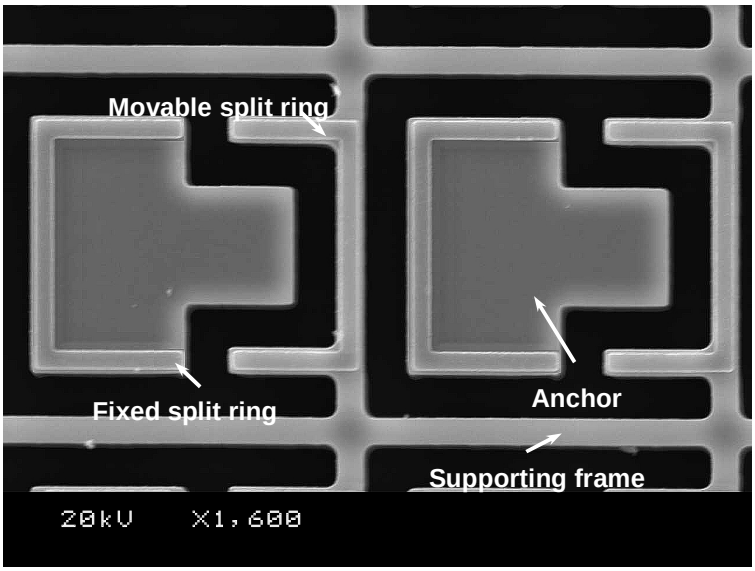

(b)

Fig. 5.8: Scanning electron micrographs of the fabricated tunable magnetic metamaterial. (a) Overview of the structures and (b) close-up of the unit cells.

The fabricated tunable metamaterial is shown in Fig. 5.8. An overview of the micromachined tunable magnetic metamaterial is shown in Fig. 5.8(a) using the scanning electron microscopy (SEM). Two identical electrostatic comb drive actuators are placed on both sides of the unit cell array. Each actuator provides bidirectional in-plane translation following the actuation relationship $\Delta x = AV^2$, where Δx is the displacement, V is the actuation voltage and $A = 0.04\ \mu m/V^2$ is the actuation coefficient. Close-up of the unit cells is shown in Fig. 5.8(b). The semi-square split rings are formed by patterning an evaporated aluminum layer (0.5 μm thick) on top of the SOI wafer. The side length of the split ring R is 19 μm and the gap between the two semi-squares G is 4 μm after fabrication. The width of the aluminum strip W is 2 μm and the period of the unit cell array is 25 μm. The movable split rings are patterned on the supporting frame, which is made of many crossed narrow beams (2 μm width). The fixed split rings are patterned on the isolated anchors. The "T" shape of the anchors is to ensure the surrounding trenches (between the anchors and the supporting frame) to have the same width (4 μm). Since all the trenches have to be etched off in the deep etching process, the same width ensures the same etching speed over different areas and thus simplifies the process control. Each anchor encloses larger areas of the underlying oxide layer than the supporting frame. This ensures that in the HF release some oxide under the anchors still remains when the oxide under the supporting frame is fully removed.

As a result, the anchors are well fixed on the substrate while the supporting frame is freely movable. With these design considerations, the fabrication yield reaches almost 100%.

5.4 Experimental results and discussions

The electrical response of the split ring unit cells is analyzed numerically and experimentally before a further discussion on the magnetic response of the tunable metamaterial is conducted. There are three major parameters which affect the response of the tunable metamaterial to the external electric field: the side wall length *R*, the period *P* and the gap width *G*. Those parameters determined the coupling strength between the unit cells and split rings which is critical to the resonance condition of the external electric field. However, in particle tuning process base on MEMS technology, the tuning of the side wall length and period is not feasible once the tunable metamaterial is fabricated. On the other hand, the tuning of the gap width *G* can be easily realized by the design of the tunable metamaterial discussed in the previous sections.

5.4.1 Electrical response

According to the numerical analysis, the changing of the split ring unit cell geometry can tune the electrical response of the metamaterial. The largest tuning range is achieved by changing the size of the unit cell which is not feasible from the practical point of view. The alternative way to tune the geometry of the unit cells is to change the gap distance which is easier to be achieved using MEMS technology. In this section, the tunable metamaterial with tunable gap distance *G* is experimental demonstrated.

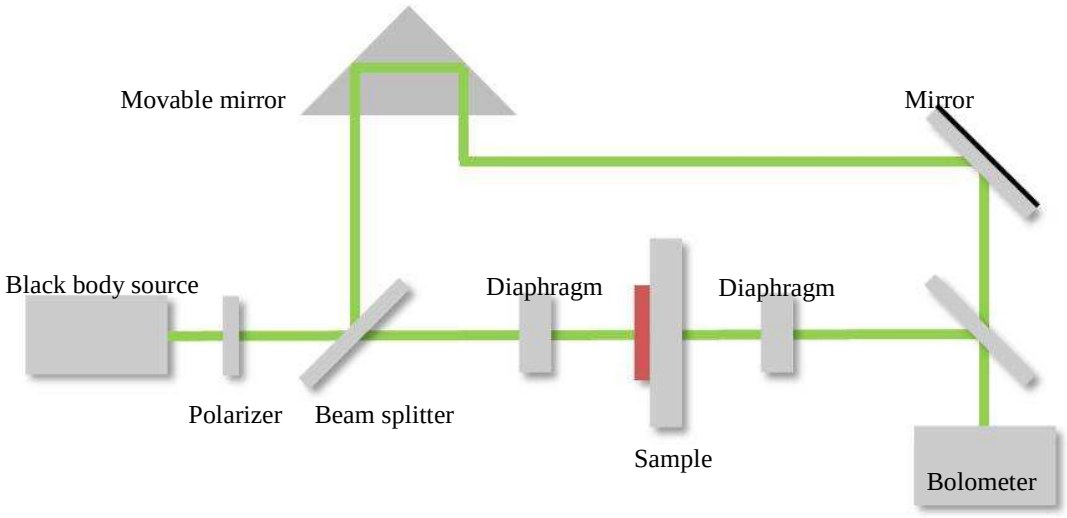

Fig. 5.9: The schematic of the experiment setup.

The experimental setup is shown in Fig. 5.9. The transmission spectrum of the tunable metamaterial is measured by the vacuum FT-IR spectrometer (VERTEX 80v) from Bruker Optics. The resolution is 0.5 cm^{-1} in wave number which equals to 0.015 THz in frequency. The black body source is used as the THz light source which has a broad band emission from 0.1 THz to 10 THz. The THz light is polarized by the polarizer and a diaphragm is used to convert the spot size of the light according to the size of the sample (4 mm × 4 mm). A sample holder is used to fix the sample which is perpendicularly to the incident light source during the experiment. The signal light is collected by the bolometer and analyzed by a computer using Fourier transform method. During the experiment the comb drive is controlled by two source measurement units (SMU). The gap width *G* of the split ring resonator can be tuned during the experiment by controlling the pumping electric voltage from the SMU.

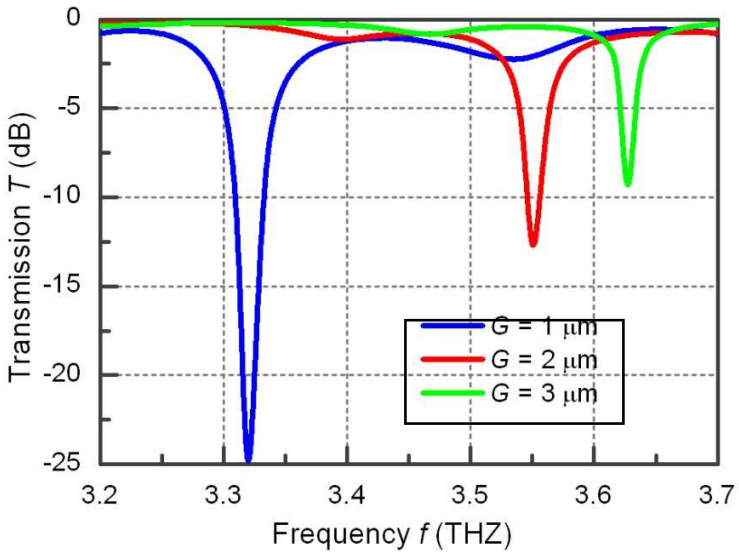

Fig. 5.10: The measured transmission spectrum at different gap width (G =1 μm black dotted line with square, G = 2 μm red dotted line with circular, G = 3 μm blue dotted line with triangle). The inserts shows the simulated electrical field distribution at each gap position.

The measured tunable metamaterial has a unit cells array of 160 × 160 with the period of 25 μm. The side wall length R is 19 mm and the metal strip width is 3 μm. The substrate width is around 100 μm.

The measured transmission spectrum at different gap width is shown in Fig. 5.10. The black dotted line with square shows the transmission spectrum when the gap width is 1 μm. The red dotted line with circular and the blue dotted line with triangle shows the transmission spectrum when the gap width is 2 μm and 3 μm respectively. The increasing of the gap width results in the shifting of the dip frequency to higher frequency region which agrees with the prediction of the simulation results (Fig. 5.5(a)). It can be seen

from Fig. 5.10 that the dip depth of the resonance becomes shallow as the gap width *G* is increasing. This can be explained by the change of the quality factor of the split ring resonator. The quality factor is a very important parameter indicating the capability of a resonance cavity to keep the resonant energy from all kinds of losing, such as radiation loss, absorption or coupling to the outside. It can be seen from the inserts of Fig. 5.10. The smaller the gap width is, the stronger the confinement of the cavity resonance energy. The lager gap width actually weakens the coupling of the semi-squares within the split ring resonator unit cells which makes it easier for the confined light to leak to the outside. Furthermore, when the semi-squares from the adjacent unit cells has a stronger coupling strength than those within the one split ring unit cell, the shape of the unit cell become more like "I" shaped unit cell than split ring resonator Fig. 1(a). Therefore, the original resonance mode trends to vanish as the gap further increased which also explains the reason why the quality factor decreases as the gap width *G* is increasing.

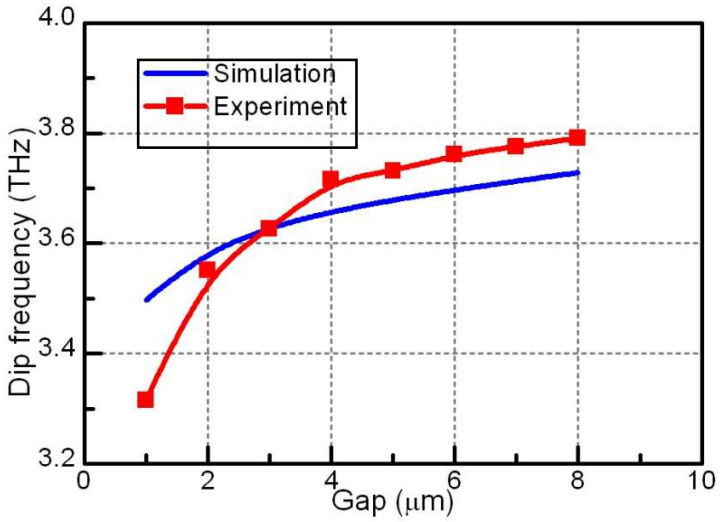

Fig. 5.11: The measured dip frequency versus the gap tuning (red square). The dashed line shows the simulation results.

The measured dip frequency versus the gap tuning is summarized in Fig. 5.11. The dip frequency is tuned from 3.3 THz to 3.8 THz as the gap width G is changing from 1 μm to 8 μm. The tuning range is around 0.5 THz which is 15% of the initial dip frequency. It should be pointed out that the sensitivity of the gap width change ΔG becomes smaller as the gap increasing. This can be explained by the following reasons: Firstly, the electric field is highly confined between the gaps when G is very small which makes the resonance mode is very sensitive to the gap changing. Secondly, the quality factor is reduced as the gap is increasing which reduce the sensitivity of the cavity resonant mode. In this experiment, the split ring unit cells are not side coated which means the air gap between the two semi-squares are still exists even the gap width G reaches its maximum 8 μm. However the frequency dip become very shallow (< 5 dB) when the air gap become large enough (> 7 μm).

5.4.2 Magnetic response

General speaking, conventional materials which response to the incoming magnetic field are far more rare than those response to the dielectric field in nature. That is because the magnetic polarization in nature molecular is guided by either the orbital current or the unpaired electron spins. Therefore, the magnetic resonance, which is analogy to the phonon resonance which enhance the electric response at the frequency region of infrared or above, happens mainly at frequency region below THz. However, magnetic response of materials at THz region or above has lots of application on devices such as super lenses, magnetic mirrors, cloaking devices and filters. Nature materials which response to the magnetic field above the gigahertz region are typically narrow band and have weak response to the external magnetic field which limit their applications The study on the magnetic metamaterial in THz region will surely benefit the THz optics and their applications. Therefore, magnetic metamaterials working at high frequency region has been studied in many works.

The electrical response of the tunable metamaterial is demonstrated in pervious section which shows that the electrical response of the metamaterial can be tuned using MEMS technology without changing the refractive index of the compositing material. However, the electrical resonance frequency of the designed tunable metamaterial is too high to apply the effective medium theory on ($\lambda \approx 3P$). In this section, the magnetic response of the tunable metamaterial is studied to demonstrate the tuning of the tunable metamaterial as an effective homogenous material.

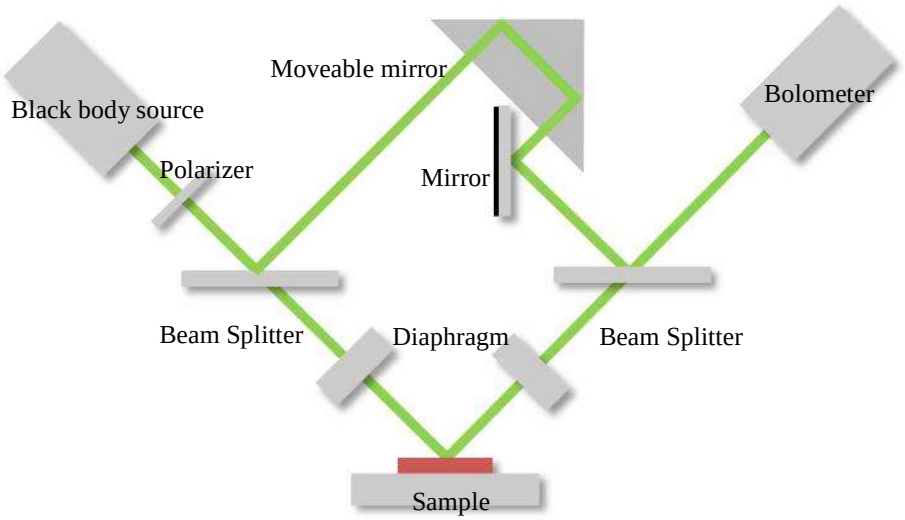

Fig. 5.12: the schematic of the experiment setup

The reflection spectrum of the tunable metamaterial is measured by the vacuum FT-IR spectrometer (VERTEX 80v) from Bruker Optics. Fig. 5.12 shows the setup of the experiment. The broadband THz light ranging from 0.1 THz to 5 THz is generated by the black body radiation and the polarization state is controlled by a THz polarizer. The spot size of the light source is controlled by the diaphragm according to the size of the sample (4 mm × 4mm). The reflected light from the sample is gathered by the bolometer cooled by liquid helium. The sample hold is rough glass plate with 1 cm thickness which can absorb and scatter the unwanted incident light. Both the polarizer and the incident angle are controlled mechanically by the integrated motor. The resolution is set to be 2 cm^{-1} and the scan time is 32 minutes which give the average results of around 2000 scan times.

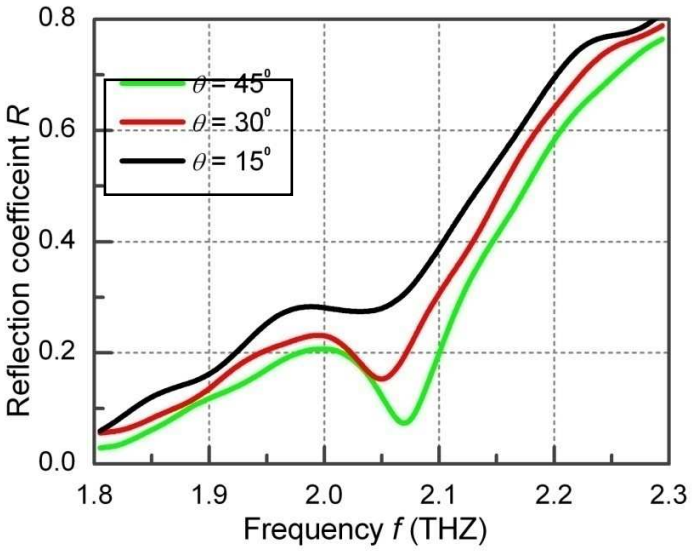

(a)

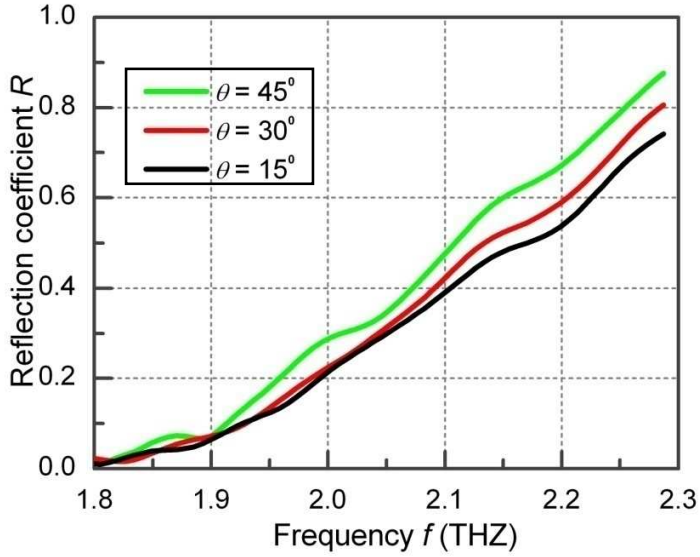

(b)

Fig. 5.13: The measured reflection spectrum of the tunable metamaterial when the incident EM wave is (a) TE and (b) TM polarized. The spectrum is measured at different incident angles (black 15°, red 30° and green 45°)

The reflection spectrum of the tunable metamaterial is measured at different incident light polarization and different incident angles (Fig 5.13). The spectrums of different incident angles are plotted using different colors. It can be observed that the resonant frequencies that correspond to the dips of the spectra are quite close to each other (around 2.05 THz). Since the electric field is always parallel to the unit cell surface, the change of the incident angle has little effect on the electric response of the tunable magnetic metamaterial. However, incident angle does change the orientation of the magnetic field. With the increase of the incident angle from 15° to 45°, the vertical component of the magnetic field becomes larger and larger and thus the dip is lowered further. When the polarization is changed to the TM state (the magnetic field is transverse to the incident plane), the dips of the resonance disappear as shown in Fig. 5.13(b). This is expected since the magnetic field no longer has vertical component to the surface of the unit cells. The slope of the measured reflection spectrum (Fig. 5.13) is larger than that of the simulated reflection spectrum (Fig. 5.11), because the light emitted by the black body source is not even at the measurement frequency range.

To further examine the tunability of the magnetic response, the reflection spectra of the magnetic metamaterial are measured at different gap widths. The incidence is always in the TE polarization. Fig. 5.14(a) shows the measured reflection coefficients when G is tuned from 0 to 8 μm with a step of 2 μm. In the extreme cases of G = 0 and 8 μm, the geometrical shapes of the unit cell correspond to the closed ring and the "I" shape (see Fig. 5.1(c) and (d)), respectively. Therefore, the unit cells are no longer SRRs and do not have the magnetic response in the measurement frequency region (1.8 – 2.3

THz). When the gap width is increased from 2 to 6 μm, the resonant frequency is blue shifted but the dip becomes shallower. The shallowness indicates that the coupling strength between the two semi-square split rings is reduced. The dip vanishes when the gap become 8 μm which means the pervious resonance mode no longer exists as the geometry of the unit cell is totally changed. The experimental observations show clearly that the magnetic response of the tunable magnetic metamaterial can be changed drastically by reshaping the unit cells.

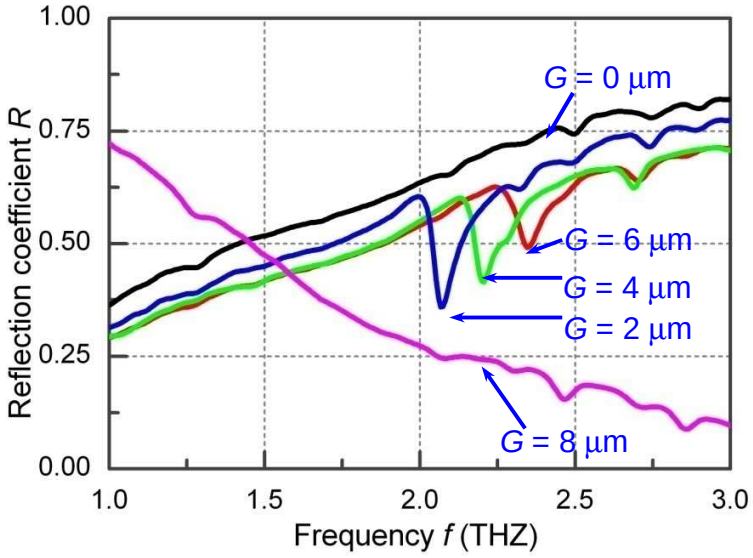

Fig. 5.14: The reflection spectrum of the tunable metamaterial when the gap is tuned from 0 μm to 8 μm with a step of 2 μm. The different colors stand for different gap width (black 0 μm, blue 2 μm, green 4 μm, red 6 μm and pink 8 μm).

It is clear that both the electrical and magnetic response of the split ring resonator metamaterial can be tuned by reshaping the unit cells. However, the effect of the unit cell

geometry change on the material properties cannot be read directly from the transmission or reflection spectrum. In the next section, the effective permeability of the split ring resonator metamaterial is studied under different gap width *G*.

The unit cells of metamaterials are often designed to mimic the molecular of the natural materials. A single unit cell is nothing but a sub-wavelength resonator. However, metamaterials consists of a large amount of unit cell can be described using the effective medium theory. There are several methods which have been introduced to retrieve the effective parameters form the simulated or experimental data of the metamaterials. For example, the field averaging method, the S-parameter retrieval method and the Fresnel fitting method. The field averaging method average the local electric and magnetic field to obtain the macroscopic values of the *E*, *D*, *B* and *H* fields. The effective permittivity and permeability can be derived from the averaged field values. The field averaging method is a quick method to retrieve the effective parameters of the materials. However the inaccuracy is introduced by the averaging process. S-parameter retrieval method requires the information of the transmission coefficient and reflection coefficient which can be obtained by either the simulation or the measurement. The S-parameter retrieval method has long been used for characterization of the micro-structures at radio frequencies (RF) and microwave frequencies. A single frequency S-parameter simulation or measurement needs to obtain four values to obtain both the real and imaginary part of the effective permittivity and permeability: The phase and amplitude of the transmission and reflection. The S-parameter retrieval method is advanced in excluding the incorrect solutions by enlarging the simulation or measurement frequency range. However, the S-

parameter retrieval method also has some draw backs: The phase information is quite difficult to be obtained by the experiment when the frequency region is at THz or higher. Some works using the S-parameter retrieval method characterize the metamaterial samples working at infrared frequency region with the amplitude information only. This method helps on the design of the metamaterials which have certain magnetic and electric response to the incident EM wave. But it depends on the consistency of the transmission and reflection coefficients and cannot give a direct quantification of material properties on THz region or above. Additionally, the S-parameter retrieval method is restricted to wave incident perpendicularly to the surface of the unit cell arrays to simplify both the numerical and analytical expressions. Therefore, the S-parameter retrieval method cannot be applied to obtain the effective permeability of the tunable metamaterials demonstrated here.

In this work, Fresnel fitting method is applied to derive the effective permeability of the tunable metamaterial. The Fresnel fitting method has been widely used in the optical spectroscopy and recently been introduced to characterize the material parameters of metamaterial structure. The Fresnel equations can be used for oblique incidence waves. The measurement of the reflected or transmitted wave magnitude at different incident angles can be used to compensate the absence of the phase information. The Fresnel fitting method actually provides a regious method to obtain the effective permeability and permittivity from the experimental data in arbitrary material in which the effective permeability and permittivity can be properly defined. Although it is possible to apply the Fresnel fitting method at every give frequency, the fitting process

can be greatly shortened if the function forms of the permeability and permittivity is already known. The Fresnel fitting method greatly reduced the requirement for the experiment studying the material properties of the met material.

The response to the electrical and magnetic field of continues medium can be described by two 3 × 3 tensor which stands for the permittivity $\varepsilon(\omega)$ and the permeability $\mu(\omega)$, regardless the coupling between the magnetic and electric field.

$$\varepsilon(\omega) = \begin{pmatrix} \varepsilon_{xx}(\omega) & 0 & 0 \\ 0 & \varepsilon_{yy}(\omega) & 0 \\ 0 & 0 & 1 \end{pmatrix} \tag{5.4}$$

$$\mu(\omega) = \begin{pmatrix} 1 & 0 & 0 \\ 0 & 1 & 0 \\ 0 & 0 & \mu_{zz}(\omega) \end{pmatrix} \tag{5.5}$$

Where *x*, *y* stands for the direction parallel to the surface of the split ring resonator. *x* stands for the direction along the gap while *y* stands for the direction along the side wall of the split ring. *z* stands for the direction perpendicular to the surface of the unit cell.

The Fresnel equations can be derived from Maxwell's equation by solving the boundary-value problem at the various material interfaces.

$$t = \frac{e^{-ik_z d}}{\cos(q_z d) - \frac{i}{2}\left(\frac{\mu_{zz} k_z}{q_z} + \frac{q_z}{\mu_{zz} k_z}\right)\sin(q_z d)} \tag{5.6}$$

$$r = \frac{\frac{i}{2}\left(-\frac{\mu_{zz} k_z}{q_z} + \frac{q_z}{\mu_{zz} k_z}\right)\sin(q_z d)}{\cos(q_z d) - \frac{i}{2}\left(\frac{\mu_{zz} k_z}{q_z} + \frac{q_z}{\mu_{zz} k_z}\right)\sin(q_z d)} \tag{5.7}$$

Where q is the wave vector in medium and k is the wave vector in vacuum. d is the thickness of the unit cell.

To simplify the calculation the electrical and magnetic response for the split ring resonator can be described as follows,

$$\varepsilon_{xx}(\omega) = \varepsilon_s - \frac{A_e \omega_p^2}{\omega^2 - \omega_{e0}^2 + i\omega r_e} \tag{5.8}$$

$$\mu_{zz}(\omega) = \varepsilon_s - \frac{A_m \omega^2}{\omega^2 - \omega_{m0}^2 + i\omega r_m} \tag{5.9}$$

The $\varepsilon_{xx}(\omega)$ and $\mu_{zz}(\omega)$ satisfy,

$$\frac{q_y^2}{\mu_{zz}} + \frac{q_z^2}{1} = \omega^2 \varepsilon_{xx} \tag{5.10}$$

The material parameters ($A_e, A_m, \omega_{m0}, \omega_{e0}, \omega_{mp}, \gamma_m, \gamma_e, \varepsilon_s$) can be derived by submitting Eq. 5.8 and Eq. 5.9 to Eq. 5.7 and fitting the experimental results in Fig. 5.14.

All the parameters are given an approximate in the first place. Then Eq. 5.7 is calculated by the MATLAB program and the results are compared with the experiment results. The simulated spectrum derived by Eq. 5.7 is plotted once the least square reaches the threshold value. The best fitted value is chosen according to the reflection spectrum from Fig. 5.14.

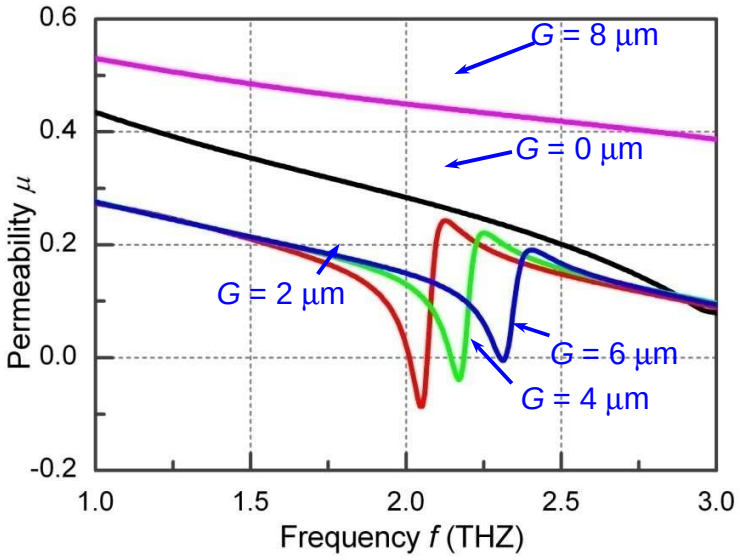

(a)

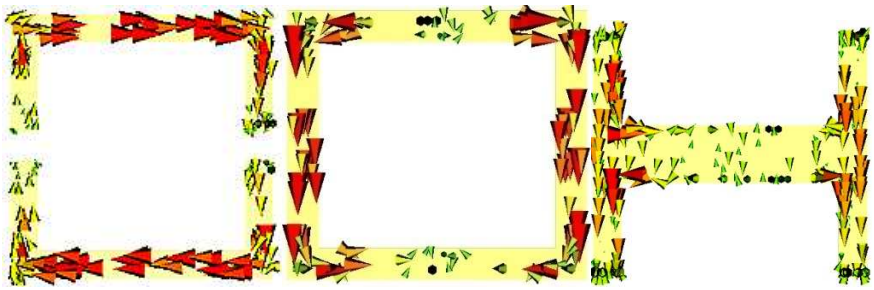

(b) (c) (d)

Fig. 5.15: (a) The effective permeability m at different gap width *G*. The effective permeability is derived from the reflection coefficient using the Fresnel fit method. (b),

(c) and (d) shows the surface current when the gap width is 2 μm, 0 μm and 8 μm respectively.

The results are shown in Fig. 4 (b). For G = 0 and 8 μm, the permeability has no resonant dips and decreases monotonically with the increase of frequency. For the other gap widths, the dips experience the same blue shift as those shown in Fig. 4 (a). It is interesting to see that the effective permeability could go to negative at the dips, for instance, at the frequency 2.05 and 2.19 THz for G = 2 and 4 μm, respectively. At a fixed frequency 2.05 THz, the permeability is tuned from -0.1 to 0.5 as G is increased from 2 to 8 μm. The insets of Fig. 4(b) show that the surface current of the SRR (G = 2 μm) is quite different from those of the closed ring and the "I"-shaped unit cells. The SRR unit cell has strong surface current and forms circle current when the incident frequency is around 2.05 THz. It explains the reason of negative permeability near this frequency. In contrast, the permeability of the closed ring unit cell or the "I"-shaped unit cell never becomes negative within the measurement frequency region since they cannot form the circle current in the absence of the gap.

5.4.3 Light speed modulation

Slow light is one of the promising applications of metamaterials the dispersion of which can be designed to slow down the group velocity of light. Slow light can delay or even store the light in all-optical memories. As photons normally do not strongly excite materials which are transparent at their frequency, slowing down the light can enhance the light-material interaction and induce nonlinear effects. Therefore, materials that can

slow light down have potential applications on light storage, optical regenerator, optical switch and optical buffer etc. Generally speaking, there are two kinds of approaches that can slow down the group velocity of the light. One is to use the material resonance, such as the absorption resonance of an atomic vapor or the stimulated Brillouin scattering. The other method is to use the artificial materials with microstructures, such as the array of micro ring resonators, the coupled resonator optical waveguide and photonic crystals. The unit cell of the metamaterials is analogy to the atom or molecular of the nature materials. Therefore, it can be used to slow the light down by design the resonance condition of the unit cells. The electromagnetically induced transparency (EIT) is reported in many works on metamaterials which has the slow light factor up to 200.

Most of the slow light devices can slow the light speed down to a certain scale. However, the devices that can modulate the group velocity of the light propagating through are rare due to the following reasons. For slow light devices using the material resonance, the resonance is depended on the energy level of the atoms or molecular. Therefore, the material resonance is highly depended on the wavelength of light and not easy to be controlled. On the other hand, the change of the refractive of the nature materials plays a important role in the control of slow light devices which are using the resonance nature of the micro-cavities such as the couple resonant optical waveguide and photonic crystals. The change of the resonance modes of such micro-cavities is achieved by exciting or even changing the compositing materials. Therefore, those micro-cavities are often designed to have high quality factors to improve the effect of the compositing material refractive index change. However, the high quality factor of such micro-cavities

also limits the bandwidth of the transmitted frequencies. Therefore, the modulation of the light speed in such devices is not easy to be achieved. The tunable material using MEMS system does not depend on the refractive index change of the compositing materials. The tuning of such tunable material is achieved by reshaping the metamaterial unit cells. Therefore, it is can be useful to build the devices which can modulate the light speed reversibly. Although the reported tunable metamaterial with split ring unit cell is not designed for the purpose of slowing light or tuning the speed of the light. The light speed modulation effect is observed during the experiment of the tunable metamaterial on the THz time domain spectroscopy (TDS),

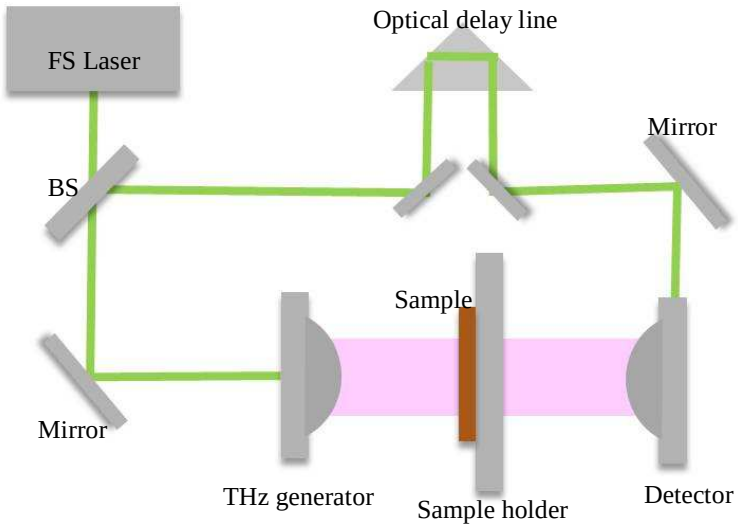

Fig. 5.16: The experiment setup of THz-TDS.

The experiment setup of THz-TDS is shown in Fig. 5.16. The THz pulses are generated by an ultra short 0.02 ps) pulsed laser which comes from the 780 nm femtosecond laser. This single pulse contains the frequency components covering the

frequency span from 0.06 THz to 3 THz. The electrical field of the THz pulse passing through the sample is collected by the detector which are controlled by the coherent beam comes from the femtosecond laser.

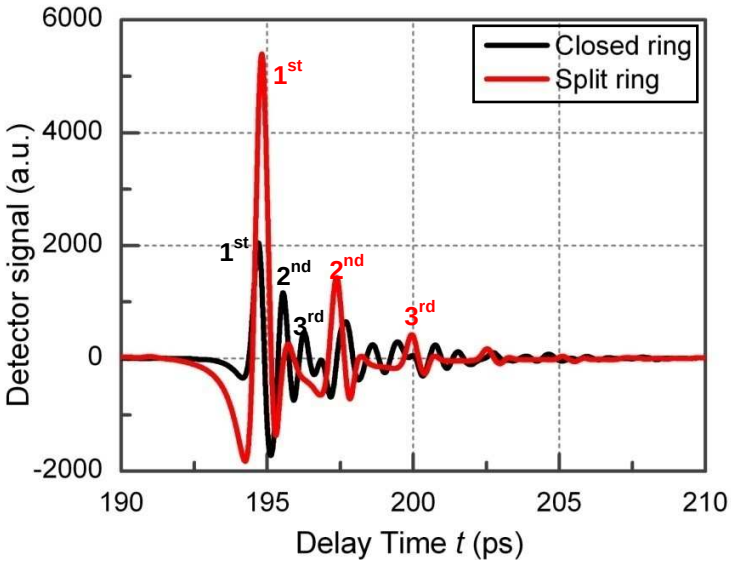

(a)

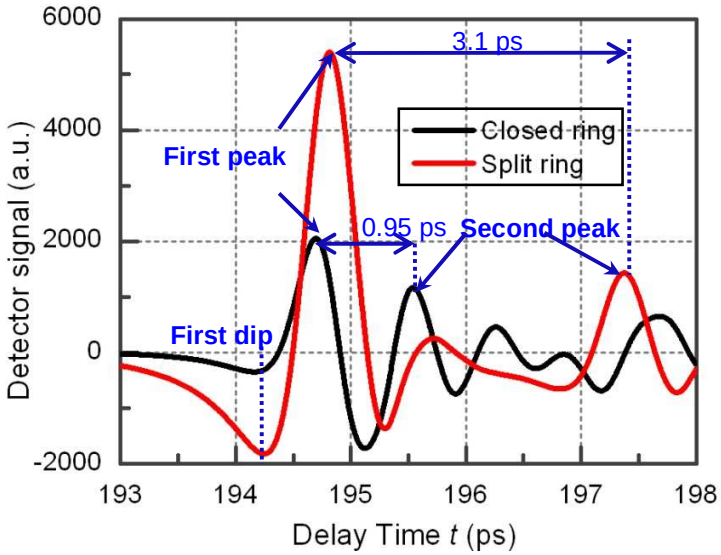

(b)

Fig 5.17: The Detector signal as the function of time for both closed ring $G = 0$ (closed ring) and $G = 2$ (split ring). (a) the Detector signal at a long time span. The peaks marks with 1^{st}, 2^{nd} and 3^{rd} indicated the times of the THz pulse resonate within the sample. (b) the zoomed in graph showing the time delay of the first peak and second peak.

Once the 780 nm laser beam shut on the detector, it will record the electric field of the signal at that time point. The record time is controlled by varying the delay time of the optical delay line. It is possible to record the signal as the function of time by recording the signal at different delay time.

The detector signal as the function of the time is shown in Fig. 5.17. The red line shows the detector signal of the split ring metamaterial when the gap width $G = 2$ mm and the black line stands for the unit cell structure of the closed ring when the gap width $G = 0$. Fig. 5.17(a) shows the detector signal at long time span (190 ps – 210 ps) which contains several peaks. When the THz pulse is incident on the sample, some of the pulse energy pass through the sample and reaches the detector without delay. This energy is shown as the first dip in the detector. The time when the first dip comes to the detector is almost the same because the physical length of the sample is always the same (100 mm) no matter how the gap width is tuned. However, energy of the THz pulse does not pass through the sample simultaneously. Some of the energy is reflected by the metamaterial-air interface and resonant within the sample. The energy of the THz pulse is radiated by the sample each time the pulse energy reaches the boundary of the sample. This explains the peaks of the detector signal function. The time difference of each peaks equal to the time needed by the THz pulse to pass through the sample. The time difference of the

closed ring structure is 0.95 ps as shown in Fig. 5.17(b). This is similar to the time for the THz pulse to travel through the 100 mm thick silicon (The refractive index of the silicon substrate is around 3 at THz region). This is because the electrical resonance is not quite strong as the gap vanished. The closed ring unit cell cannot form a very strong resonance to increase the photon life time thus make the light slowed down. However, things are different to the split ring unit cell. The peak separation of the split ring unit cell is 3.1 ps which is approximate three times of the peak separation for the closed ring. In other words, the light speed is slowed down by the factor of 3 when the gap width is tuned from 0 mm to 2 mm.

5.5 Summary

In this chapter, a tunable metamaterial using the MEMS technology is numerically analyzed and experimentally demonstrated. This chapter is divided into five parts. Firstly, the design of the tunable metamaterial is shown in §5.1. The unit cell of the tunable metamaterial consists of two separated semi-squares (Fig. 5.1) the gap between which can be tuned by the MEMS comb drives. The unit cell geometry can be changed from split ring unit cell to shape "□" or shape "I" unit cell when the gap width is tuned to reach its minimum and its maximum respectively. The tunable metamaterial is fabricated using the DRIE process which is shown in is shown in §5.2. The fabricated unit cells are consisted with two parts one movable parts and one fixed parts which is realized by the controlled wet releasing process. In this particular fabrication process for split ring unit cells the releasing time is controlled around 15 minutes. Theoretically speaking, the over

etching phenomenon caused by long etching time of the DRIE process can be used for releasing the movable structures without wet release. However the uniformity of the substrate cannot be guaranteed in this process. The fabricated tunable metamaterial unit cell has the side wall length R = 19 μm, the initial gap width G = 4 μm and the period P = 25 μm. The tunable metamaterial sample has a unit cell array of 160 × 160 which is around 4 mm × 4mm. The optical properties of the tunable metamaterial are tuned by changing the geometry of the unit cells which is the "molecular" of the metamaterials. §5.3 demonstrate the electrical response of the tunable metamaterial. The numerical study on the geometry tuning of the unit cell is firstly given and then followed by the experimental results of the transmission spectrum on gap tuning. According to the experiment results, the electrical resonance frequency of the tunable metamaterial can be tuned from 3.3 THz to 3.8 THz via the unit cell gap change which is around 15% of the initial resonance frequency. The magnetic response of the tunable metamaterial is demonstrated in §5.3. The magnetic resonance is induced by the tilted incident EM wave which as the magnetic component perpendicular to the surface of the unit cells. The magnetic resonance frequency is 2.19 THz at the initial state G = 4 μm. The magnetic resonance frequency shits to higher frequency region when the gap width is increasing and the measured resonance frequency is vanished as the gap between the two semi-squares is vanished G = 8 μm and G = 0 μm. The effective permeability as the function of incident frequency is derived by the Fresnel fitting method which fit the measured reflection spectrum by the Fresnel equation. An interesting result is shown in Fig. 5.15 that the effective permeability can be tuned from the negative (-0.1) to positive (0.5)

region. Finally, §5.4 demonstrate the tuning of the light speed using the tunable metamaterial which is the potential application of such devices based on the tunable metamaterials. The experiment results show the measured light speed of such tunable metamaterials is tuned by the factor of 3 when the unit cell geometry is changed from the split ring resonator to the closed ring resonator.

CHAPTER 6

CONCLUSION REMARKS

6.1 Conclusions

In this PhD project, three different approaches have been studied for tunable photonic devices based on MEMS technology. First, the optical double barrier structure has been numerically studied and experimentally demonstrated as the thermo-optical switch, switchable polarizer and optical tunneling junctions integrated as reconfigurable WDM system. The coupled FP cavities and digital mirrors have been demonstrated as thermo-optical switch and wavelength selective mirror for tunable lasers. Second, the slow light structure using metamaterial with coupled split ring unit cells is numerically analyzed. Finally, a tunable magnetic metamaterial is demonstrated using MEMS technology.

In the study of *double optical barriers structures*, three different tunable photonic devices has been demonstrated using thermo-optical tuning. *A thermo-optic switch* is realized using MEMS technology. The device is fabricated on silicon-on-isolator wafer using deep etching process. The transmission of the optical switch is controlled by the optical length of the central rib which is thermally controlled by the external pumping current. In experiment, it measures a switching speed of 1 μs and an extinction ratio of 30 dB. *A switchable polarizer* is demonstrated using the double optical barrier structure

which transmit the light with one polarization state and filter out the others. In experiment it measures a PER of lager than 23 dB when the pumping current is above 60 mA. The switching time is shorter than 125 μs which is limited by the polarization analyzer used in the experiment. *A MEMS reconfigurable add-drop multiplexer* is realized by applied the optical tunneling structure to the ribbed waveguide. The tunable add-drop multiplexer is based on Y-shape optical double barriers tunneling junction which are realized by MEMS technology. In the experiment, a five-channel prototype of the tunable add-drop multiplexer is demonstrated. The measured output is ranged from 1549.24 nm to 1559.21 nm.

In the study of the metamaterials with coupled SRR unit cells, *a tunable slow light metamaterial* via tuning the substrate refractive index is numerically studied. The couple SRR unit cell is proposed and numerically characterized. The simulation results show that the coupled SRR design improves the tunability of the effective permittivity and the effective permeability by 70 and 200 times, respectively. The required permittivity change is only 0.025, which can be achieved by either thermal-optic effect or photon induced free carrier effect of the semiconductor materials. It may find potential applications in data storage, photonic circuits, optical communications and bio-sensors.

In the study of magnetic metamaterials, *a THz tunable metamaterial* using the MEMS technology is numerically analyzed and experimentally demonstrated. The tunable magnetic metamaterials is constructed by split ring unit cells the geometry of which can be changed by MEMS actuators. The size of the unit cells is around 40 μm × 40 μm corresponding to the resonance frequency in THz region. The effective

permeability of the tunable magnetic metamaterial can be tuned from negative (-0.1) to positive (0.5) at the resonant frequency. It demonstrates a unique approach to control the optical properties of metamaterials via changing the geometric dimensions and shapes of the unit cells.

6.2 Recommendations

In this PhD project, different approaches have been studied to develop tunable photonic devices based on MEMS technology. The recommendations for future research are listed as fellow.

The optical double barriers structure is used for the optical tunable devices base on MEMS technology. There are several drawbacks which stop the further increasing the performances of the devices. First, the ray shift caused by the oblique incident light and the Goos-Hänchen effect. This increases the insertion loss of the devices such as the optical switch and polarizer. One of the solutions is shifting the output fiber according to the shift of the Gaussian beams. Second, the thermo-optical effects are used for the demonstration of the optical switches, polarizer and reconfigurable WDM system because of the experimental convenience. For the purpose of fast switching, the photon induced free carrier effect can be used as the tuning mechanism of the double optical barrier structures. For example, the central rib can be fabricated as a micro-cavity which can localize the light and increase the intensity of the light within the rib region. In this way, the tunneling light can be tuned by the guiding light by the rib. This method not only can increase the tuning speed of the optical switches but also can achieve the all optical

switching which is using one beam of light to control another. Furthermore, this method can circumvent the dilemma faced by most the all optical switching method using high Q micro-cavities. The pumping light has to be much stronger than the signal light to induce the nonlinear effects when passing the same optical cavities as the signal light does. The third problem is to further reduce the device scale of the double optical barrier structure. Here in the free space coupling, the device scale is limited by the size of the prisms and the fiber. The prisms can be scaled down with better design while the limitation is still lays on the size of the fiber. The optical tunneling junction sets a good example on how to further reduce the device scale by integrating the tunneling structure with the optical waveguide. In this way the device scale is only limited by the diffraction limit of the light. However the design of the optical tunneling junction has to be further studied for particle applications. For example the coupling of the guiding mode to the resonance tunneling condition is the major problems which increase the insertion loss of the optical tunneling junctions.

The study of the slow light metamaterial shows the possibility to slow the light down using metamaterial waveguide. Furthermore, the tunablility of the optical properties of split ring metamaterial due to the substrate refractive index change is increased by 200 times when using the coupled split ring unit cell. However, the realization of such tunable slow light metamaterials remains a problem. The coupled split ring unit cell has three layers of metal thin films one of which is buried within the substrate and the other two metal films are coated on the opposite side of the substrate. The realization of such metal-dielectric structures is difficult but not impossible using the

existing fabrication techniques. However many works have to be done in order to realize such structures.

The magnetic metamaterial using split ring unit cells are tuned using the MEMS actuators. This tuning method can change the geometry of the metamaterial unit cells thus change the optical properties of the metamaterials fundamentally. This technology opens a new way for the tuning of the metamaterials which will surely lead to a lot of new designs for tunable metamaterials. For example, the design can be emphasized on the geometry of the unit cells which can leads to dramatic change of the metamaterial optical properties or different applications. It can also work on the MEMS side to fertilize the research on the tunable metamaterials such as introducing the rotation, banding or stretching the unit cells of the metamaterial to change the related spatial position of each unit cells. Finally, the theoretical study can be done using the MEMS tunable metamaterial to mimic the transition of the nature materials in the atomic or molecular level. For example, the thermo expansion effect of crystals, the rotation of the molecular and the chemical reaction process.

AUTHOR'S PUBLICATIONS

Journal papers

[1] W. M. Zhu, X. M. Zhang, A. Q. Liu, H. Cai, J. Tamil, and T. Bourouina, "A micromachined optical double well for thermo-optic switching via resonant tunneling effect," *Applied Physics Letters*, Vol. 92, No. 25, 251101, 2008.

[2] W. M. Zhu, X. M. Zhang, T. Zhong, A. Q. Liu and M. Yu, "Micromachined optical well structure for thermo-optic switching," *Applied Physics Letters*, Vol. 91, No. 26, 261106, 2007 □Cover Story□.

[3] W. M. Zhu, X. M. Zhang, A. Q. Liu, T. Bourouina and J. H. Teng, "A slow light metamaterial waveguide," Optics Express (Submitted).

[4] W. M. Zhu, X. M. Zhang, A. Q. Liu, D. P. Tsai, J. H. Teng, T. Mei, T. Bourouina, G. Q. Lo and D. L. Kwong, "Micromachined tunable magnetic metamaterial," *Physical Review Letters*, (Submitted).

Conference papers

[5] W.M. Zhu, W. Zhang, H. Cai, J. Tamil, B. Liu, T. Bourouina and A.Q. Liu, "A MEMS Digital Mirror for Tunable Laser Wavelength Selection," *The 15th International Conference on Solid-State Sensors, Actuators and Microsystems* (*Transducer 2009)*, 2009 (Oral).

[6] W. M. Zhu, H. Cai, T. Mei, T. Bourouina, J. F. Tao, G. Q. Lo, D. L. Kwong and A. Q. Liu, "A mems tunable metamaterial filter", *23th IEEE International Conference on Micro Electro Mechanical Systems (MEMS 2010)*, Hong Kong, 2010 (Oral).

REFERENCES

[1] J. Hecht, “City of Light: The Story of Fiber Optics”, Oxford university press, 1999.

[2] C. Decusatis, “Fiber optic data communication: Technological trends and advances”, Academic press, 2002.

[3] G. P. Agrawal, “Nonlinear fiber optics”, Academic press, 2007.

[4] V. Ronchi, “Optics: The science of vision”, New York university press, 1957.

[5] J. N. Downing, “Fiber-Optic communications”, Thomson Delmar Learning press, 2005.

[6] B. Chomycz, “Planning fiber optic networks”, McGraw-Hill companies, Inc press, 2009.

[7] G. Lifante, “Integrated photonics: Fundamentals”, John Wiley & Sons Ltd press, 2003.

[8] F. J. Duarte, “Tunable laser applications”, CRC press, 2009.

[9] R. W. Boyd, “Nonlinear optics”, Academic Press, 2008.

[10] B. E. A. Saleh, M. C. Teich, “Fundamentals of photonics”, John Wiley & Sons, Inc, 1991.

[11] D. S. Wiersma and S. Cavalierit, “Light emission: A temperature-tunable random laser”, Nature, **414**, pp. 708, 2001.

[12] J. Y. Allain, M. Monerie, H. Poignant, “Tunable green upconversion erbium fibre laser”, Electron. Lett., **28**, pp. 111, 1992.

[13] M. Ozaki, M. Kasano, T. Kitasho, D. Ganzke, W. Haase and K. Yoshino, "Electro-tunable liquid-crystal laser", Adv. Materials, **15**, pp. 974, 2003.

[14] K. J. Kim, J. W. Kim, M. C. Oh, Y. O. Noh and H. J. Lee, "Flexible polymer waveguide tunable lasers", Opt. Express, **18**, pp. 8392, 2010.

[15] L. Y. Lin, E. L. Goldstein and R. W. Tkach, IEEE. J. Selected Topics in Quantum Electronics, **5**, pp. 4, 1999.

[16] D. K. Hunter, M. C. Chia and I. Andonovic, "Buffering in optical packet switches", J. Lightwave Technology, **16**, pp. 2081, 1998.

[17] M. C. Chia, D. K. Hunter, I. Andonovic, P. Ball, I. Wright, S. P. Ferguson, K. M. Guild and M. J. O'Mahony, "Packet loss and delay performance of feedback and feed-forward arrayed-waveguide gratings-based optical packet switches with WDM inputs-outputs", J. Lightwave Technology, **19**, pp. 1241, 2001.

[18] R. Kasahara, M. Yanagisawa, T. Goh, A. Sugita, A. Himeno and M. Yasu, "New structure of silica-based planar lightwave circuits for low-power thermooptic switch and its application to 8 × 8 optical matrix switch" J. Lightwave Technology, **20**, pp. 993, 2002.

[19] W. H. Nelson, A. N. M. M. Choudhury, M. Abdalla, R. Bryant, E. Meland and W. Niland, "Wavelength- and polarization-independent large angle InP/InGaAsP digital optical switches with extinction ratios exceeding 20 dB", IEEE, Photon. Tech. Lett., **6**, pp. 1332, 1994.

[20] O. Ishida, H. Takahashi and Y. Inoue, "Digitally tunable optical filters using arrayed-waveguide grating (AWG) multiplexers and optical switches", J. Lightwave Technology, **15**, pp. 321, 1997.

[21] S. Sudo, K. Mizutani, J. Merlier, T. Okamoto, K. Tsuruoka, K. Sato and K. Kudo, “External cavity wavelength tunable laser with on-chip VOA using etched mirror based integration technology”, Electro. Lett., **42**, pp. 347, 2006.

[22] X. M. Zhang, Q. W. Zhao, A. Q. Liu, J. Zhang, J. H. Lau and C. H. Kam, "Asymmetric tuning schemes of MEMS dual-shutter VOA," Journal of Lightwave Technology, **26**, pp. 569, 2008

[23] A. Q. Liu, A. B. Yu, M. F. Karim and M. Tang (invited review paper), "RF MEMS switches and integrated switching circuit," J. Semicon. Techn. and Sci., Special issue on NANO/Microsystems Technology, **7**, No.3, 2007.

[24] Q. X. Zhang, A. B. Yu, L. H. Guo, R. Kumar, K. W. Teoh, A. Q. Liu, G. Q. Lo, and D. –L. Kwong, "RF MEMS switch integrated on printed circuit board with metallic membrane first sequence and transferring," IEEE Electron Device Lett., **27**, pp. 552, 2006.

[25] X. M. Zhang, A. Q. Liu, C. Lu, D. Y. Tang, "MEMS variable optical attenuator using low driving voltage for DWDM systems ," IEE Electron. Lett., **38**, pp. 382, 2002.

[26] G. D. Valle, M. Ornigotti and E. Cianci, “Visualization of coherent destruction of tunneling in an optical double well system”, Phys. Rev. Lett., **98** (26), paper no. 263601, 2007.

[27] John J. Carey, Justyna Zawadzka and Dino A, “Noncausal time response in frustrated total internal reflection”, Phys. Rev. Lett., **84** (7), 1431, 2000.

[28] R.Y. Chiao, P.G. Kwiat and A.M. Steinberg, “Analogies between electron and photon tunneling”, Physica B, **175**, 257, 1991.

[29] D. Bohm, Quantum Theory, Prentice-Hall, Englewood Cliffs, N.J., 1951.

[30] L.L. Chang, L. Esaki and R. Tsu, “Resonant tunneling in semiconductor double barriers”, Appl. Phys. Lett., **24** (12), 593, 1974.

[31] H. Cai, B. Liu, X. M. Zhang, A. Q. Liu, T. Bourouina and Q. X. Zhang, " A micromachined tunable coupled-cavity laser for wide tuning range and high spectral purity ," Opt. Express, **16**, pp. 16670, 2008.

[32] H. Cai, A. Q. Liu, X. M. Zhang , J. Tamil, D. Y. Tang , J. Wu and Q. X. Zhang, "Tunable dual-wavelength laser constructed by silicon micromachining," Appl. Phys. Lett., **92**, 051113, 2008.

[33] H. Cai, A. Q. Liu, X. M. Zhang , J. Tamil, Q. X. Zhang, D. Y. Tang, C. Lu, "A Miniature Tunable Coupled-Cavity Laser Constructed by Micromachining Technology," Appl. Phys. Lett., **92**, 031105, 2008.

[34] A. Q. Liu, X. M. Zhang, "A review of MEMS external-cavity tunable lasers," J. Micromechanics and Microengineering, **17**, pp. R1, 2007.

[35] N. C. Lindquist, A. Lesuffleur, S. H. Oh, “Periodic modulation of extraordinary optical transmission through subwavelength hole arrays using surrounding Bragg mirrors”, Phys. Rev. B, **76**, 165415, 2007.

[36] O. Glushko, R. Meisels and F. Kuchar, “Simulations of wave propagation and disorder in 3D non-close-packed colloidal photonic crystals with low refractive index contrast”, Opt. Express, **18**, 7101, 2010.

[37] T. Ding, K. Song, K. Clays and C. H. Tung, “Fabrication of 3D photonic crystals of ellipsoids: Convective self-assembly in magnetic field”, Adv. Materials, **21**, 1936, 2009.

[38] M. Imada, S. Noda, A. Chutinan, T. Tokuda, M. Murata and G. Sasaki, “Coherent two-dimensional lasing action in surface-emitting laser with triangular-lattice photonic crystal structure”, Appl. Phys. Lett., **75**, 316, 1999.

[39] Selin H. G. Teo, A. Q. Liu, M. B. Yu, and J. Singh, " Synthesized processing techniques for monolithic iIntegration of nanometers-scale hole type photonic bandgap crystal with micrometers-scale microelectromechanical structures ," J. Vac. Science & Technology B, **24**, pp. 1689, 2006.

[40] Selin H. G. Teo, A. Q. Liu, J. B. Zhang, and M. H. Hong, "Induced free carriers modulation of photonic crystal optical intersection via localized optical absorption effect," Appl. Phys. Lett., **89**, 091910, 2006.

[41] E. H. Khoo, T. H. Cheng, A. Q. Liu and J. Li and D. Pinjala, "Transmitting light efficiently on photonic crystal surface waveguide bend", Appl. Phys. Lett., **91**, 171109, 2007.

[42] E.H. Khoo, A.Q. Liu, X.M. Zhang, E.P. Li, J. Li, D. Pinjala and B.S. Luk'yanchuk, "Exact step-coupling theory for mode-coupling behavior in geometrical variation photonic crystal waveguides," Phys. Rev. B, **80**, 035101, 2009.

[43] Y. F. Yu, V. Kanna, T. Bourouina, S. H. Ng, P. H. Yap, and A. Q. Liu, "An on-chip glass sphere resonator for label-free detection", 23th IEEE International Conference on Micro Electro Mechanical Systems (MEMS 2010), Hongkong.

[44] Y. F. Yu, T. Bourouina, and A. Q. Liu, “On-chip droplet enhanced fluorescence emission for low concentration protein measurement,” The 15th International Conference on Solid-State Sensors, Actuators and Microsystems (Transducers ’09), June 21 - 25, 2009, Denver, CO, USA, pp. 1250-1252, paper T3P.093.

[45] B. Mcnamara, K. Wiesenfeld and R. Roy, “Observation of stochastic resonance in a ring laser”, Phys. Rev. Lett., **60**, 2626, 1998.

[46] M. Tang, A. Q. Liu, and J.Oberhammer, "A silicon-on-Glass Single-Pole Double-Throw (SPDT) Switching Circuit Integrated With Silicon-Core Metal-Coated Transmission Line," J. Micromechanics and Microengineering, **18**, No. 095024, 2008.

[47] J. Oberhammer, M. Tang, A. Q. Liu and G. Stemme, "Mechanically tri-stable, true single-pole-double-throw (SPDT) switches," J. Micromechanics and Microengineering, **16**, pp. 1, 2006.

[48] J. Li, A. Q. Liu, W. D. Zhong, Q. X. Zhang, C. Lu, "MEMS switch based serial reconfigurable OADM," Optics Communications, **230**, pp. 81, 2004.

[49] A. Q. Liu , X. M. Zhang, V. M. Murukeshan, Q. X. Zhang, Q. B. Zou, and S. Uppili, "An optical switch using drawbridge micromirror for large array crossconnects," Sensors & Actuators, Physics A, **97**, pp. 227, 2002.

[50] J- H. Huang, K. M. Liew, C. H. Wong, S. Rajendran, M. J. Tan and A. Q. LIU, "Mechanical design and optimization of capacitive micromachined switch," Sensors and Actuators, Physics A, **93**, pp. 273, 2001.

[51] S. Hrbar, D. Bonefacic and D. Muha, "ENZ-based shortened horn antenna - An experimental study", 2008 IEEE International Symposium on Antennas and Propagation and USNC/URSI National Radio Science Meeting, APSURSI, art. no. 4619853, 2008..

[52] M. G. Silveirinha, A. Alu and N. Engheta, "Parallel-plate metamaterials for cloaking structures", Phys. Rev. E, **75**, 036603, 2007.

[53] A. Alu and N. Engheta, "Achieving transparency with plasmonic and metamaterial coatings", Phys. Rev. E, **72**, 016623, 2005.

[54] E. O. Liznev, A. V. Dorofeenko, L. Huizhe, A. P. Vinogradov and S. Zouhdi, "Epsilon-near-zero material as a unique solution to three different approaches to cloaking", Appl. Phys. A, pp. 1-5, in press, 2010.

[55] D. A. Powell, A. Alu, B. Edwards, A. Vakil, Y. S. Kivshar and N. Engheta, "Nonlinear control of tunneling through an epsilon-near-zero channel", Phys. Rev. B, 79, 245135, 2009.

[56] R. Drori, M. Einat, D. Shur, E. Jerby, G. Rosenman, T. Advani, R. J. Temkin and C. Pralong, "Demonstration of microwave generation by a ferroelectric-cathode tube", Appl. Phys. Lett., **74**, pp. 335, 1999.

[57] L. W. Li, Y. N. Li, T. S. Yeo, J. R. Mosig and O. J. F. Martin, "A broadband and high-gain metamaterial microstrip antenna", Appl. Phys. Lett., **96**, 164101, 2010.

[58] P. Jin and R. W. Ziolkowski, “Broadband, efficient, electrically small metamaterial-inspired antennas facilitated by active near-field resonant parasitic elements”, IEEE Transactions on Antennas and Propagation **58** (2), pp. 318-327, 2010.

[59] J. Zhu and G. V. Eleftheriades, “Dual-band metamaterial-inspired small monopole antenna for WiFi applications”, Electro. Lett., **45**, pp. 1104, 2009.

[60] N. Lopez, C. J. Lee, A. Gummalla and M. Achour, “Compact metamaterial antenna array for long term evolution (LTE) handset application”, 2009 IEEE International Workshop on Antenna Technology, art. no. 4906933, 2009.

[61] M. Quinten, A. Leitner, J. R. Krenn, and F. R. Aussenegg, “Electromagnetic energy transport via linear chains of silver nanoparticles”, Opt. Lett., **23**, pp. 1331, 1998.

[62] M. L. Brongersma, J. W. Hartman and A. Atwater, “Electromagnetic energy transfer and switching in nanoparticle chain arrays below the diffraction limit”, Phys. Rev. B, **62**, 16356, 2000.

[63] T. Zhong, X. M. Zhang, A. Q. Liu, J. Li, C. Lu, And D. Y. Tang, "Thermal-optic switch by total-internal reflection of micromachined silicon prism," IEEE J. Selected Topics in Quantum Electronics, **12**, pp. 348, 2007.

[64] J. Li, A. Q. Liu, X. M. Zhang and T. Zhong, "Light switching via thermo-optic effect of micromachined silicon prism," Appl. Phys. Lett. , **88**, 243501, 2006.

[65] G. T. Reed, “Silicon photonics: An introduction”, John Wiley & Sons, Ltd, 2004.

[66] W. M. Zhu, X. M. Zhang, T. Zhong and A. Q. Liu, "MEMS Optical Tunneling Structure for Thermo-optic Switching," 21th IEEE International Conference on

Micro Electro Mechanical Systems (MEMS 2008), Tucson, Arizona, USA, pp. 782, 2008.

[67] A. Q. Liu, X. M. Zhang, H. Cai, A. B. Yu and C. Lu, "Retro-axial VOA using parabolic mirror pair", IEEE Photonics Technology Letters, **19**, no. 9, pp. 692-694, 2007.

[68] D. R. Smith, J. B. Pendry, M. C. K. Wiltshire, "Metamaterials and Negative Refractive Index", Science, **305**, pp. 788, 2004.

[69] A. Al and N. Engheta, "Polarizabilities and effective parameters for collections of spherical nanoparticles formed by pairs of concentric double-negative, single-negative, andor double-positive metamaterial layers", J. Appl. Phys., **97**, 094310, 2005.

[70] R. A. Shelby, D. R. Smith, S. C. Nematnasser and S. Schultz, "Microwave transmission through a two-dimensional, isotropic, left-handed metamaterial", Appl. Phys. Lett., **78**, pp. 489, 2001.

[71] R. W. Ziolkowski, "Pulsed and CW Gaussian beam interactions with double negative metamaterial slabs" Opt. Express, **11**, pp. 662, 2003.

[72] J. Huang, L. Ran, H. Chen, X. M. Zhang, K. Chen, T. M. Grzegorczyk and J. A. Kong, "Experimental confirmation of negative refractive index of a metamaterial composed of Ω-like metallic patterns", Appl. Phys. Lett., **84**, PP. 1537, 2004.

[73] H. O. Moser, B. D. F. Casse, O. Wilhelmi and B. T. Saw, "Terahertz response of a microfabricated rod-split-ring-resonator electromagnetic metamaterial", Phys. Rev. Lett., **94**, 063901, 2005.

[74] R. W. Ziolkowski, "Propagation in and scattering from a matched metamaterial having a zero index of refraction", Phys. Rev. E, *70*, 046608, 2004.

[75] A. K. Iyer, P. C. Kremer and G. V. Eleftheriades, "Experimental and theoretical verification of focusing in a large, periodically loaded transmission line negative refractive index metamaterial", Opt. Express, **11**, pp. 696, 2003.

[76] A. Alu and N. Engheta, "Cloaking and transparency for collections of particles with metamaterial and plasmonic covers", Opt. Express, **15**, pp. 7578, 2007.

[77] M. C. K. Wiltshire, J. V. Hajnal, J. B. Pendry, D. J. Edwards and C. J. Stevens, "Metamaterial endoscope for magnetic field transfer: Near field imaging with magnetic wires", Opt. Express, **11**, pp. 709, 2003.

[78] M. Shamonin, E. Shamonina, V. Kalinin and L. Solymar, "Properties of a metamaterial element: Analytical solutions and numerical simulations for a singly split double ring", J. Appl. Phys., **95**, pp. 3778, 2004.

[79] K. Guven, M. D. Caliskan and E. Ozbay, "Experimental observation of left-handed transmission in a bilayer metamaterial under normal-to-plane propagation", Opt. Express, **14**, pp. 8685, 2006.

[80] J. D. Baena, L. Jelinek, R. Marques and F. Medina, "Near-perfect tunneling and amplification of evanescent electromagnetic waves in a waveguide filled by a metamaterial: Theory and experiments", Phys. Rev. B, **72**, 075116, 2005.

[81] R. W. Ziokowski and A. D. Kipple, "Reciprocity between the effects of resonant scattering and enhanced radiated power by electrically small antennas in the presence of nested metamaterial shells", Phys. Rev. E, **72**, 036602, 2005.

[82] C. Rockstuhl, F. Lederer, C. Etrich, T. Pertsch and T. Scharf, "Design of an artificial three-dimensional composite metamaterial with magnetic resonances in the visible range of the electromagnetic spectrum", Phys. Rev. Lett., **99**, 017401, 2007.

[83] Y. Yuan, C. Bingham, T. Tyler, S. Palit, T. H. Hand, W. J. Padilla, D. R. Smith and S. A. Cummer et.al., "Experimental verification of epsilon-near-zero metamaterial coupling and energy squeezing using a microwave waveguide", Phys. Rev. Lett., **100**, 033903, 2008.

[84] J. B. Pendry, A. J. Holden, D. J. Robbins and W. J. Stewart, "Magnetism from conductors and enhanced nonlinear phenomena", IEEE Trans. Microw. Theory Tech. **47**, 2075 (1999).

[85] J. D. Baena, L. Jelinek, R. Marquas and J. Zehentner, "Electrically small isotropic three-dimensional magnetic resonators for metamaterial design", Appl. Phys. Lett., 88, 134108, 2006.

[86] A. Bitzer, H. Merbold, A. Thoman, T. Feurer, H. Helm and M. Walther, "Terahertz near-field imaging of electric and magnetic resonances of a planar metamaterial", Opt. Express, 17, ppl 3826, 2009.

[87] R. Liu, Q. Cheng, T. Hand, J.J. Mock, J. T. Cui, S. A. Cummer and D. R. Smith, "Experimental demonstration of electromagnetic tunneling through an epsilon-near-zero metamaterial at microwave frequencies", Phys. Rev. Lett., **100**, 023903, 2008.

[88] D. Korobkin, Y. A. Urzhumov, B. N. Iii, C. Zorman, Z. Zhang, I. D. Mayergoyz and G. Shvets, "Mid-infrared metamaterial based on perforated SiC membrane: Engineering optical response using surface phonon polaritons", Appl. Phys. A, **88**, pp. 605, 2007.

[89] R. W. Ziolkowski, "Propagation in and scattering from a matched metamaterial having a zero index of refraction", Phys. Rev. E, **70**, 046608, 2004.

[90] F. Zhang, G. Houzet, E. Lheurette, D. Lippens, M. Chaubet and X. Zhao, "Negative-zero-positive metamaterial with omega-type metal inclusions", J. Appl. Phys., **103**, 084321, 2008.

[91] A. Alu, A. Salandrino and N. Engheta, "Parallel, series, and intermediate interconnections of optical nanocircuit elements. 2. Nanocircuit and physical interpretation", J. Opt. Soc. Am. B, **24**, pp. 3014, 2007.

[92] J. J. Li and N. Engheta, "Subwavelength plasmonic cavity resonator on a nanowire with periodic permittivity variation", Phys. Rev. B, **74**, 115125, 2006.

[93] W. H. Weber and G. W. Ford, "Propagation of optical excitations by dipolar interactions in metal nanoparticle chains", Phys. Rev. B, **70**, 125429, 2004.

[94] M. Shamonin, E. Shamonina, V. Kalinin and L. Solymar, "Properties of a metamaterial element: Analytical solutions and numerical simulations for a singly split double ring", J. Appl. Phys. **95**, 3778, 2004.

[95] O. Sydoruk, A. Radkovskaya, O. Zhuromskyy, E. Shamonina, M. Shamonin, C. J. Stevens, G. Faulkner, D. J. Edwards and L. Solymar, "Tailoring the near-field guiding properties of magnetic metamaterials with two resonant elements per unit cell", Phys. Rev. B, **73**, 224406, 2006.

[96] E. Shamonina, V. A. Kalinin, K. H. Ringhofer and L. Solymar, "Magneto-inductive waveguide", Electron. Lett., **38**, pp. 371, 2002.

[97] W. J. Padilla, A. J. Taylor, C. Highstrete, M. Lee and R. D. Averitt, "Dynamical electric and magnetic metamaterial response at terahertz frequencies", Phys. Rev. Lett., **96**, 107401, pp. 1, 2001.

[98] J. F. Wang, B. S. Qu, Z. Xu, J. Q. Zhang, Y. M. Yang, H. Ma and C. Gu, "A candidate three-dimensional GHz left-handed metamaterial composed of coplanar magnetic and electric resonators", Photonics and Nanostructures - Fundamentals and Applications, **6**, pp. 183-187, 2008.

[99] I. Sersic, M. Frimmer, E. Verhagen and A. F. Koenderink, "Electric and Magnetic Dipole Coupling in Near-Infrared Split-Ring Metamaterial Arrays", Phys. Rev. Lett., **103**, 213902, 2009.

[100] L. Jelinek, R. Marqus and M. J. Freire, "Accurate modeling of split ring metamaterial lenses for magnetic resonance imaging applications", J. Appl. Phys., **105**, 024907, 2009.

[101] Y. Minowa, T. Fujii, M. Nagai, T. Ochiai, K. Sakoda, K. Hirao and K. Tanaka, "Evaluation of effective electric permittivity and magnetic permeability in metamaterial slabs by terahertz time-domain spectroscopy", Opt. Express, **16**, pp. 4785, 2008.

[102] C. Navau, D. X. Chen, A. Sanchez and N. D. Valle, "Magnetic properties of a dc metamaterial consisting of parallel square superconducting thin plates", Appl. Phys. Lett., **94**, 242501, 2009.

[103] Z. G. Dong, X. M. Xu, H. Liu, T. Li and S. N. Zhu, "Omnidirectional magnetic-resonance transmission and its elimination in a metallic metamaterial comprising rings and plates", Phys. Rev. E, **78**, 066612, 2008.

[104] L. Kang, Q. Zhao, H. Zhao and J. Zhou, "Magnetic tuning of electrically resonant metamaterial with inclusion of ferrite", Appl. Phys. Lett., **93**, 171909, 2008.

[105] D. L. Sounas, N. V. Kantartzis and T. D. Tsiboukis, "Temporal characteristics of resonant surface polaritons in superlensing planar double-negative slabs: Development of analytical schemes and numerical models", IEEE Trans. Antennas Propag., **51**, 2572, 2003.

[106] S. O. Brien and J. B. Pendry, "Photonic band-gap effects and magnetic activity in dielectric composites", Phys. Condens. Matter, **14**, 6383, 2002.

[107] P. G. Balmaz and O. J. F. Martin, "Electromagnetic resonances in individual and coupled split-ring resonators", J. Appl. Phys. **92**, 2929, 2002.

[108] L. V. Panina, A. N. Grigorenko, D. P. Makhnovskiy, "Optomagnetic composite medium with conducting nanoelements", Phys. Rev. B, **66**, 155411, 2002.

[109] M.V. Kostin and V.V. Shevchenko, "Theory of artificial magnetic sub- stances based on ring currents", J. Commun. Technol. Electron., **38**, pp. 78, 1993.

[110] A. Radkovskaya, M. Shamonin, C. J. Stevens, G. Faulkner, D. J. Edwards, E. Shamonina, and L. Solymar, "Resonant frequencies of a combination of split rings: experimental, analytical and numerical study", Microw. Opt. Tech. Lett., **46**, pp.473, 2005.

[111] A. Radkovskaya, M. Shamonin, C. J. Stevens, G. Faulkner, D. J. Edwards, E. Shamonina, and L. Solymar, "An experimental study of the properties of magnetoinductive waves in the presence of retardation", J. Magn. Magn. Mater., **300**, pp. 29, 2006.

[112] M. C. K. Wiltshire, E. Shamonina, I. R. Young and L. Solymar, "Dispersion characteristics of magneto-inductive waves: comparison between theory and experiment", Edwards, Electron. Lett., **39**, pp. 215, 2003.

[113] S. A. Schelkunoff and H. T. Friis, "Antennas: Theory and Practice", John Wiley and Sons, 1952.

[114] H. Mosallaei and K. Sarabandi, "Antenna miniaturization and bandwidth enhancement using reactive impedance substrate", Antennas Propag. Soc. Int. Symp. **1**, 301, 2004.

[115] M. V. Kostin and V. V. Shevchenko, "Artificial magnetics based on double circular elements, in: Proc. of Bianisotropics'94", Perigueux, France, pp. 49, 1994.

[116] M. C. K. Wiltshire, J. B. Pendry, I. R. Young, D. J. Larkman, D. J. Gilderdale, J. V. Hajnal, "Microstructured Magnetic Materials for RF Flux Guides in Magnetic Resonance Imaging", Science, **291**, pp. 849, 2001.

[117] J. D. Baena, R. Marques, F. Medina and J. Martel, "Artificial magnetic metamaterial design by using spiral resonators", Phys. Rev. B, **69**, 014402, 2002.

[118] T. Hao, C. J. Stevens, and D. J. Edwards, "Simulations and measurements for 1D metamaterial elements", Proc. of the SPIE-COO Conference, Warsaw, Poland, 2005.

[119] I. Bulu, C. Humeyra, K. Aydin and E. Ozbay, "Study of the field emitted by a source placed inside a two-dimensional left-handed metamaterial", Opt. Lett., **31**, pp. 814, 2007.

[120] P. M. T. Ikonen, K. N. Rozanov, A. V. Osipov, P. Alitalo and S. A. Tretyakov, "Magnetodielectric Substrates in Antenna Miniaturization: Potential and Limitations", IEEE. Trans. Antennas and Propagation, **54**, pp. 3391, 2006.

[121] T. J. Yen, W. J. Padilla, N. Fang, D. C. Vier, D. R. Smith, J. B. Pendry, D. N. Basov, X. Zhang, "Terahertz Magnetic Response from Artificial Materials", Science, **303**, pp. 1494, 2004.

[122] S. Linden, C. Enkrich, M. Wegener, J. Zhou, T. Koschny and C. M. Soukoulis, "Magnetic Response of Metamaterials at 100 Terahertz", Science, **306**, pp. 1351, 2004.

[123] S. Zhang, W. Fan, N. C. Panoiu, K. J. Malloy, R. M. Osgood and S. R. J. Brueck, "Experimental Demonstration of Near-Infrared Negative-Index Metamaterials", Phys. Rev. Lett. **95**, 137404, 2005.

[124] V. M. Shalaev, W. Cai, U. K. Chettiar, H.-K. Yuan, A. K. Sarychev, V. P. Drachev, and A. V. Kildishev, "Negative index of refraction in optical metamaterials", Opt. Lett. **30**, 3356, 2005.

[125] G. Dolling, M. Wegener, C. M. Soukoulis, and S. Linden, "Negative-index metamaterial at 780 nm wavelength", Opt. Lett. **32**, pp. 53, 2007.

[126] Y. Svirko, N. Zheludev, and M. Osipov, "Layered chiral metallic microstructures with inductive coupling", Appl. Phys. Lett. **78**, pp. 498, 2001.

[127] V. A. Podolskiy, A. K. Sarychev, and V. M. Shalaev, "Plasmon modes in metal nanowires", J. Nonlinear Opt. Phys. Mater., **11**, pp. 65, 2002.

[128] V. S. Podolskiy, A. K. Sarychey, E. E. Narimanov and V. M. Shalaev, "Resonant light interaction with plasmonic nanowire systems", J. Opt. A, Pure Appl. Opt., **7**, S32, 2005.

[129] C. Enkrich, M. Wegener, S. Linden, S. Burger, L. Zschiedrich, F. Schmidt, J. F. Zhou, T. Koschny and C. M. Soukoulis, "Magnetic metamaterials at telecommunication and Visible frequencies", Phys. Rev. Lett., **95**, 203901, 2005.

[130] J. S. Shumaker-Parry, H. Rochholz, and M. Kreiter, "Fabrication of crescent-shaped optical antennas", Adv. Mater., **17**, 2131, 2005.

[131] J. Zhang, P. A.R. Ade, P. Mauskopf, L. Moncelsi, G. Savini and N. Whitehouse, "Light transmission properties of holey metal films in the metamaterial limit: Effective medium theory and subwavelength imaging", New Journal of Physics, **11**, 123013, 2009.

[132] B. Zhang and G. Barbastathis, "Dielectric metamaterial magnifier creating a virtual color image with far-field subwavelength information", Opt. Express, **18**, pp. 11552, 2010.

[133] B. Zeng, X. Yang, C. Wang, Q. Feng and X. Luo, "Super-resolution imaging at different wavelengths by using a one-dimensional metamaterial structure", J. Optc. A, **12**, 035104, 2010.

[134] A. Schneider, A. Shuvaev, S. Engelbrecht and S. O. Demokritov, "Electrically excited inverse electron spin resonance in a split-ring metamaterial resonator", Phys. Rev. Lett., **103**, 103907, 2009.

[135] N. Papasimakis, Y.H. Fu, V. A. Fedotov, S. L. Prosvirnin, D. P. Tsai and N. I. Zheludev, "Metamaterial with polarization and direction insensitive resonant

transmission response mimicking electromagnetically induced transparency", Appl. Phys. Lett. **94**, 211902, 2009.

[136] P. Tassin, G. D. V. Sande, I. Veretennicoff, P. Kockaert and M. Tlidi, "Pattern formation without diffraction matching in optical parametric oscillators with a metamaterial", Opt. Express, **17**, pp. 9428, 2009.

[137] S. Enoch and N. Bonod, "Absorption of light by Extremely shallow metallic gratings: Metamaterial behavior evgeny popov", Opt. Express, **17**, pp. 6770, 2009.

[138] R. Yang, Y. Xie, X. Yang, R. Wang and B. Chen, "Fundamental modal properties of SRR metamaterials and metamaterial based waveguiding structures", Opt. Express, **17**, pp. 6101, 2009.

[139] C. Yan, Y. Cui, Q. Wang and S. Zhuo, "Superwide-band negative refraction of a symmetrical E-shaped metamaterial with two electromagnetic resonances", Phys. Rev. E, **77**, 056604, 2008.

[140] C. W. Qiu, S. Zouhdi and Y. L. Geng, "Shifted resonances in coated metamaterial cylinders: Enhanced backscattering and near-field effects", Phys. Rev. E, **77**, 046604, 2008.

[141] L. L. Hou, J. Y. Chin, X. M. Yang, X. Q. Lin, R. Liu, F. Y. Xu and T. J. Cui, "Advanced parameter retrievals for metamaterial slabs using an inhomogeneous model", J. Appl. Phys. **103**, 064904, 2008.

[142] F. Y. Meng, Q. Wu and L. W. Li, "Transmission characteristics of wave modes in a rectangular waveguide filled with anisotropic metamaterial", Appl. Phys. A, **94**, pp. 747-753, 2009.

[143] J. S. G. Diaz, A. A. Melcon, S. Gupta and C. Caloz, "Spatiooral Talbot phenomenon using metamaterial composite right/left-handed leaky-wave antennas", J. Appl. Phys., **104**, 104901, 2008.

[144] J. W. Dong and H. Z. Wang, "Slow electromagnetic propagation with low group velocity dispersion in an all-metamaterial-based waveguide", Appl. Phys. Lett., **91**, 111909, 2007.

[145] C. M. Krowne, "Low loss guided wave propagation in a left-handed microstrip structure using dispersive split ring-rod combination metamaterial", IET Microwaves, Antennas and Propagation, **1**, pp. 887, 2007.

[146] M. A. C. Beltran, K. D. Irwin, G. C. Hilton, L. R. Vale and K. W. Lehnert, "Amplification and squeezing of quantum noise with a tunable Josephson metamaterial", Nat. Phys., **4**, pp. 928, 2008.

[147] S. Ahmed and Q. A. Naqvi, "Electromagnetic scattering from a perfect electromagnetic conductor circular cylinder coated with a metamaterial having negative permittivity and/or permeability", Opt. Communications, **281**, pp. 5664, 2008.

[148] H. T. Chen, J. F. Hara, A. K. Azad, A. J. Taylor, R. D. Averitt, D. Shrekenhamer and W. J. Padilla, "Experimental demonstration of frequency-agile terahertz metamaterials", Nat. Photonics, **2**, 295, 2008.

[149] H. T. Chen, J. F. Hara, A. J. Taylor, R. D. Averitt, C. Highstrete, M. Lee and W. J. Padilla, "Complementary planar terahertz metamaterials", Opt. Express, **15**, pp. 1084, 2007.

[150] H. T. Chen, W. J. Padilla, J. O. M. Zide, S. R. Bank, A. C. Gossand, A. J. Taylor and R. D. Averitt, " Active terahertz metamaterial devices", Nature, **444,** pp. 597, 2006.

[151] H. T. Chen, W. J. Padilla , J. O. M. Zide, S. R. Bank, A. C. Gossand, A. J. Taylor and R. D. Averitt, "Ultrafast optical switching of terahertz metamaterials fabricated on ErAs/GaAs nanoisland superlattices, Opt. Lett., 32, 1620, 2007.

[152] W. J. Padilla, "Group theoretical description of artificial electromagnetic metamaterials", Opt. Express, **15**, pp. 1639, 2007.

[153] A. Fang, T. Koschny and C. M. Soukoulis, "Lasing in metamaterial nanostructures", J. Opt. A, **12**, 024013, 2010.

[154] R. Yahiaoui, S. N. Burokur and A. D. Lustrac, "Enhanced directivity of ultra-thin metamaterial-based cavity antenna fed by multisource", Electron. Lett., 45, pp. 814, 2009.

[155] P. Ginzburg and M. Orenstein, "Metal-free quantum-based metamaterial for surface plasmon polariton guiding with amplification", J. Appl. Phys., **104**, 063513, 2008.

[156] D. N. Fittinghoff, P. R. Bolton, B. Chang and K. C. Kulander, "Observation of nonsequential double ionization of helium with optical tunneling", Phys. Rev. Lett., **69**, pp. 2642, 1992.

[157] C. Spielmann, R. Szipocs, A. Stingl and F. Krausz, "Tunneling of optical pulses through photonic band gaps", Phys. Rev. Lett., 73, pp. 2308, 1994.

[158] D. P. Tsai, J. Kovacs, Z. Wang, M. Moskovits, V. M. Shalaev, J. S. Suh and R. Botet, "Photon scanning tunneling microscopy images of optical excitations of fractal metal colloid clusters", Phys. Rev. Lett., **72**, pp. 4149, 1994.

[159] P. Balcou and L. Dutriaux, "Dual optical tunneling times in frustrated total internal reflection", Phys. Rev. Lett. **78**, pp. 851, 1997.

[160] Q. Niu, X. G. Zhao, G. A. Georgakis and M. G. Raizen, "Atomic Landau-Zener tunneling and Wannier-Stark ladders in optical potentials", Phys. Rev. Lett. **76**, pp. 4504, 1996.

[161] L. J. Wang, A. Kuzmich and A. Dogariu, "Gain-assisted superluminal light propagation", Nature, **406**, pp. 277. 2000.

[162] I. F. Mirabel and L. F. Rodriguez, "A superluminal source in the Galaxy", Nature, **371**, pp. 46, 1994.

[163] M. S. Bigelow, N. N. Lepeshkin and R. W. Boyd, "Superluminal and slow light propagation in a room-temperature solid", Science, 301, pp. 200, 2003.

[164] D. Mugnai, A. Ranfagni and R. Ruggeri, "Observation of Superluminal Behaviors in Wave Propagation", Phys. Rev. Lett., **84**, pp. 4830, 2000.

[165] A. M. Steinberg and R. Y. Chiao, "Dispersionless, highly superluminal propagation in a medium with a gain doublet" Phys. Rev. A, **49**, pp. 2071, 1994.

[166] E. Hecht, "Optics", Addison Wesley, 2002.

[167] W. M. Zhu, X. M. Zhang, A. Q. Liu, H. Cai, J. Tamil, And T. Bourouina, "A micromachined optical double well for thermo-optic switching via resonant tunneling effect", Appl. Phys. Lett., **92**, 251101, 2008.

[168] W. M. Zhu, X. M. Zhang, H. Cai, J. Tamil, W. Zhang, B. Liu, T. Bourouina and A. Q. Liu, "Mems laser with tunable wavelength and polarization using optical tunneling effect", 22th IEEE International Conference on Micro Electro Mechanical Systems, Italy, 2009.